Carmen Pérez León

Vibrational Spectroscopy of Photosensitizer Dyes for Organic Solar Cells

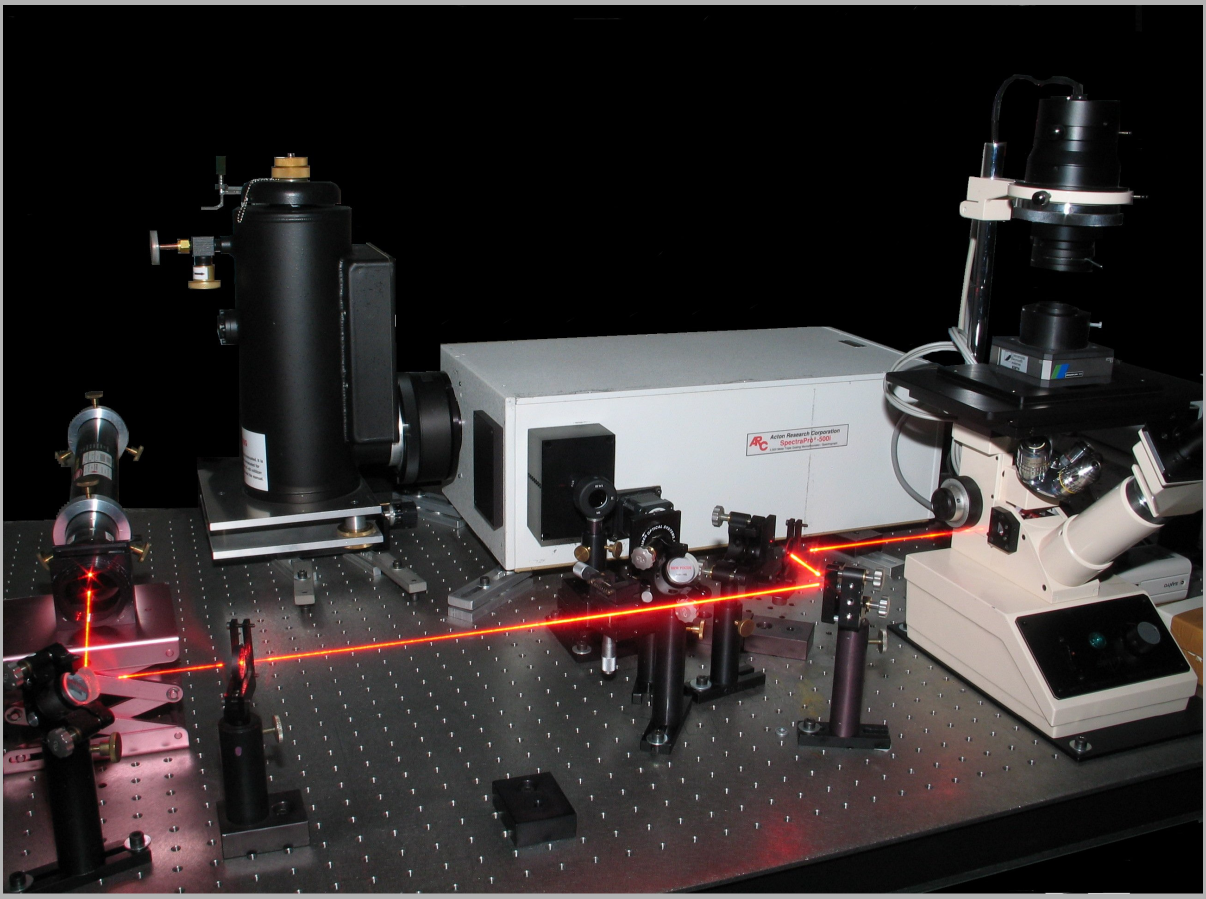

Vibrational Spectroscopy of Photosensitizer Dyes for Organic Solar Cells

Von der Universität Bayreuth
zur Erlangung des Grades eines
Doktors der Naturwissenschaften (Dr. rer. nat.)
genehmigte Abhandlung

vorgelegt von

Carmen Pérez León

geboren am 9. July 1975 in Sevilla, Spanien

1. Gutachter:	Apl. Prof. Dr. L. Kador
2. Gutachter:	Prof. Dr. A. Seilmeier
Tag der Einreichung:	25. Juli 2005
Tag des Kolloquiums:	18. November 2005

Zusammenfassung

Ruthenium(II)-Komplexe mit Polypyridyl-Liganden werden derzeit ausgiebig auf ihre mögliche Anwendung als Photosensibilisatoren untersucht [1–4]. Von besonderem Interesse ist ihre Verwendung in farbstoffsensibilisierten Solarzellen auf der Basis von nanokristallinen Titandioxid-Filmen. Funktionelle Gruppen des Farbstoffes ermöglichen eine effiziente Verankerung auf der Oberfläche des Halbleiters (TiO_2) und verstärken die elektronische Wechselwirkung zwischen dem Donor-Orbital des Farbstoffes und dem Leitungsband des Halbleiters.

In dieser Arbeit wurden Ruthenium-Bipyridyl-Komplexe mit unterschiedlichen Liganden untersucht, um den Einfluss der Wechselwirkungen zwischen Lösungsmittel, Komplex und Substrat besser zu verstehen. Als Farbstoffe wurden der kommerzielle Photosensibilisator $(Bu_4N)_2[Ru(dcbpyH)_2(NCS)_2]$ oder N719 mit Cyano-Liganden sowie ein neuer Farbstoff $[Ru(dcbpyH_2)_2(bpy\text{-}TPA_2)](PF_6)_2$ oder Ru-TPA_2 mit Triphenylamin-Liganden verwendet.

Die Untersuchungen wurden mit den Spektroskopiemethoden UV-VIS, normale Raman-Spektroskopie, Präresonanz- und Resonanz-Raman-Spektroskopie, SERS, Absorptions-FTIR and ATR-FTIR durchgeführt. Zur Aufnahme der Raman-Spektren wurden als Anregungslichtquellen ein HeNe-Laser (λ = 632.8 nm) und ein frequenzverdoppelter Nd:YAG-Laser (λ = 532 nm) verwendet. Die Ergebnisse können wie folgt zusammengefasst werden:

Im Kapitel 3 werden die reinen Farbstoffe spektroskopisch charakterisiert. UV-VIS-Absorptionsexperimente zeigen bei beiden Farbstoffen solvatochrome Verschiebungen der elektronischen Übergänge auf Grund von Wasserstoffbrückenbindungen und Donor-Akzeptor-Wechselwirkungen zwischen den Liganden und den Lösungsmittelmolekülen. Die Übergänge von N719 zeigen eine Blauverschiebung mit zunehmender *Gutmann acceptor number*, was auch schon bei anderen Cyano- und Thiocyano-Komplexen beobachtet worden war. Dagegen weisen die Übergänge von Ru-TPA_2 eine Rotverschiebung mit zunehmender *Gutmann donor number* des Lösungsmittels auf, außer beim Wasser, das eine größere Verschiebung als Ethanol bewirkt. Ein zusätzlicher Beitrag der verschiedenen deprotonierten Zustände der Farbstoffe wurde ebenfalls berücksichtigt.

Das Resonanz-Raman-Spektrum von N719 lässt vermuten, dass der niedrigste MLCT-Übergang einer Injektion eines Elektrons in die Bipyridin-Liganden entspricht. Die stärksten Linien im Raman-Spektrum von Ru-TPA$_2$ sind die Linien des TPA-Liganden, unabhängig davon, ob das Spektrum mit dem roten oder dem grünen Laser aufgenommen wurde. Bei grünem Anregungslicht werden die Bipyridin-Linien durch Präresonanzeffekte leicht verstärkt. Eine detaillierte Zuordnung der Vibrationslinien wurde sowohl für die Raman- als auch für die FTIR-Spektren durchgeführt.

Unterschiedliche TiO$_2$-Substrate wurden verwendet. In den Raman- und FTIR-Spektren werden den Linien die entsprechenden Schwingungen zugeordnet. Die Kristallinität der verschiedenen Proben wird kurz diskutiert.

In Kapitel 4 wird der Einfluss des Lösungsmittels auf die Adsorption der beiden Farbstoffe an kolloide Partikel mit oberflächenverstärkter Raman-Spektroskopie (SERS) untersucht. Wasser, Ethanol und Acetonitril wurden als Lösungsmittel verwendet. Die SERS-Substrate waren kolloide Silber- und Goldlösungen.

Die Analyse der aufgenommenen Spektren ergibt, dass die Farbstoffe an die kolloiden Systeme abhängig von Lösungsmittel in unterschiedlicher Art und Weise adsorbiert sind. Bei sauren pH-Werten und mit Acetonitril als Lösungsmittel (Akzeptor für Wasserstoffbrückenbindungen) deprotonieren die Farbstoffe nicht vollständig und binden über ihre Elektron-Donor-Liganden, während sie in Wasser (sowohl Donor als auch Akzeptor für Wasserstoffbrückenbindungen) auch über ihre Elektron-Akzeptor-Liganden binden. In Ethanol (Donor für Wasserstoffbrückenbindungen) verhält sich N719 ebenso wie in Wasser, aber Ru-TPA$_2$ bindet nur über seine Elektron-Akzeptor-Liganden.

Auch bei basischem pH-Wert hat das Lösungsmittels einen Einfluss darauf, wie die Moleküle an den metallischen Partikeln haften. In Acetonitril (Akzeptor für Wasserstoffbrückenbindungen) wird die Bindung über die Elektron-Donor-Liganden bevorzugt. In Wasser und Ethanol (Donor für Wasserstoffbrückenbindungen) dagegen binden die Farbstoffe auch über ihre Akzeptor-Liganden, die Dicarboxybipyridine.

Die mit SERRS (oberflächen- und resonanzverstärkter Raman-Spektroskopie) erhaltenen Signale des Farbstoffes N719 sind sehr ähnlich zu den mit dem roten Laser aufgenommenen SERS-Spektren, zeigen aber zusätzlich die Charakteristika des Resonanzeffekts. Der Vergleich mit den RRS-Spektren des N719-Pulvers weist darauf hin, dass wahrscheinlich nur die Schwingungen, die mit der Verankerung auf dem kolloiden System verknüpft sind, durch die Adsorption beeinflusst werden. Für Ru-TPA$_2$ sind die Spektren ebenfalls für beide Anregungswellenlängen sehr ähnlich. Eine geringe Verstärkung der zu den Bipyridinen gehörigen Linien durch Präresonanzeffekte konnte beobachtet werden.

Weiterhin stellte sich heraus, dass in wässrigen Goldlösungen der Farbstoffe kein SERS-Signal zu Stande kommt und dass der SERS-Effekt in Ethanol-Goldlösungen sehr schwach ist. Das kann durch die niedrigere Affinität der Komplexe zu Gold im Vergleich zu Silber erklärt werden, die anscheinend zur Folge hat, dass die Wechselwirkung zwischen Farbstoff und Goldnanopartikeln nicht stark genug ist, um die Wasserstoffbrückenbindung zwischen Farbstoff und Lösungsmittelmolekül aufzubrechen.

Starke SERS-Signale wurden für beide Komplexe in Goldlösung aufgenommen, wenn als Lösungsmittel Acetonitril verwendet wurde. Außerdem treten dann Resonanzeffekte auf, vor allem für den Farbstoff Ru-TPA$_2$. Das UV-VIS-Absorptionsmaximum verschiebt sich auf Grund eines Ladungstransfers zwischen dem Komplex und dem metallischen Nanopartikel. Die Ähnlichkeit zwischen den SERS- und den SERRS- Signalen von Ru-TPA$_2$ weist auf die wichtige Rolle des chemischen Verstärkungsmechanismus hin. Ladungstransfer, Wasserstoffbrückenbindungen und Donor-Akzeptor-Wechselwirkungen müssen bei der Interpretation der beobachteten Spektren berücksichtigt werden. Die Änderung des pH-Wertes in den basischen Bereich hat den gleichen Einfluss wie bei der Silberlösung: N719 zeigt kleine Veränderungen in seinem Adsorptionsverhalten, während die Spektren von Ru-TPA$_2$ unbeeinflusst bleiben, was die hohe Affinität der TPA-Liganden zu Gold bestätigt.

Ein weiteres Ergebnis besteht darin, dass die Zugabe von NaCl als Elektrolyt eine Bindung über die Donor-Liganden zu begünstigen scheint.

In Kapitel 5 wird die Adsorption von N719 und Ru-TPA$_2$ auf zwei verschiedenen nanokristallinen TiO$_2$-Substraten charakterisiert. Der erste Teil ist der Untersuchung von farbstoffsensibilisierten Filmen aus Anatas-Paste gewidmet. Im zweiten Teil wurde statt der Paste ein Anatas-Nanopulver verwendet. UV-VIS-, Raman- und FTIR-Spektroskopie wurden benutzt.

Die untersuchten Ruthenium-Polypyridyl-Farbstoffe enthalten Carboxy-Liganden, mit denen sie an TiO$_2$ binden. Diese Carboxy-Gruppen können mit Metallionen auf unterschiedliche Weise wechselwirken: Durch physikalische Adsorption über eine Wasserstoffbrückenbindung oder durch Bildung einer chemischen Bindung. Dabei sind unidentate, bidentate (Chelat) oder verbrückende Bindung möglich. Eine unidentate Bindung besteht darin, dass ein Sauerstoffatom der Carboxyl säure-Gruppe mit dem Metallion eine Esterbindung eingeht. Bei der bidentaten bzw. verbrückenden Bindung wechselwirken beide Sauerstoffatome dieser Gruppe gleich stark mit einem Metallion bzw. mit zwei Metallionen.

Im ersten Teil zeigen die UV-VIS-Absorptionsmessungen des Titandioxid-Films einen geringen Einfluss der Adsorption auf die elektronischen Übergänge, nämlich eine Verschiebung zu niedrigeren Energien. Raman-Experimente bei den zwei Anregungswellenlängen zeigen, dass effiziente photoinduzierte Ladungstransfer-Prozesse zwischen Adsorbat und Substrat stattfinden. Außerdem wurde erstmalig ein Raman-Spektrum eines an TiO$_2$ adsorbierten Ru-bpy-Farbstoffes (hier der Farbstoff N719) aufgenommen, wobei nur die SERS-Vertärkung ausgenützt wurde, aber nicht die Resonanzbedingung erfüllt war. Präresonante Effekte im Fall von Ru-TPA$_2$ erlauben es, ein Raman-Spektrum mit sehr gutem Signal-Rausch Verhältnis zu messen. Der Fluoreszenz-Hintergrund kann auf Rückstände von nicht chemisorbierten Molekülen zurückgeführt werden. Die Raman-Messungen legen nahe, dass die Koordination der beiden Komplexe auf dem TiO$_2$-Film durch bidentate oder verbrückende Bindung erfolgt. Dieses Ergebnis wurde durch die ATR-FTIR-Spektren bestätigt, die direkte Aussagen über den Deprotonierungsgrad der Carboxy-Liganden und über ihre Wechselwirkungen mit der TiO_2-Oberfläche ermöglichen.

Es wurde außerdem gezeigt, dass die Thiocyanat-Gruppe des Komplexes N719 von der Adsorption eindeutig beeinflusst wird, während die Auswirkung auf den Donor-Liganden des Ru-TPA_2, die bpy-TPA_2-Gruppe, nur sehr klein zu sein scheint.

Weder Raman- noch ATR-FTIR-Spektroskopie zeigen Unterschiede in der Bindungs-Konfiguration des Farbstoffes N719 auf dem TiO_2-Film, wenn die Proben mit verschiedenen Lösungmittelm präpariert werden. Nur in den SERRS-Spektren konnten sehr kleine Variationen beobachtet werden.

Im zweiten Teil von Kapitel 5 werden FTIR-Messungen an KBr-Pellets vorgestellt, die aus den an Anatas-Nanopulver absorbierten Farbstoffen gepresst wurden. Sie machen deutlich, dass der Farbstoff N719 mit TiO_2 verbrückende oder bidentate Bindungen eingeht, ähnlich wie bei der Anatas-Paste. Dagegen scheinen die Ru-TPA_2-Komplexe über eine unidentate oder Esterbindung oder durch direkte Physisorption über Wasserstoffbrücken zu binden, was hier im Gegensatz zum Fall der Anatas-Paste steht. Das weist auf eine starke Abhängigkeit der Bindungskonfiguration vor der Morphologie des Halbleiters hin.

Contents

List of Tables

Introduction

Here comes the sun...
George Harrison

The demand of energy has dramatically increased since the start of the industrial revolution, in which the transformation of heat into motion began to be applied. This increase is the result not only of industrial development but also of population growth. Part of this energy is wasted by modern habits or life style, but since this is not the subject of the present thesis, it will not be discussed further. Nowadays, the majority of the energy sources are non-renewable, such as fossil fuels — coal, oil and natural gas, which provide over 80% of our energy — plus uranium. These sources are contaminating, dangerous, or produce a strong impact on the environment — especially the climate; hence, the world is in search of alternative renewable sources of energy. This includes solar, wind and wave energy, biomass (wood or crops such as sugar), geothermal energy, and hydro power [5]. These alternative sources are fast developing in some countries, e.g. eolic energy constitutes the 6% of the primary energy in the European Union, but less than 1% world-wide. Big expectations are related to fusion research (ITER), which is considered the energy source of the future.

Amongst the renewable energy sources, solar energy is one of the most promising. An immense amount of energy from the sun strikes the surface of the earth every day. This energy may be captured and used in the form of heat for some applications, or it may be converted directly into electricity using photovoltaic cells.

In the early 1950s, researchers at Bell Laboratories produced the first silicon-based solar cell that generated enough electricity to operate common electric devices. In 1958, the first Earth-orbiting satellite, Vanguard I, was powered with solar energy. Slowly, solar technology has become the standard method for generating energy in the space. But it was not until the 1970s that it has started to be commonly used on the Earth, in everyday-life devices. Since then, the prices of these cells have decreased but still this technology remains expensive compared with other energy sources.

Inorganic solar cells consist of a semiconductor (generally silicon) which has been doped with impurity atoms so that it contains positively charged (p-type) and negatively charged (n-type) regions. The semiconductor absorbs photons whose energies are above its energy gap. These photons excite electrons from the valence band to the conduction band, producing electron-hole pairs near the interface between the two regions (p-n junction) which are separated by the potential difference across the interface. Electrons will migrate toward the positive side of the junction and holes toward the negative side leading to a flow of electric current. This type of solar cells can reach efficiencies of about 25% on the Earth and roughly 30% in space. But for optimum performance of these cells, large high-purity single crystals are needed and the crystal-growth processes required are highly demanding, which is finally reflected in the price. Therefore, cheaper solar cells have been searched for.

In 1991, O'Regan and Grätzel published an article entitled: "A low-cost, high-efficiency solar cell based on dye-sensitized colloidal TiO_2 films" [1] which opened up a new perspective in the world of solar energy. The authors presented the first dye-sensitized nanocrystalline solar cell with an announced conversion yield of 7.1%, which is presently claimed to be over 10% [6]. In contrast to conventional silicon cells, in dye-sensitized photovoltaic cells, light absorption and charge separation occur in separate molecular layers. This simplifies the cell design, thus leading to lower costs.

The dye-sensitized solar cells consists of a Ru-complex adsorbed on nanocrystalline layers of TiO_2. This dye is often a member of the ruthenium-polypyridyl family. The molecules contain anchoring groups such as carboxylic acid, dihydroxy, and phosphonic acid, which serve to immobilize the dye on the nanocrystalline TiO_2 surface [7]. The dye absorbs the incoming light, and after photoexcitation, transfers an electron to the conduction band of the semiconductor (TiO_2). The injected electrons percolate in the nanocrystalline TiO_2 to the anode. The oxidized form of the dye is rapidly reduced by redox mediators. A good understanding of the phenomenon is necessary for further optimization of the performance of the cells and for enhancing their quantum yield.

In the present thesis, ruthenium bipyridiyl complexes with ligands of different nature have been investigated in order to obtain a better understanding of the influence of the interactions between solvent, complex, and substrate. The dyes were the well-known $(Bu_4N)_2[Ru(dcbpyH)_2(NCS)_2]$ photosensitizer with cyano ligands and a new dye, $[Ru(dcbpyH_2)_2(bpy\text{-}TPA_2)](PF_6)_2$, with triphenylamine (TPA) moieties.

For this purpose, UV-VIS, Raman, resonance Raman, SERS, FTIR, and ATR-FTIR spectroscopies have been used. UV-VIS spectroscopy provides information about the electronic transitions of the dye molecules, while the vibrational spectroscopies are able to offer structural information of the adsorption processes as well as the relevant changes induced by the chemisorption on the surface.

The fundamentals and the experimental setups of these techniques are described in the theoretical and experimental introductions, chapter 1 and 2, respectively.

The aim of chapter 3 is to characterize the samples using the different spectroscopic techniques. In addition, different TiO_2 substrates are described.

The adsorption of the complexes on silver and gold nanoparticles is investigated with surface-enhanced Raman spectroscopy (SERS) in chapter 4. SERS data provide highly sensitive information about the orientation of the adsorbate with respect to the metal surface and about the nature of the interaction of the molecule with the colloidal system.

In chapter 5, the adsorption of the dye on two different TiO_2 substrates, anatase paste films and anatase nanopowder, is studied which clarifies the role of the carboxylate groups in the anchoring process of the dyes on the semiconductor surface.

Finally, the results obtained in this thesis and an outlook to suggested future research activities are summarized in chapter 6.

Chapter 1

Theoretical Background

1.1 Interaction of Molecules with Electromagnetic Radiation

Using the Born-Oppenheimer approximation, the energy of a molecule in one of its eigenstates can be written as the sum of four terms which correspond to different motions of the molecule:

$$E = E_{transl} + E_{elec} + E_{vib} + E_{rot}, \tag{1.1}$$

where E_{transl} is the energy of the translation of the molecule, E_{elec} the electronic energy, E_{vib} the contribution of the vibrations of the atoms or atomic groups, and E_{rot} that of the rotation of the complete molecule. Since the translational motion is not of interest, the E_{transl} term will be neglected in the following. Also E_{rot} will be disregarded, since rotational transitions are not resolved in condensed matter.

Molecular spectroscopy is the study of the interaction of light with matter. The photons can interact with the molecules in three different ways: by absorption, emission and scattering (see Fig. 1.1).

> *Absorption* takes place if the photon energy corresponds to the difference between two energy eigenlevels of the molecule. The molecules are excited to a higher energy level when they absorb light. The type of excitation depends on the wavelength of this light (λ). For example, with UV and visible light (200-700 nm) electrons are promoted to higher orbitals, with infrared light (1000 nm-2.5 μm) vibrations are excited, and with far-IR and microwaves (25 μm-2.5 cm) rotations are excited. An absorption spectrum represents the absorption as a function of wavelength.
>
> *Emission* occurs when the excited molecules decay to lower energy levels emitting a photon whose energy corresponds to the difference between two energy

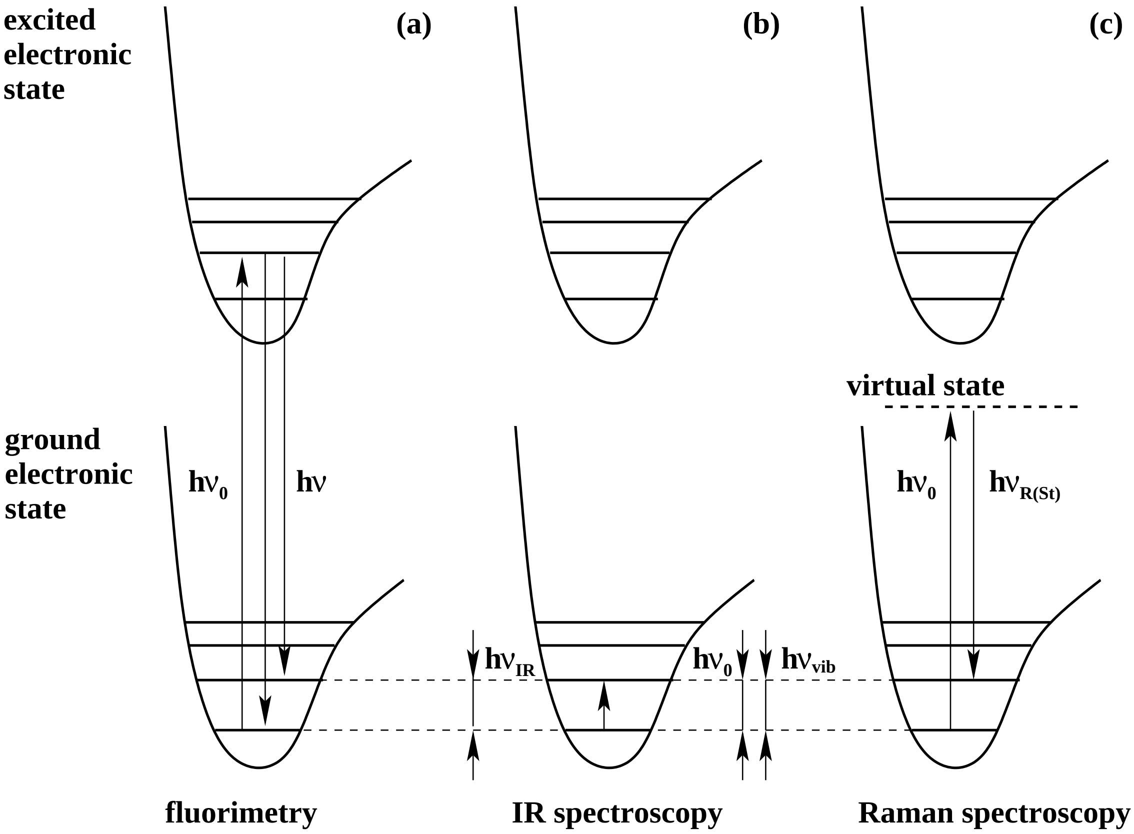

FIG. 1.1. Comparison of the different interactions of molecules with light: **(a)** UV-VIS absorption/emission, **(b)** IR absorption, and **(c)** Raman scattering; and the different spectroscopic techniques to study them.

levels of the molecule. If the transition is between states with the same spin, the emission is called fluorescence, if they have different spin, phosphorescence. Typical lifetimes of excited electronic states are several nanoseconds.

Also *scattering* of the irradiated light can occur but with less probability. The energy of the scattered photon does not correspond to the difference between two energy levels of the molecule. If the interaction is elastic, it is called Rayleigh scattering, if inelastic, Raman scattering. This process takes place instantaneously ($< 10^{-12}$ s).

In this chapter a theoretical description of the interaction of UV, visible, and infrared light with molecules is given. A partial quantum mechanical formulation is used: The radiation is treated classically and is regarded as the source of a perturbation of the molecular system which is treated quantum-mechanically. Transitions between energy levels of the molecular system can occur with absorption or emission of radiation, if the transition dipole moment between the initial and the final molecular state is non-zero. For light scattering, the polarizability of the molecule is the important quantity. Moreover a qualitative discussion of the selection rules and a general overview of the band assignment of the different spectra are also included. The fundamentals of surface-enhanced Raman scattering (SERS) and its applications are summarized at the end of the chapter. Several books of molecular spectroscopy have been used for the formulation of this theoretical introduction [8–13].

1.1.1 Quantum Theory

A quantum mechanical system is described by the Schrödinger equation:

$$H_0\Psi_0 = -\frac{\hbar}{i}\frac{\partial\Psi_0}{\partial t}. \tag{1.2}$$

A perturbation to this state is described by introducing an additional term, the *interaction operator* H_{int},

$$(H_0 + H_{int})\Psi = -\frac{\hbar}{i}\frac{\partial\Psi}{\partial t}. \tag{1.3}$$

The solution of the perturbed system can be written as a superposition of the eigenstates of the unperturbed one:

$$\Psi(\vec{r},t) = -\sum_k a_k(t)\Psi_k(\vec{r},t), \tag{1.4}$$

where the coefficients $a_k(t)$ are time-dependent weighting factors, and $a_k^*(t)a_k(t)$ gives the probability of finding the system in state k. From Eqs. 1.3 and 1.4 it follows that

$$(H_0 + H_{int})\sum_k a_k(t)\Psi_k(\vec{r},t) = -\frac{\hbar}{i}\sum_k \dot{a}_k(t)\Psi_k(\vec{r},t) - \frac{\hbar}{i}\sum_k a_k(t)\dot{\Psi}_k(\vec{r},t). \tag{1.5}$$

Since $\Psi_k(\vec{r},t)$ are the solutions of the Schrödinger equation for the system without perturbation, it follows that

$$H_{int}\sum_k a_k(t)\Psi_k(\vec{r},t) = -\frac{\hbar}{i}\sum_k \dot{a}_k(t)\Psi_k(\vec{r},t). \tag{1.6}$$

The wavefunctions $\Psi_k(\vec{r},t)$ are orthonormal; so Eq. 1.6 after being multiplied with $\Psi_m^*(\vec{r},t)$ from the left and integrated over all space gives

$$\dot{a}_m(t) = -\frac{i}{\hbar}\sum_k a_k(t)\int \Psi_m^*(\vec{r},t)H_{int}\Psi_k(\vec{r},t)d\vec{r}. \tag{1.7}$$

If the wavefunction $\Psi_k(\vec{r},t)$ is written as the product of a time-dependent and a space-dependent term $\psi_k(\vec{r})\exp(\frac{-i}{\hbar}E_k t)$, it yields

$$\dot{a}_m(t) = -\frac{i}{\hbar}\sum_k a_k(t)\exp\left\{\frac{i}{\hbar}(E_m - E_k)t\right\}\int \psi_m^*(\vec{r})H_{int}\psi_k(\vec{r})d\vec{r}, \tag{1.8}$$

where

$$\int \psi_m^*(\vec{r}) H_{int} \psi_k(\vec{r}) d\vec{r} = \langle m|H_{int}|k\rangle \tag{1.9}$$

is the matrix element of the operator H_{int} between the states m and k. With the Dirac bra-ket notation, equation 1.8 is given by

$$\dot{a}_m(t) = -\frac{i}{\hbar}\sum_k a_k(t)\exp\left\{\frac{i}{\hbar}(E_m - E_k)t\right\}\langle m|H_{int}|k\rangle. \tag{1.10}$$

Now, rewriting

$$a_k(t) = b_k(t)\exp\left(\frac{i}{\hbar}E_k t\right) \tag{1.11}$$

a set of homogeneous differential equations are obtained

$$\dot{b}_m(t) = -\frac{i}{\hbar}\Big\{E_m b_m(t) + \sum_k b_k(t)\langle m|H_{int}|k\rangle\Big\}, \quad \text{with} \quad m = 1, 2, ... \tag{1.12}$$

Assuming that the time-dependent factor of H_{int} is either constant within an interval $0 \leq t \leq \theta$ or proportional to $\exp(i\omega t) + \exp(-i\omega t)$, this system can be solved by any standard method. Introducing $b_k = c_k \exp(\alpha t)$ yields

$$-\Big(\frac{i}{\hbar}\alpha + E_m\Big)c_m = \sum_k c_k\langle m|H_{int}|k\rangle, \quad \text{with} \quad m = 1, 2, ... \tag{1.13}$$

This system of equations can be solved if the determinant of the coefficients is equal to zero:

$$\begin{vmatrix} -E_1 - \frac{i}{\hbar}\alpha & \cdots & \langle n|H_{int}|1\rangle \\ \langle 1|H_{int}|2\rangle & \ddots & \\ \cdots & -E_k - \frac{i}{\hbar}\alpha & \cdots \\ & & \ddots \\ \langle 1|H_{int}|n\rangle & \cdots & -E_n - \frac{i}{\hbar}\alpha \end{vmatrix} = 0. \tag{1.14}$$

Supposing that the perturbation caused by the interaction of the e.m. radiation with the molecule is small, Eq. 1.14 can be expanded up to second order in the matrix element of the operator H_{int}, resulting in

$$\frac{i}{\hbar}\alpha = -E_l + \sum_{k\neq l}^{n}\frac{\langle m|H_{int}|l\rangle\langle l|H_{int}|k\rangle}{E_k - E_l}, \quad \text{with} \quad l = 1, 2, ... \tag{1.15}$$

After determining c_k and b_k, an expression for a_k can be derived with the eigenvalues of Eq. 1.14:

$$a_k(t) = \frac{\langle m|H_{int}|k\rangle}{E_m - E_k}\Big\{1 - \exp\Big[\frac{i}{\hbar}(E_k - E_m)t\Big]\Big\} \tag{1.16a}$$

$$+ \frac{1}{E_m - E_k}\sum_{l>k}^{n}\frac{\langle m|H_{int}|l\rangle\langle l|H_{int}|k\rangle}{E_m - E_l}\Big\{1 - \exp\Big[\frac{i}{\hbar}(E_k - E_m)t\Big]\Big\} \tag{1.16b}$$

$$+ \sum_{l>k}^{n}\frac{\langle m|H_{int}|l\rangle\langle l|H_{int}|k\rangle}{(E_m - E_l)(E_l - E_k)}\Big\{1 - \exp\Big[\frac{i}{\hbar}(E_k - E_m)t\Big]\Big\}. \tag{1.16c}$$

The first term of equation 1.16 describes the transition from an initial state m to a final state k due to emission or absorption of radiation, respectively. The terms 1.16b and 1.16c contain transition matrix elements to all other electronic states (with index l). They are important, e.g., for Raman scattering.

1.1.2 Interaction with the Dipole Moment

In this subsection, direct absorption or emission is studied; hence, the transition dipole moment of the system and the first term of equation 1.16 which describes the transition from an initial state m to a final state k due to emission or absorption of a photon will be considered.

The interaction of the electric field of the light, $\vec{E} = \vec{E_0}[\exp(-i\omega t) + \exp(i\omega t)]$, with the dipole moment operator of the molecules, $\vec{\mu} = \sum_j e_j \vec{r_j}$ (j being an index for the electrons), can be expressed as

$$H_{int} = \vec{E}\vec{\mu} = \vec{E_0}[\exp(-i\omega t) + \exp(i\omega t)]\vec{\mu}. \tag{1.17}$$

The maximum of H_{int} occurs when the electric-field vector is parallel to the dipole moment, and no light will be absorbed when $\vec{E}$ is perpendicular to $\vec{\mu}$.

After the introduction of this H_{int} in Eq. 1.10 and separation of the time-dependent factor of $\vec{E}$, the term 1.16a can be rewritten as

$$\begin{aligned} a_k(t) = {} & \frac{\langle m|\vec{\mu}|k\rangle}{E_m - E_k + \hbar\omega}\Big\{1 - \exp\Big[\frac{i}{\hbar}(E_k - E_m + \hbar\omega)t\Big]\Big\}\vec{E_0} \\ & + \frac{\langle m|\vec{\mu}|k\rangle}{E_m - E_k - \hbar\omega}\Big\{1 - \exp\Big[\frac{i}{\hbar}(E_k - E_m - \hbar\omega)t\Big]\Big\}\vec{E_0}. \end{aligned} \tag{1.18}$$

For the absorption of radiation, e.g. a transition from k to m, equation 1.18 simplifies to

$$a_k(t) = \langle m|\vec{\mu}|k\rangle\vec{E_0}\,\frac{1 - \exp[\frac{i}{\hbar}(E_k - E_m - \hbar\omega)t]}{E_k - E_m - \hbar\omega}. \tag{1.19}$$

With $\exp(-i\omega t) + \exp(i\omega t) = 2\cos\omega t$, the probability for the transition at a given frequency reads

$$a_k^*(t)a_k(t) = 4|\langle m|\vec{\mu}|k\rangle|^2\vec{E_0}^2\,\frac{[\sin\frac{1}{2\hbar}(E_k - E_m - \hbar\omega)t]^2}{(E_k - E_m - \hbar\omega)^2}, \tag{1.20}$$

and integrating over the whole frequency range yields

$$a_k^*(t)a_k(t) = \frac{1}{\hbar^2}|\langle m|\vec{\mu}|k\rangle|^2\vec{E_0}^2 t. \tag{1.21}$$

1.1.3 Experimental Quantities

The elements of equation 1.21 can be related with experimental quantities. First, the amplitude of the incident radiation can be written in terms of its energy density $\rho = (3/2\pi)E_0^2$, and the following transition probability results

$$a_k^*(t)a_k(t) = \frac{2\pi}{3\hbar^2}|\langle m|\vec{\mu}|k\rangle|^2\rho t. \tag{1.22}$$

Second, not only one molecule but a number N_0 per unit volume (cm^3) will be considered. For a sample of thickness dl, the change of intensity dI of the radiation passing through it is given by the relation:

$$-dI = \frac{2\pi}{3\hbar^2}|\langle m|\vec{\mu}|k\rangle|^2\rho\hbar\omega_{km}N_0 dl, \tag{1.23}$$

where $\hbar\omega_{km}$ is the energy absorbed in a single transition between states k and m.

Furthermore, since I is the energy flowing through unit area per unit time, it can be expressed in terms of the energy density as

$$I = c\rho, \tag{1.24}$$

where c is the velocity of propagation of the radiation. Thus Eq. 1.23 appears as

$$-dI = \frac{2\pi}{3\hbar^2}|\langle m|\vec{\mu}|k\rangle|^2\frac{I}{c}\ \hbar\omega_{km}N_0 dl. \tag{1.25}$$

The *Bouguer-Lambert-Beer law* forms the mathematical-physical basis of light absorption measurements in the UV-VIS and IR region. This law relates the decrease in intensity of the radiation as it penetrates a distance dl in an absorbing sample, and reads

$$-dI = \alpha(\omega)IXdl, \tag{1.26}$$

where X is the molar concentration and $\alpha(\omega)$ the *absorption coefficient.*

For comparison with the experimental expression, Eq. 1.26, it is necessary to find the relation between N_0 and the molar concentration. Using the Avogadro's number N_A, the relation reads

$$N_0 = \frac{N_A X}{1000}, \tag{1.27}$$

and Eq.1.25 can be written

$$-dI = \Big(\frac{2\pi 10^{-3}}{3\hbar^2 c}|\langle m|\vec{\mu}|k\rangle|^2 N_A\hbar\omega_{km}\Big)IXdl. \tag{1.28}$$

This expression allows us to identify $\alpha(\omega)$.

The absorption band for a given transition usually extends over a range of frequencies. The total intensity of the band is obtained by measuring and integrating $\alpha(\omega)$ in the region of the absorption:

$$\Omega = \int_{band} \alpha(\omega) d\omega. \tag{1.29}$$

The integrated form of Beer's law is given by

$$\ln \frac{I_0}{I} = \ln \frac{1}{T} = \alpha(\omega) X l \quad \longrightarrow \quad \log \frac{I_0}{I} = \log \frac{1}{T} = \alpha\,'(\omega) X l = A, \tag{1.30}$$

where I_0 is the intensity of the radiation before and I after passing through the sample, $T = I/I_0$ is the *transmittance*, and A the *absorbance*, which is given in units of the optical density ($OD = \log(I_0/I)$).

1.1.4 Selection Rules

The results of the previous subsection provide a quantitative relationship between the transition moment of the corresponding absorbing molecule and the absorption of the radiation. But also qualitative statements can be made about which transitions can be induced by the electromagnetic radiation. These are given by the so-called *selection rules*, and for a given system they can be obtained by calculating for which transitions the integral $\langle m|\vec{\mu}|k\rangle$ is zero. These *selection rules* will be calculated for every specific problem.

1.2 UV-Visible or Electronic Spectroscopy

The absorption of a UV-VIS photon results in an electronic transition of a molecule, in which an electron is promoted from the ground state to higher electronic states, usually from the HOMO (Highest Occupied Molecular Orbital) to the LUMO (Lowest Unoccupied Molecular Orbital).

The vast majority of valence electrons are either σ electrons, which are strongly bound, or π electrons, which are less firmly bound, or n electrons, which are not part of a molecular bond. Single bonds contain σ electrons only, whereas multiple bonds contain π electrons as well as σ electrons. The ionization energies follow the relation $E_\sigma > E_\pi > E_n$, so the electronic transition usually originates from n or π electrons in a chromophore. The corresponding transitions in the different wavelength ranges are generalized and schematically presented in Fig. 1.2.

If in a molecule $\langle m|\vec{\mu}|k\rangle \neq 0$, the corresponding transition will be allowed (high absorption), if not, the transition will be forbidden (low absorption).

The absorption of compounds or ions containing transition metals have been long used to characterize these species empirically. Many of these systems are colored, i.e. they

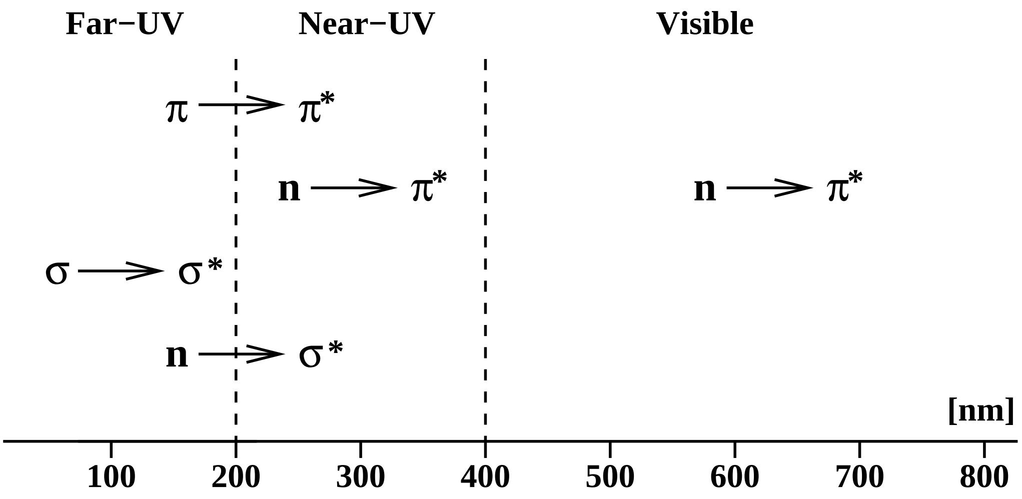

FIG. 1.2. Regions of the electronic spectrum and corresponding types of transitions.

have electronic transitions that result in absorption in the visible region. The analysis of such absorption bands in terms of the electronic states involved leads to further understanding of the bonding in these coordination compounds.

1.3 Vibrational Levels

Both IR and Raman spectroscopy usually investigate the vibrational transitions of the molecules. In this section, the vibrational levels and their interaction with light are discussed, before going into details of every spectroscopic technique. The e.m. wave is characterized by its wavelength or frequency, which are related to each other by

$$\lambda = \frac{c}{\nu}, \tag{1.31}$$

where c is the velocity of light in vacuum. The wavelength λ is usually expressed in nm. The frequency ν is expressed as the number of cycles per second (Hz). It can also be characterized by the wavenumber $\tilde{\nu}$, in cm^{-1}, where

$$\tilde{\nu} = \frac{\nu}{c} \quad \longrightarrow \quad \tilde{\nu} = \frac{1}{\lambda} \;\; [\mathrm{cm}^{-1}]. \tag{1.32}$$

The vibrational energy levels of a molecule are calculated with the model of the harmonic oscillator. From the Schrödinger equation of the harmonic oscillator, its eigenvalues can be obtained, i.e. the energy values corresponding to the consecutive energy levels determined by the vibrational quantum numbers ($v = 0, 1, 2, \dots$). They can be written

$$E = h\nu_0(v + \frac{1}{2}), \tag{1.33}$$

where ν_0 is the classical eigenfrequency of the harmonic oscillator. This frequency is given by

$$\nu_0 = \frac{1}{2\pi}\sqrt{\frac{f}{m_r}}, \tag{1.34}$$

where f is the force constant and m_r the reduced mass.

But a vibrating molecule does not behave exactly as a harmonic oscillator (equidistant energy levels); it can be more accurately described in terms of an anharmonic oscillator (non-equidistant energy levels). The selection rule for the harmonic oscillator is

$$\Delta v = \pm 1, \tag{1.35}$$

so that the only possible transitions are those between neighboring energy levels.

The analogous selection rule for the anharmonic oscillator has the form

$$\Delta v = \pm 1, \pm 2, \pm 3, \ldots \tag{1.36}$$

In addition to the *fundamental* transitions $\Delta v = \pm 1$, there are additional transitions $\Delta v = \pm 2, \pm 3, \cdots \pm n$, which are called *overtones.*

A harmonic oscillator can be assigned to each normal vibration of the molecule. A molecule of 3N-6 vibrational degrees of freedom is represented by 3N-6 oscillators. In the vibrational spectra of polyatomic molecules, also *combinational modes* can be observed in addition to the fundamentals and the overtones. The frequencies of these combinational bands are the sums or the differences of the frequencies of the fundamentals or overtones.

It is also possible to observe the phenomenon of *Fermi resonance* between coupled molecular oscillators. The condition required for this type of resonance are identical, or almost identical, frequencies of the fundamental mode of one oscillation and of an overtone or a combinational mode of the other vibration and identical symmetry of them. Then, instead of the fundamental mode, two bands of slightly different frequencies can be observed.

The intensities of individual bands in the spectrum of a compound are related to the probability of transition between the corresponding vibrational levels and the populations of the initial levels, which depend on temperature. The dependency on temperature is given by the Boltzmann distribution and has the form

$$N_v = N_0 \ \exp\left(\frac{-(E_v - E_0)}{k_B T}\right), \tag{1.37}$$

where N_v denotes the number of molecules in the vibrational level with quantum number v, N_0 the number of molecules in the lowest vibrational level ($v = 0$), k_B the Boltzmann constant, T the absolute temperature, and E_v and E_0 are the energies of the vibrational levels characterized by the quantum numbers v and 0, respectively.

1.4 Infrared Spectroscopy

It has been noted that the covalent bonds of molecules are not rigid, but are like stiff springs that can be stretched and bent. Transitions between vibrational energy states may be induced by absorption of infrared radiation, whose photons have the appropriate energy. The stretching vibrations appear at higher wavenumbers than the bending vibrations, since more energy is required to stretch (compress) a bond than to bend it. The transition probability of infrared absorption is given by Eq. 1.21

$$a_k^*(t)a_k(t) = \frac{1}{\hbar^2}|\langle m|\vec{\mu}|k\rangle|^2 \vec{E_0}^2 t. \tag{1.38}$$

The vibrations of a molecule result only in small deviations of the bond from its equilibrium length. Hence, the dipole moment can be expanded as a power series in the displacement r around the equilibrium value r_0

$$\langle m|\vec{\mu}|k\rangle = \int \psi_m^* \Big[\vec{\mu_0} + \Big(\frac{\partial \mu}{\partial r}\Big)_{r=r_0}(r - r_0)\Big]\psi_k d\vec{r} \sim \frac{\partial \vec{\mu}}{\partial r}\int \psi_m^* r \; \psi_k d\vec{r}. \tag{1.39}$$

The zero order of the expansion makes the integral non-zero only for $m = k$, so no transition is taking place. For the second term, due to the orthogonality of the wavefunctions, the integral will only be $\neq 0$ for $k = m+1$, which corresponds to a transition from a lower-energy level m to the next higher level ($k = m+1$). In addition, a change in the dipole moment connected with the vibration is necessary to obtain a non-zero transition and, hence, absorption:

$$\langle m|\vec{\mu}|k\rangle \neq 0 \quad \text{if} \quad \frac{\partial \vec{\mu}}{\partial r} \neq 0, \quad \text{for} \quad k = m + 1. \tag{1.40}$$

Hence, it is evident that not all molecular vibrations lead to observable infrared absorption. In general, a vibration must cause a change in the electric dipole moment within a molecule to absorb infrared light. The greater this change is, the stronger will be the absorption.

1.5 Raman Spectroscopy

1.5.1 The Raman Effect

The Raman effect can be understood as a scattering process of photons on molecules. If the scattering occurs without change in the energy of the incident photon, the interaction is called elastic or *Rayleigh scattering*, and if it involves a change of this energy, inelastic or *Raman scattering* (see Fig. 1.3).

Before the scattering process, the photon has an energy $E_0 = h\nu_0$ and a momentum $p_0 = h\nu_0/c$, and the molecule of mass M is in an energy level E_k and has a velocity v_0.

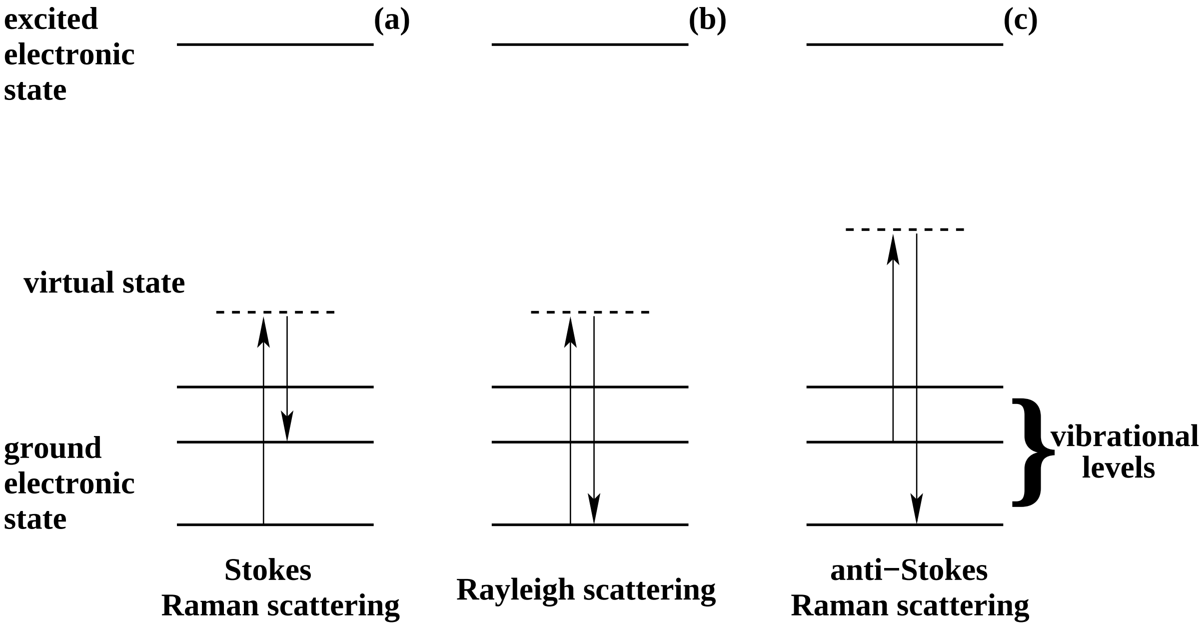

FIG. 1.3. Energy level diagram of Raman scattering with monochromatic light.

After the process, these quantities are modified to $E' = h\nu'$, $p' = h\nu'/c$ for the photon and E_m and v' for the molecule. Thus, the conservation of energy requires

$$h\nu_0 + \frac{Mv_0^2}{2} + E_k = h\nu' + \frac{Mv'^2}{2} + E_m. \tag{1.41}$$

The change in the kinetic energy of the molecule caused by the scattering process is negligible as compared with the total exchange of energy, $|h(\nu_0 - \nu')| >> M/2(v_0^2 - v'^2)$, so Eq. 1.41 can be simplified to

$$h\Delta\nu = h(\nu_0 - \nu') = E_m - E_k. \tag{1.42}$$

The photon energy of the scattered light may be smaller, equal to or larger than that of the incident radiation. If the energy is smaller,

$$h\Delta\nu = h(\nu_0 - \nu') > 0 \quad \longrightarrow \quad E_m > E_k, \tag{1.43}$$

this implies that the initial energy level was lower than the final level. The difference energy is used to induce a transition from the vibrational level k to level m. This correspond to the *Stokes* lines in the Raman spectrum (see Fig. 1.3 (a)).

If the photon energy does not change,

$$h\Delta\nu = h(\nu_0 - \nu') = 0 \quad \longrightarrow \quad E_m = E_k, \tag{1.44}$$

it means that the energy levels of the molecule before and after the collision are the same, and *Rayleigh* scattering occurs (see Fig. 1.3 (b)).

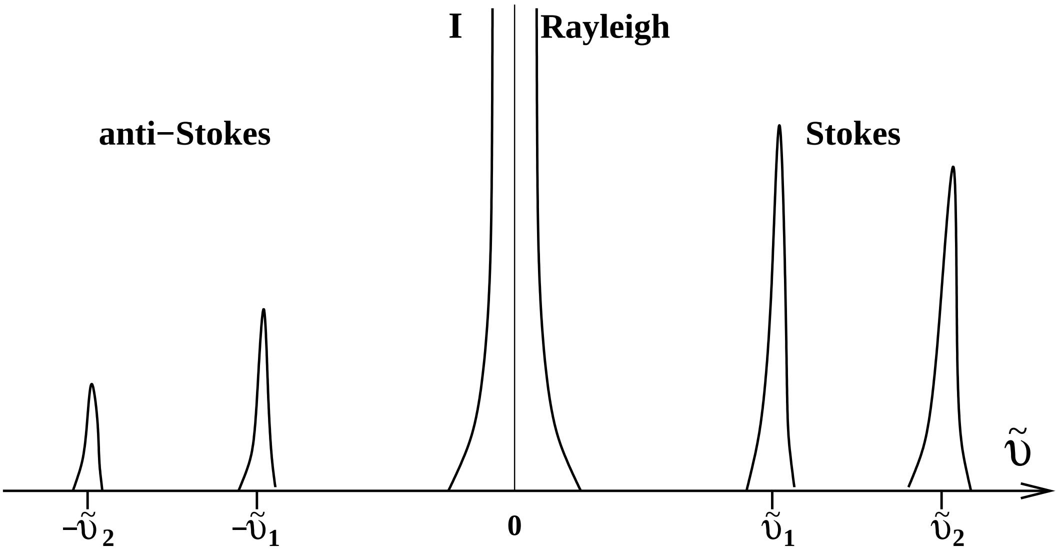

FIG. 1.4. Part of a Raman spectrum (sketch).

Finally, if the photon energy increases,

$$h\Delta\nu = h(\nu_0 - \nu') < 0 \quad \longrightarrow \quad E_m < E_k, \tag{1.45}$$

the additional energy is due to a transition from a higher vibrational level k to a lower level m, and the process contributes to the *anti-Stokes* lines (see Fig. 1.3 (c)).

A part of a Raman spectrum is schematically shown in Fig. 1.4. The intensity of the scattered lines is plotted vs. the wavenumber shift or Raman shift:

$$\tilde{\nu} = \Delta\nu/c = (\nu_0 - \nu')/c, \quad \text{in} \quad \text{cm}^{-1}. \tag{1.46}$$

The Rayleigh line corresponds to a Raman shift of zero, since $\nu' = \nu_0$. The intensity of the Rayleigh line is 10^5-10^6 times higher than that of the accompanying Raman bands. The absolute differences between the frequencies of the incident photon and the Stokes and anti-Stokes photons are the same and equal to the molecular vibration frequency:

$$\begin{array}{rlll} \text{Stokes} & h\nu_0 - h\nu' = h\nu_{vib} & \longrightarrow & \nu_0 - \nu'(St) = \nu_{vib} \\ \text{anti-Stokes} & h\nu_0 - h\nu' = -h\nu_{vib} & \longrightarrow & \nu'(aSt) - \nu_0 = \nu_{vib} \end{array} \tag{1.47}$$

This shows that the frequency difference between the exciting and the scattered radiation is characteristic of a molecule and independent of the frequency of the exciting radiation.

According to the Boltzmann law, only a small portion of the molecules will occupy the first excited vibrational state at room temperature. Most of the molecules are in the ground state and, as a consequence, the intensity of anti-Stokes lines will be much lower than that of the Stokes lines. Therefore, Raman spectroscopy usually involves measurement of the Stokes side.

The Raman intensity is directly proportional to the number of scattering molecules per unit volume, i.e., to the volume concentration of the substance.

Now, to derive the necessary conditions for the occurrence of Raman scattering, the interaction of the light with the dipole moment it induces in the molecules has to be studied. The incident radiation can be represented by the electric field vector $\vec{E}$,

$$\vec{E} \;=\; \vec{E_0}\cos\;2\pi\nu_0 t \tag{1.48}$$

which excites the molecular electron cloud to oscillations with angular frequency $2\pi\nu_0$ and induces a dipole moment $\vec{\mu}$ which can be related to the electric field vector via

$$\vec{\mu} = \underline{\underline{\alpha}}\vec{E} \;=\; \underline{\underline{\alpha}}\vec{E_0}\cos\;2\pi\nu_0 t = \;\underline{\underline{\alpha}}\vec{E_0}\cos\;\omega_0 t, \tag{1.49}$$

where $\underline{\underline{\alpha}}$ is the *polarizability.* With the exception of isotropic molecules (for example CCl_4) the molecular polarizability shows tensor properties, and the induced dipole moment $\vec{\mu}$ is, in general, not parallel to the electric field $\vec{E}$.

It can be written as

$$\begin{pmatrix} \mu_x \\ \mu_y \\ \mu_z \end{pmatrix} = \begin{pmatrix} \alpha_{xx} & \alpha_{xy} & \alpha_{xz} \\ \alpha_{yx} & \alpha_{yy} & \alpha_{yz} \\ \alpha_{zx} & \alpha_{zy} & \alpha_{zz} \end{pmatrix} \begin{pmatrix} E_x \\ E_y \\ E_z \end{pmatrix} = \vec{\mu} = \underline{\underline{\alpha}}\vec{E}, \tag{1.50}$$

where α_{ij} are the components of the tensor $\underline{\underline{\alpha}}$.

Considering that the vibrations of a molecule result only in small deviations of the bonds from their equilibrium lengths, the polarizability can be expanded as a power series in the displacement r around the equilibrium value r_0,

$$\underline{\underline{\alpha}} = \underline{\underline{\alpha_0}} + \left(\frac{\partial\underline{\underline{\alpha}}}{\partial r}\right)_{r=r_0}(r-r_0)\;\cos 2\pi\nu_{vib}t, \tag{1.51}$$

and the induced dipole moment reads

$$\begin{aligned} \vec{\mu} = \;& \underline{\underline{\alpha_0}}\vec{E_0}\cos\;2\pi\nu_0 t + \frac{1}{2}\left(\frac{\partial\underline{\underline{\alpha}}}{\partial r}\right)_{r=r_0}(r-r_0)\vec{E_0}\cos\;2\pi(\nu_0-\nu_{vib})t \\ & +\frac{1}{2}\left(\frac{\partial\underline{\underline{\alpha}}}{\partial r}\right)_{r=r_0}(r-r_0)\vec{E_0}\cos\;2\pi(\nu_0+\nu_{vib})t. \end{aligned} \tag{1.52}$$

According to Eq. 1.52 there is one component of the induced dipole which oscillates with the frequency of the incident light, resulting in Rayleigh scattering, the second component oscillates with $\nu_0-\nu_{vib}$ (Stokes), and the third one with $\nu_0+\nu_{vib}$ (anti-Stokes). The latter two are only present if

$$\frac{\partial\underline{\underline{\alpha}}}{\partial r} \neq 0, \tag{1.53}$$

i.e., if the polarizability changes during the vibration.

Coming back to the quantum-mechanical description of Section 1.1.1, we consider the term of Eq. 1.16b which describes a transition from state m to state k and contains transition matrix elements to all other electronic states (with index l):

$$a_k^{Raman}(t) = \frac{1}{E_m - E_k} \sum_{l>k}^{n} \frac{\langle m|H_{int}|l\rangle\langle l|H_{int}|k\rangle}{E_m - E_l} \Big\{1 - \exp\Big[\frac{i}{\hbar}(E_k - E_m)t\Big]\Big\}. \tag{1.54}$$

Inserting the interaction of the electric field of the light with the dipole moment of the molecules, $H_{int} = \vec{E}\vec{\mu} = \vec{E_0}[\exp(-i\omega t) + \exp(i\omega t)]\vec{\mu}$, Eq. 1.54 can be expressed as

$$\begin{aligned} a_k^{Raman}(t) = & \frac{\vec{E_0}^2\Big\{1 - \exp\Big[\frac{i}{\hbar}(E_k - E_m + \hbar\omega)t\Big]\Big\}}{E_m - E_k + \hbar\omega} \sum_{l>k}^{n} \frac{< m|\vec{\mu}|l >< l|\vec{\mu}|k >}{E_m - E_l + \hbar\omega} \\ + & \frac{\vec{E_0}^2\Big\{1 - \exp\Big[\frac{i}{\hbar}(E_k - E_m - \hbar\omega)t\Big]\Big\}}{E_m - E_k - \hbar\omega} \sum_{l>k}^{n} \frac{< m|\vec{\mu}|l >< l|\vec{\mu}|k >}{E_m - E_l - \hbar\omega}. \end{aligned} \tag{1.55}$$

Thus, the probability for a transition from a lower state m to a higher state k is given by

$$\begin{aligned} a_k^*(t)a_k(t)^{Raman} = & \frac{\vec{E_0}^4}{(E_m - E_k - \hbar\omega)^2} \underline{\underline{\alpha}}_{mk}^2 \\ & \cdot \Big\{2 - \exp\Big[\frac{i}{\hbar}(E_k - E_m - \hbar\omega)t\Big] - \exp\Big[\frac{-i}{\hbar}(E_k - E_m - \hbar\omega)t\Big]\Big\} \\ = & \frac{4\vec{E_0}^4 \sin^2\Big[\frac{1}{2\hbar}(E_k - E_m - \hbar\omega)t\Big]}{(E_m - E_k - \hbar\omega)^2} \underline{\underline{\alpha}}_{mk}^2, \end{aligned} \tag{1.56}$$

where

$$\underline{\underline{\alpha}}_{mk} = \sum_l \frac{< m|\vec{\mu}|l >< l|\vec{\mu}|k >}{E_m - E_l + \hbar\omega} \tag{1.57}$$

is called the *polarizability* or *scattering* tensor for the discussed transition from m to k. The components of this tensor can be written

$$(\alpha_{ij})_{mk} = \sum_l \frac{< m|\vec{\mu_i}|l >< l|\vec{\mu_j}|k >}{E_m - E_l + \hbar\omega}. \tag{1.58}$$

This expression of the scattering tensor elements is only valid under certain conditions:

- the excitation frequency must be much higher than those associated with any vibrational transition of the system, and
- the excitation frequency must be lower than the frequency of any electronic transition.

Under these conditions the scattering tensor is real, symmetric and frequency-independent.

1.5.2 Comparison of Raman and IR Spectroscopy

IR absorption spectroscopy together with Raman spectroscopy will give almost complete information about the vibrational spectrum of a molecule in the ground electronic state. The methods are complementary, which follows from the nature of the phenomena on which they are based.

The complementarity of infrared and Raman spectroscopy results from the different *selection rules* which determine the presence of a band corresponding to a given vibration of the molecule in the infrared and/or Raman spectrum. If the vibration causes a change in the dipole moment, which occurs when the vibration changes the symmetry of the charge density distribution, i.e. if $(\partial\vec{\mu}/\partial r) \neq 0$, it is active in the IR spectrum. If the vibration is connected with a change of the molecular polarizability, i.e. if $(\partial\underline{\underline{\alpha}}/\partial r) \neq 0$, it is active in the Raman spectrum.

The fulfillment of one or both of these conditions is related to the symmetry of the molecule. If the molecule has a center of symmetry, a vibration which is active in the infrared spectrum is inactive in the Raman spectrum and vice versa. This rule is called the *rule of mutual exclusion*. If the molecule does not possess a center of symmetry, a number of vibrations appear in both spectra. The differences between the selection rules of both effects are related to the behavior of an anharmonic oscillator, used as a model for the vibrations of a molecule.

Band intensities in both types of spectra can be predicted with great reliability from some general rules. E.g. non-polar or slightly polar groups tend to have strong Raman lines, whereas strongly polar groups show strong IR absorption. Overtones and combinational bands are stronger in the IR than in the Raman spectrum. In addition, there is a long list of relations for specific types of vibrations of certain molecular groups.

1.5.3 Resonance Raman Spectroscopy

The resonance Raman effect is observed when the frequency of the exciting radiation is very close to, or lies within the range of, an electronic absorption of the molecule (see Fig. 1.5). Under these conditions, the intensities of Raman bands of this chromophore are selectively enhanced by a factor of 10^3 to 10^5. This selectivity is important not only for identifying vibrations of this particular chromophore in a complex spectrum, but also for locating its electronic transitions in a UV-VIS spectrum.

Hence, the resonance Raman spectrum of the molecule provides a fingerprint of the corresponding electronic transition and can be used to identify the ligand which has the lowest energy level in mixed-ligand complexes [14, 15].

According to Eq. 1.58, when $E_l - E_m \approx \hbar\omega$, it appears that the transition polarizability tends to infinity. However, the formula derived in Section 1.5.1 cannot be applied in this case, as it was pointed out previously. In a more general treatment, the lifetimes

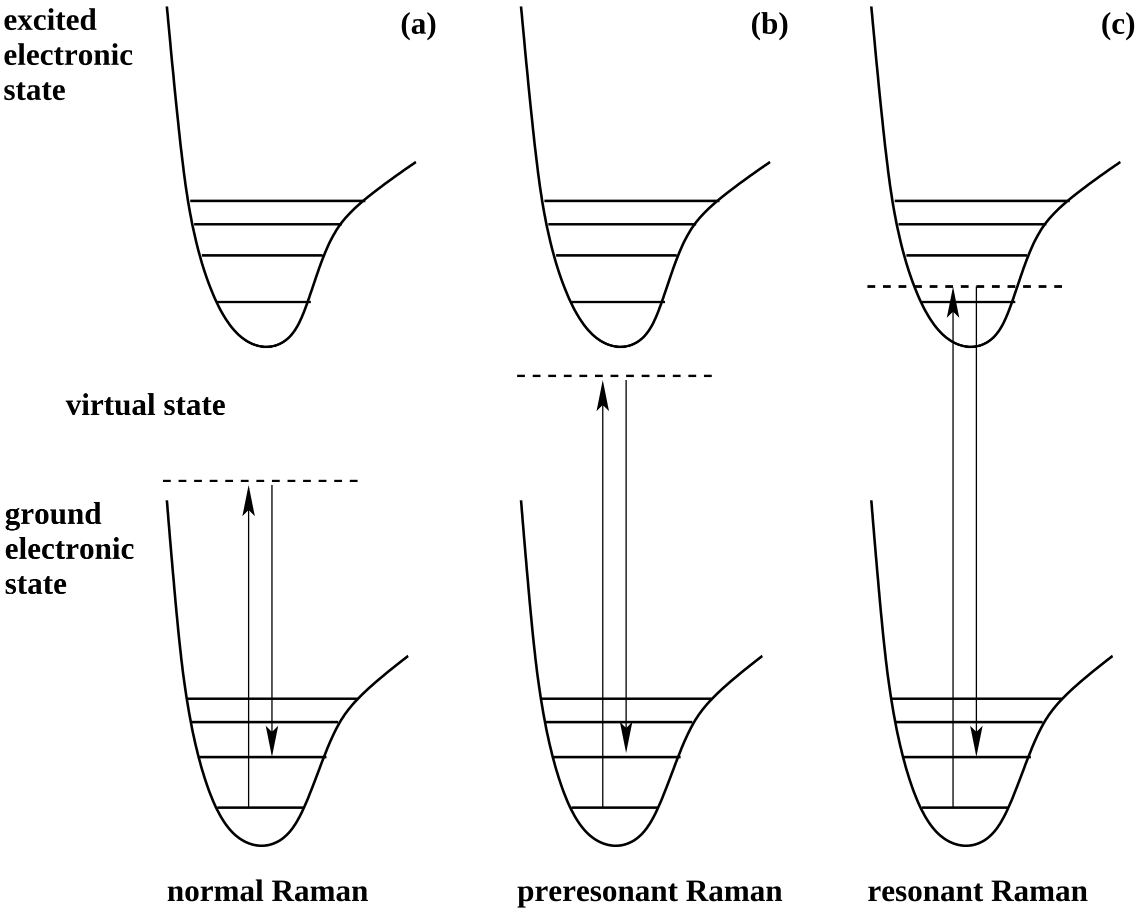

FIG. 1.5. Energy level diagram for **(a)** normal, **(b)** preresonance, and **(c)** resonance Raman scattering.

of the states l have to be taken into account. These states are assumed to decay exponentially with time according to

$$\Psi_l = \psi_l \exp\Big\{-i\Big(\omega_l - \frac{i}{2}\Gamma_l\Big)t\Big\}. \tag{1.59}$$

Then, Eq. 1.58 reads

$$(\alpha_{ij})_{mk} = \sum_l \frac{< m|\vec{\mu_i}|l >< l|\vec{\mu_j}|k >}{E_m - E_l + \hbar\omega - i\Gamma_l}, \tag{1.60}$$

where Γ_l is the spectral width of the l state and $i\Gamma_l$ the so-called *damping constant.*

If it is considered that the total wavefunctions can be written as the product of the electronic and vibrational wavefunctions, the components of the polarizability tensor can be decomposed into two parts:

$$(\alpha_{ij})_{mk} \cong A + B \tag{1.61}$$

The A-term is associated with totally symmetric modes and becomes larger as the denominator becomes smaller (resonance condition). The B-term, which involves two electronic excited states, provides a mechanism of resonance of non-totally symmetric vibrations. In general, B-term enhancement is significantly weaker than that arising from the A-term. Thus, usually the total symmetric modes of a polyatomic molecule are subject to significant Raman resonance enhancement.

It follows from these relations that the resonance effect appears gradually rather than abruptly, when approaching the electronic absorption maximum.

RRS studies can be connected with some disadvantages, since there is always the chance that strong absorption of the exciting radiation may occur and cause decomposition of the sample. Also, the Raman-scattered radiation may be absorbed by the sample itself. If fluorescence appears simultaneously with the resonance Raman signal, it produces a strong background in the recorded spectra.

1.5.4 Surface Enhanced Raman Spectroscopy

Since the Raman effect was discovered by Raman and Krishnan in 1928 [16], the inelastic scattering of photons with matter has been widely used for the investigation of the structure of molecules, crystals, and polymer materials. The cross section of normal Raman scattering, however, is very low. With the invention of the laser (1958) a renaissance of Raman spectroscopy was introduced. It has been shown in the previous subsection that the resonance effect can increase the Raman signal from 3 to 5 orders of magnitude. But after the discovery of surface-enhanced Raman scattering 30 years ago, the investigation of solid surfaces has been greatly stimulated.

The Raman signals can be enhanced by many orders of magnitude when the molecules under investigation are attached to metallic nanostructures or rough surfaces. SERS has been observed on molecules adsorbed on different metals (such as noble, alkali, and transition metals) [17] and also on semiconductors [18, 19], the largest enhancement occurring on silver, gold and copper. The substrates can be rough surfaces, metal island films, UHV cold evaporated films, colloids prepared by chemical reduction, and nanofabricated metal particle arrays [20–22]. The SERS effects are accompanied by strong quenching of fluorescence.

In 1974 Fleischmann and coworkers [23] discovered SERS, although they did not recognized its nature. Three years later Van Duyne and Jeanmaire [24], and simultaneously Albrecht and Creighton [25], recognized that the increase of the intensity was due to a new effect. SERS research was accelerated dramatically in the early 1980s with contributions of chemists, physicists, and engineers from around the world. In 1997, the Nie group [26] and the Kneipp group [27] achieved single-molecule detection via SERS under different experimental conditions.

SERS differs in a number of ways from ordinary Raman spectroscopy and even from unenhanced surface Raman spectroscopy. The intensities of the bands generally fall off with increasing wavenumber. Overtones and combinational bands are not common.

Furthermore, selection rules are relaxed and modes that are normally forbidden appear in the surface-enhanced spectra.

Many mechanisms were proposed in the early days of SERS to account for the differences with respect to the normal Raman spectra. Presently, two mechanisms are generally accepted as the principal causes of the enhancement: the electromagnetic (EM) and the chemical or charge transfer (CT) contribution.

Electromagnetic enhancement

A surface plasmon is a collective oscillation of the conduction electrons which occurs at the surface of solid metals and semiconductors under electromagnetic excitation. Localized plasmon modes can be excited if the surface is composed of small structures such as gratings, spheroidal particles, or just as a consequence of roughness. The electric field of the plasmon has a certain resonance frequency ω_{pl}. In the case of an isolated, small spheroidal metal particle, the plasmon field is dipolar and related to the excitation field E_0 by a factor depending on the ratio of the dielectric constants of both metal and environment, ε_m and ε, respectively, and on the depolarization factor A of the particle:

$$E = \frac{\varepsilon_m(\omega)/\varepsilon(\omega)}{1 + [\varepsilon_m(\omega)/\varepsilon(\omega) - 1]A}\, E_0 = \beta(\omega)E_0. \tag{1.62}$$

This relation describes the field just outside the surface of the particle. The resonance frequency ω_{pl} is determined by the condition

$$Re[\varepsilon_m(\omega_{pl})/\varepsilon(\omega_{pl})] = 1 - 1/A. \tag{1.63}$$

For a sphere $A = 1/3$, so that the resonance condition becomes

$$Re[\varepsilon_m(\omega_{pl})/\varepsilon(\omega_{pl})] = -2. \tag{1.64}$$

EM-SERS is based on the enhancement of the Raman intensity of the vibrating group through two effects: First, the electric field felt by the Raman dipole is enhanced due to the excitation of the plasmon resonance in the adjacent metallic particle. Second, the field of the oscillating Raman dipole itself, which has the frequency $(\omega - \omega_v)$ for the Stokes process, can encounter a further enhancement of the metallic particle field if $(\omega - \omega_v)$ is within the width of the plasmon resonance, where ω_v is the vibrational frequency [28]. Therefore, the Raman intensity will depend on the product of these two enhancement factors, one at the excitation frequency ω and another at $(\omega - \omega_v)$:

$$I \sim |\beta(\omega)\beta(\omega - \omega_v)|^2. \tag{1.65}$$

If ω_v is small as compared to the width of the plasmon resonance, then $I \sim |\beta(\omega)|^4$, and the EM enhancement factor G is given by

$$G = |E|^4/|E_0|^4. \tag{1.66}$$

The EM enhancement is considered the major mechanism responsible for SERS enhancement [29]. It is characterized by the following features:

- It is a long-range effect.
- It is generally independent of the nature of the adsorbed molecule.
- It depends on the electronic structure of the substrate and the roughness of the surface, since the frequencies of the surface-plasmon resonances depend on these factors [30].

SERS surface selection rules have been proposed taking into account only the EM effect. Considering that the molecules are characterized by their Raman tensor $\underline{\underline{\alpha}}$, unaltered by adsorption, and by their orientation with respect to the surface, Otto et al. [31] concluded that the vibrations perpendicular to the surface are more strongly enhanced than the parallel modes. This *SERS propensity rule* is similar to the infrared surface selection rule, which proposes that only vibrations with an oscillating dipole moment perpendicular to the surface are observed.

Chemical enhancement

Not all molecules show SERS effects, but special combinations of adsorbed molecules and metals are required [32]. This cannot be explained with the EM contribution which should be a nonselective amplification mechanism for all molecules. In addition, in potential-dependent electrochemical experiments, resonances seem to occur for specific values of the potential. On the other hand, the enhancement factor generally accepted for the EM mechanism is at most 4 orders of magnitude. But the measured enhancement factors extend to 10^6 or more. The electronic configuration of the chemical species change upon adsorption. Surface-enhancement spectra of molecules in direct contact with a surface are often different from those of the same species in the condensed phase. These observations can be ascribed to the effect of the chemical or charge-transfer enhancement.

The chemical effect is associated with the overlap of metal and adsorbate electronic wavefunctions, which leads to ground-state and light-induced charge-transfer processes. It was proposed by Lombardi et al. [33] amongst other authors, and assumes that the transfer of an electron from the Fermi level of the metal to an unoccupied molecular orbital of the adsorbate or vice versa is possible depending on the energy of the photon and the electric potential at the interface. This CT-SERS effect has been interpreted as a similar process to resonance Raman scattering in which new electronic states arise from chemisorption and serve as resonant intermediate states in the Raman process [34].

The chemical or CT enhancement is characterized by:

- Its short-range nature.
- Its dependency on the adsorbate site, the geometry of binding, and the energy levels of the adsorbed molecule.

The chemical enhancement can provide useful information on adsorption interactions between the metal and the adsorbate. However, this enhancement is not a general mechanism and its applicability is restricted by its chemical specificity [31].

Chapter 2

Experimental Techniques

The fundamentals of the electronic and vibrational spectroscopies used in this thesis have been described in the previous chapter. In the following sections, the instrumentation for the observation of the various spectra will be introduced. Since UV-VIS absorption, IR absorption, and Raman scattering are significantly different techniques, very different instruments are needed for the observation of the corresponding spectra. However, there are similar elements in all these setups:

- A light source to illuminate the sample: monochromatic sources such as lasers or polychromatic lamps.
- A device which separates polychromatic radiation into its spectral components: dispersive monochromators or interferometers.
- A detector to collect and record the resulting spectra: single-channel detectors such as photomultipliers or CCD cameras.

The chapter begins with a general discussion of lasers and dispersive monochromators. In the second part, the specific aspects of the instrumentation and experimental setups for every technique are briefly described. The chapter was written according to Refs. [10–13, 35–37].

2.1 Instrumentation

2.1.1 Lasers

In Raman spectroscopy, continuous wave (cw) lasers emitting radiation in the visible region of the spectrum with a power up to overall hundred milliwatts are generally used. Other laser types are employed for special Raman techniques, e.g. time-resolved Raman spectroscopy.

A laser consists of the following basic elements:

- An active medium, which is to be activated for obtaining laser action.
- A pumping system, which gives rise to population inversion in the energy levels of the active medium.
- An optical resonator.

Depending of the *active medium* used, the laser types can be classified as: gas lasers, e.g. HeNe, Ar, or Kr lasers; solid-state lasers, e.g. ruby or Nd:YAG lasers; semiconductor lasers; organic lasers, and dye lasers.

The most commonly used *pumping methods* or modes of energy transfer causing population inversion are:

- Optical pumping, which consists in exposing the active medium to strong radiation; this radiation is absorbed by the medium and excites it to a higher energy state.
- Electronic pumping, which is usually employed in gas lasers, consists in the excitation of gas atoms or molecules through collisions with electrons or ions in an electrical discharge.
- Collision pumping, in which the atoms or molecules of the active medium are excited with the energy transmitted from other atoms or molecules that were previously excited to an upper energy state in a separate and independent process.
- Pumping through chemical reactions, which results in the excitation of the molecules.

The *optical resonator* or *cavity* consists of (at least) two mirrors and contains the active medium. The resonator has two functions: to establish the conditions for a high degree of stimulated emission in the active medium, and to produce a monochromatic beam with a small angle of divergence.

The generated laser beam is characterized by its narrow spectral line-width, a small cross-section and low divergence, as well as coherence.

In the Raman setup used throughout this thesis (see below) an unpolarized HeNe laser (λ = 632.8 nm) and a linearly polarized frequency-doubled cw Nd:YAG laser (λ = 532 nm) have been employed. Hence, a brief discussion of these two laser sources will be given.

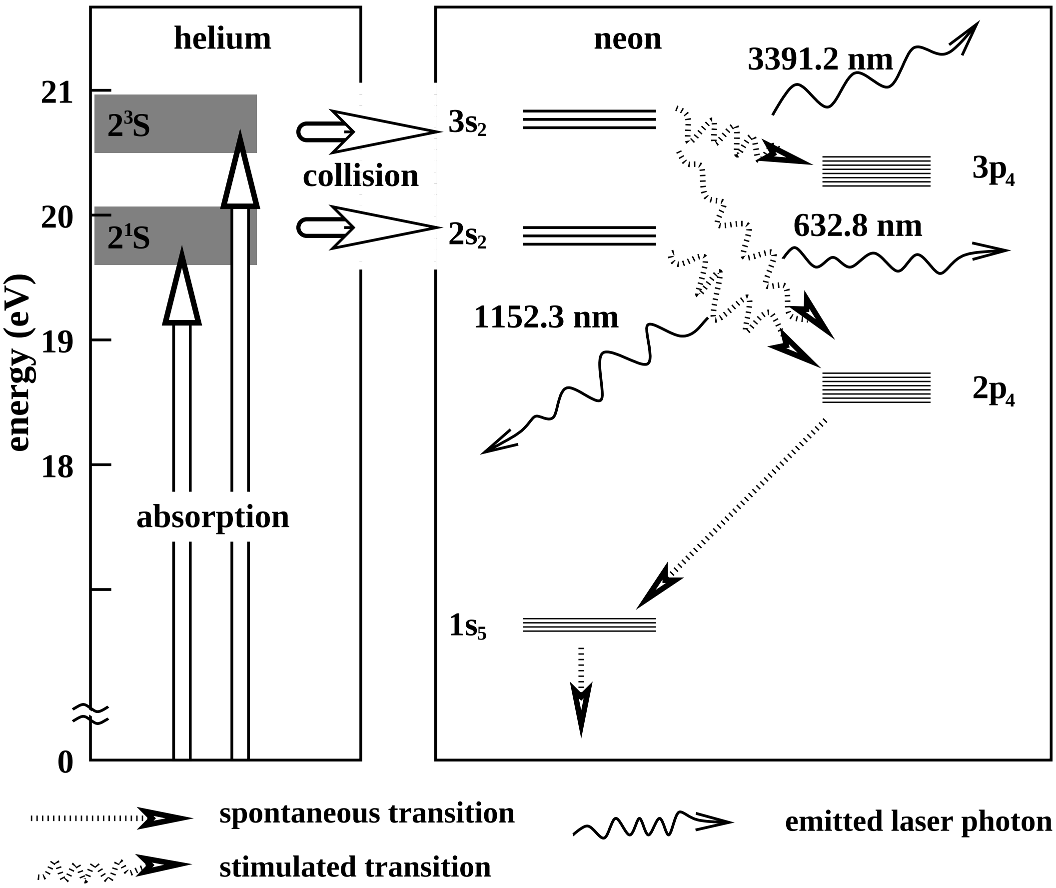

FIG. 2.1. Energy levels and transitions of the He and the Ne atom, which are important for the HeNe laser.

HeNe laser

The HeNe laser was the first gas laser invented [1]. Today it is the most popular continuous-wave gas laser; it provides a few milliwatts of continuous power and the most commonly used wavelength is in the visible part of the spectrum at 632.8 nm. The energy levels of helium and neon atom, the pumping mechanism, and the transitions taking place during operation are schematically depicted in Fig. 2.1.

In Fig. 2.2 the basic components of a noble gas laser are shown. The plasma tube is filled with a mixture of helium and neon gas. In the tube, He atoms are excited by the collisions with electrons in a high-voltage discharge. After energy relaxation from several higher levels, many He atoms accumulate in the long-lived metastable 2^1S- and 2^3S states. The excited helium atoms act as intermediates in the exciting process of the neon atoms, which are the active species of the system. Collisions of the excited He atoms with the ground-state Ne atoms result in the excitation of the latter ones to their $3s_2$- and $2s_2$ states, since the energy levels are very similar. This leads to a population

---

[1] in 1961 by the Iranian physicist Ali Javan and his coworkers W. R. Bennett, Jr. and D. R. Herriot.

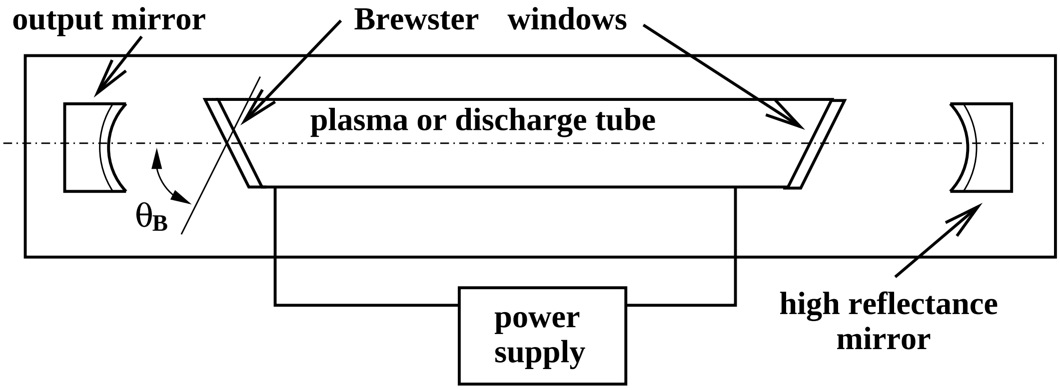

FIG. 2.2. Schematic of a typical gas laser.

inversion with respect to the lower levels $2p_4$ and $3p_4$ of the neon atom. It can be seen in Fig. 2.1 that three laser transitions are obtained: at 3391.3 nm, 1152.3 nm, and 632.8 nm. In most HeNe lasers, the red line is used.

The ends of the plasma tube are often closed with Brewster windows that have an angle defined by the condition $\tan\theta_B = n$, where n is the refractive index of the window material and θ_B Brewster's angle (see Fig. 2.2). In this case, the laser beam is almost completely polarized in a fixed direction. In the Raman setup, an unpolarized laser has been used, in which the mirrors of the cavity are glued directly onto the plasma tube. The resonator cavity is composed of a semi-transparent output mirror and a high reflectance mirror.

Nd:YAG laser

Nd:YAG is an acronym for Neodymium-doped Yttrium Aluminum Garnet. The Nd^{3+} ions in the YAG crystal are excited to a higher energy level by infrared laser diodes. The transition from this state to a lower state produces laser radiation at 1064 nm. The infrared light can be doubled or tripled in order to obtain visible or UV light. The laser used in this thesis contained a nonlinear-optical crystal which performed frequency doubling to 532 nm.

2.1.2 Monochromators

Monochromators are devices that separate polychromatic radiation spatially into its spectral components. In almost all modern dispersive instruments this step is achieved with *diffraction gratings.* A reflection grating is a reflective surface that is ruled, or scratched with parallel lines which are spaced by a distance which is similar to the wavelength of the light to be analyzed.

Incident polychromatic radiation is diffracted by a grating (see Fig. 2.3) according to

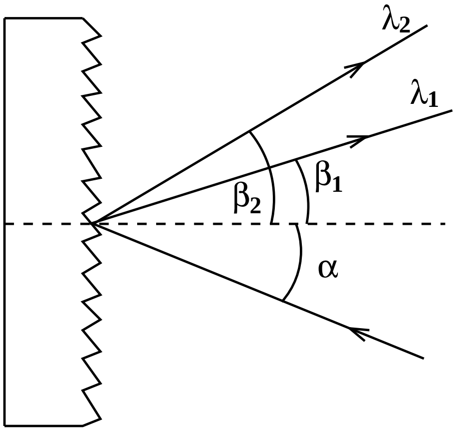

FIG. 2.3. Schematic of a diffraction grating. Rays of light of different wavelengths λ_1 and λ_2 which are incident under the same angle α exit at different angles β_1 and β_2, respectively.

the *grating equation*:

$$d(\sin\alpha + \sin\beta) = m\lambda, \tag{2.1}$$

where λ is the wavelength of the light, α the angle of incidence, β the angle of diffraction, m is an integer known as *diffraction order*, and d the spacing between the rulings. Often, the groove density g of a grating is specified, usually given in mm^{-1}, where $d = 1/g$.

Thus, if parallel polychromatic light reaches the grating under an angle α as shown in Fig. 2.3, the different wavelengths (λ_1 and λ_2) are diffracted off at different angles (β_1 and β_2).

The design of Fig. 2.4 with two spherical mirrors and a plane grating is known as *Czerny-Turner monochromator*. The grating can be rotated, and depending on the angle of the grating different wavelengths are focused into and transmitted through the exit slit. In Czerny-Turner configuration, the incident light is dispersed into its spectral components according to

$$\frac{d\lambda}{dx} = \frac{\cos\beta}{F\ m\ g}, \tag{2.2}$$

where $d\lambda/dx$ is known as the *linear dispersion* of the monochromator and F is its focal length. The linear dispersion indicates the spatial separation of the different wavelengths in the exit focal plane and thus, determines the spectral resolution for a given slit width. The latter equation can be derived from the grating equation, 2.1, by differentiating it with respect to β. Then, rewriting $dx = Fd\beta$ to relate the angular variation with the focal length, Eq. 2.2 is obtained.

This equation indicates that the linear dispersion of a monochromator is not constant but varies with the cosine of the diffraction angle. Therefore it depends on the wavelength of light being measured. If a constant spectral bandpass is to be maintained, the exit slit needs to be adjusted as the wavelength is scanned.

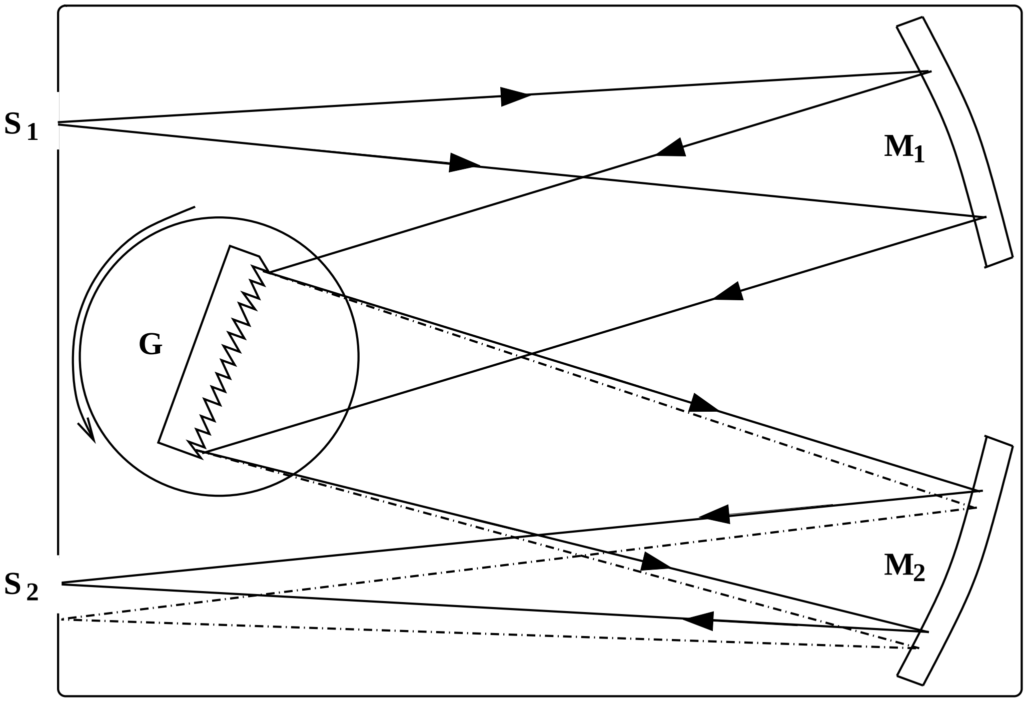

FIG. 2.4. Czerny-Turner monochromator. S_1 and S_2, entrance and exit slits, respectively; G, rotatable grating; M_1 and M_2, spherical mirrors. Different wavelengths are diffracted off the grating at different angles and reach the exit focal plane at different locations. Only one wavelength is transmitted by the exit slit S_2.

Typical infrared (IR) spectral measurements are conducted over a range from 400 to nearly 4000 cm^{-1}. Since the linear dispersion of the monochromator depends on the cosine of the angle of diffraction, as was previously noticed, it is impossible to achieve a reasonably constant bandpass over the wavelength range with the same grating. Instrument designers avoided this problem by using the grating in first and second order, depending on the wavelength investigated. Also many instruments use two gratings mounted on a turret with automatic change at a certain wavelength value.

For dispersive Raman instrumentation, the design requirements are more stringent. First, due to the presence of Rayleigh scattering, which is orders of magnitude more intense than the Raman signals, the rejection of stray light must be very high. Second, since the scattered light is in the visible region, with a relatively small frequency shift, a high resolution is needed. E.g., in IR spectroscopy, for resolving two infrared peaks at 2995 and 3000 cm^{-1}, the resolving power ($\lambda/\Delta\lambda$) needs to be $\sim$ 1000. For separating two Raman lines with 2995 and 3000 cm^{-1} shift from an Ar ion laser line (514 nm), a resolving power of 3000 is needed.

Another configuration is the so-called *Seya Namioka mounting.* In this monochromator the entrance and exit slits are fixed at an angle of about 70° and the transmitted wavelength is varied by the rotation of the concave grating (see Fig. 2.5). This type of monochromator is mainly used in the vacuum UV region.

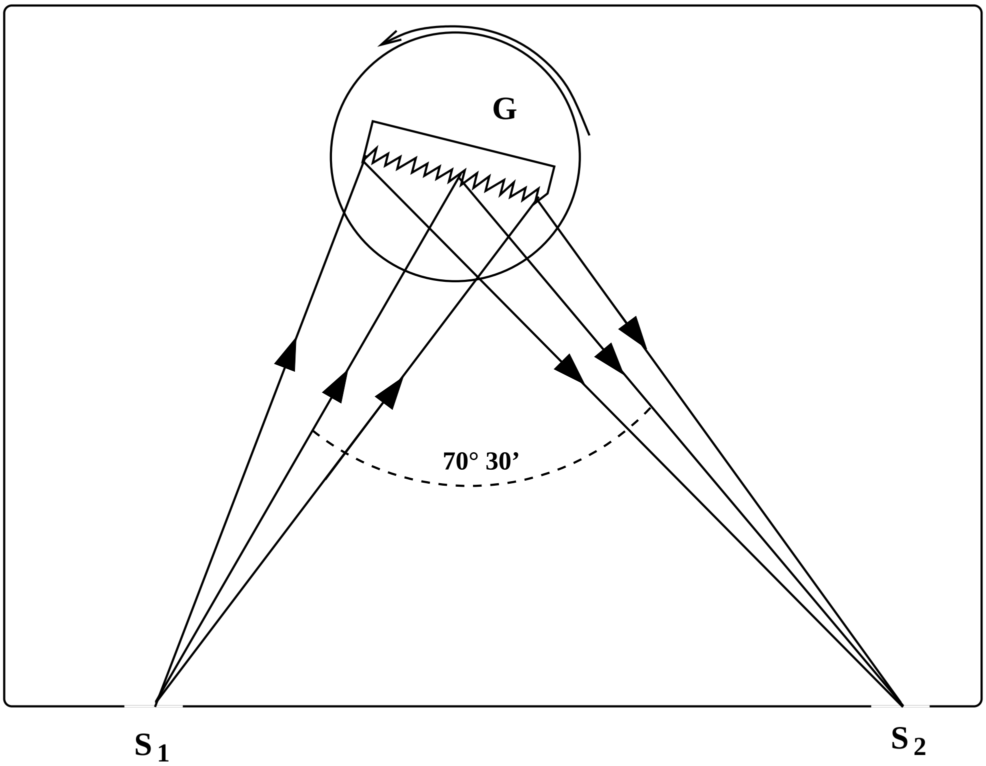

FIG. 2.5. Seya Namioka monochromator. S_1 and S_2, entrance and exit slits, respectively; G, rotatable concave grating.

2.2 UV-VIS Spectroscopy

UV-VIS absorption spectroscopy was performed with a double-beam Perkin-Elmer UV/VIS/NIR spectrophotometer. Sample illumination was performed with prealigned deuterium and tungsten sources. The spectrometer consisted of a Seya Namioka monochromator (see Fig. 2.5), with a concave holographic grating with 1053 lines per mm.

In double-beam instruments, the light is split and directed along two paths which go through the reference and the sample cuvette, respectively.

For UV-VIS absorption spectroscopy, a continuous source from 190 nm to 900 nm is needed. In the visible range of the spectrum, this requirement is fulfilled by the *tungsten lamp* which is (approximately) a black-body radiator; hence, its spectral energy distribution is described by Planck's formula:

$$S_\nu = \frac{8\pi h}{c^3}\frac{\nu^3}{e^{h\nu/kT}-1}, \tag{2.3}$$

where S_ν is the radiated energy per unit volume and unit frequency.

Like other technical black-body sources, the spectral energy distribution of a tungsten lamp decreases rapidly below 400 nm. Therefore, these lamps cannot be employed in the UV range of the spectrum. In the region below 350 nm gas discharge lamps are used as radiation sources, of which the most important type is the hydrogen or deuterium lamp. The hydrogen discharge provides a continuous spectrum between 160 and 400 nm.

2.3 FTIR Spectroscopy

Fourier transform infrared spectra of the samples were measured using a Bio-Rad Digilab FTS 40 FTIR spectrometer. The light source of this device is a globar which emits a continuous black-body spectrum in the infrared and is cooled by an external chiller. This spectrometer requires a constant supply of dry air to keep the KBr optics in proper working conditions.

2.3.1 FTIR Absorption

The FTIR technique derives from the classical Michelson interferometer. A parallel beam of radiation is directed from the source to the interferometer, which consists of two mutually perpendicular mirrors, one of which is stationary while the other one moves at a constant velocity, and a beam splitter mounted at 45° with respect to the mirrors (see Fig. 2.6). The beam splitter reflects 50 per cent of the incoming radiation. Thus half of the radiation goes to the stationary mirror, and the other half to the movable mirror, then it returns form both mirrors along the same paths. The light is recombined to a single beam at the beam splitter.

When monochromatic light is irradiated into the Michelson interferometer, the recombined beam leaving the beam splitter shows constructive or destructive interference depending on the relative path lengths from the beam splitter to the mirrors and back. If the path lengths are identical or differ by an integer number of half wavelengths, constructive interference takes place, whereas if the difference is a half-integer number of half wavelengths, the interference is destructive. Since the motion of the mirror is smooth, the detector sees a signal alternating in intensity according to a $\cos^2$ function of the mirror position. When the source emits two separate monochromatic frequencies ν_1 and ν_2, the recorded interference pattern is the sum of the signals corresponding to the individual frequencies. It can be shown that the spectral intensity distribution of the light source is recovered by (numerical) Fourier back-transformation of the interferogram (i.e., the recorded signal as a function of the mirror position). Also polychromatic light produces an interference pattern which can be transformed back to the original frequency distribution.

The recording of a FTIR spectrum is a two-stage process. First, without the sample in the beam, the movable mirror is scanned smoothly over a distance of about 1 cm, while the the interferogram is recorded by the detector. The computer then calculates

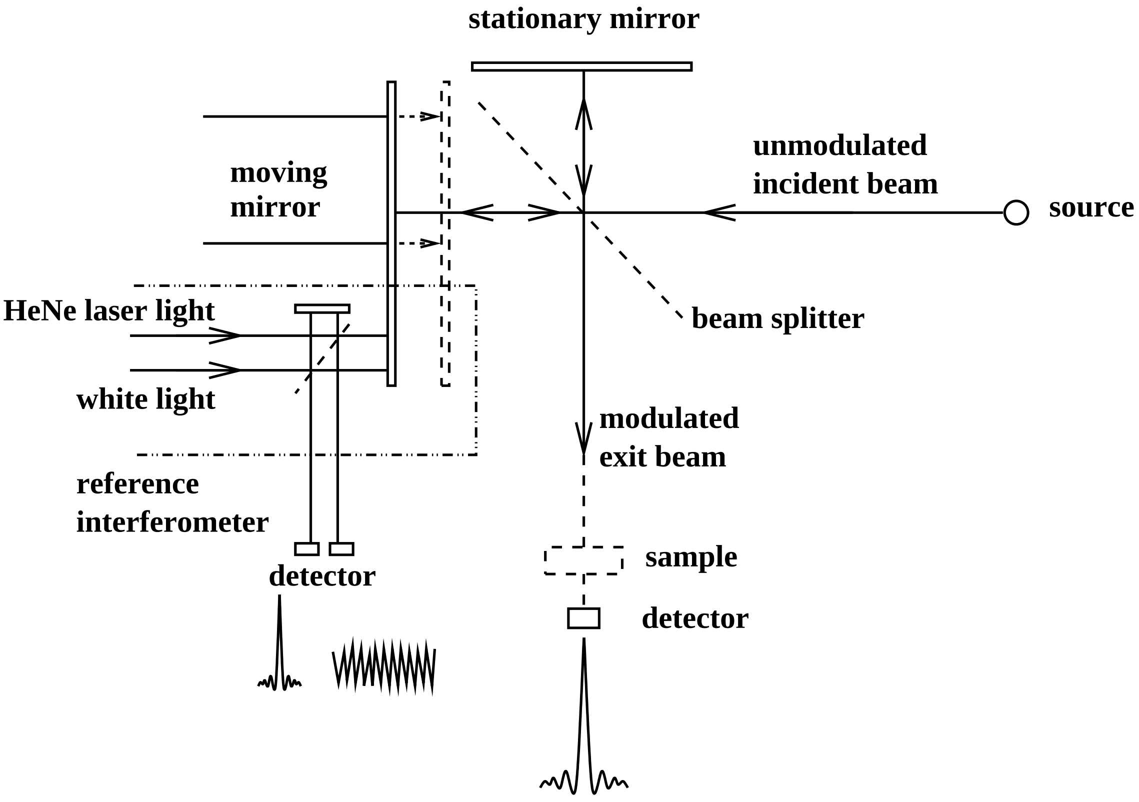

FIG. 2.6. Optical scheme of a Michelson interferometer commonly used in FTIR instruments.

the Fourier transform of the stored data to obtain the background spectrum. Secondly, a sample interferogram is recorded in exactly the same way, Fourier transformed, and after subtracting the background, the absorbance or transmittance spectrum of the sample results.

The FTIR spectrometer uses a laser (see Fig. 2.6) to control the velocity of the movable mirror and the collection of data points throughout the mirror scan. This laser is also used for wavelength calibration.

Comparison of FTIR with dispersive methods

In Section 2.1 dispersive instruments such as grating scanning spectrometers have been described. In a conventional dispersive IR spectrometer the polychromatic radiation of the source is dispersed by a monochromator, and detected in small wavenumber increments $\Delta\tilde{\nu}$ as determined by the grating and the slit width.

In the FTIR technique, $I(\tilde{\nu})$ is given by the phase difference ϕ. Modern IR spectrometers consist of FTIR interferometers, since this technique provides several differences and advantages as compared to dispersive devices. First, a FTIR instrument does not separate the energy into individual frequency elements for the measurement of a

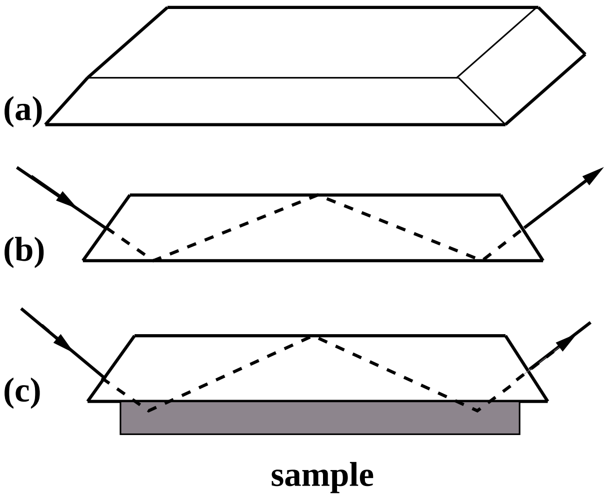

FIG. 2.7. Experimental arrangement for attenuated total reflection spectroscopy: **(a)** crystal block, **(b)** internal reflection in the block, **(c)** penetration of the evanescent wave into the sample pressed against the block.

spectrum. Each point of the interferogram contains information from each wavelength interval.

Another difference is that in FTIR spectrometry, no slit is used to limit the individual frequency intervals reaching the sample and the detector as in the case of dispersive instruments.

The resolving power of a FTIR is constant over the entire spectrum, whereas in a grating spectrometer it depends on the angle under which the grating is illuminated and, hence varies with the optical frequency.

2.3.2 ATR-FTIR

Although absorption methods are by far the most common way to measure infrared spectra, for collecting spectral information from surfaces, where transmission spectroscopy does not work, *attenuated total reflection* (ATR) spectroscopy is used. The ATR-FTIR spectra presented in this thesis have been measured using an ATR accessory with a trapezoidal KRS-5 crystal (a mixed thallium halide) plugged directly into the previously described Bio-Rad FTIR spectrometer.

The sample, which may be solid or a solution, is in contact with the trapezoidal crystal surface. The crystal block must be made from a transparent material of high refractive index. Since the infrared data are collected from the reflected and not the transmitted light, also opaque samples can be investigated. Intensities can be enhanced by using multiple internal reflections in a trapezoidal crystal as shown in Fig. 2.7

The principle of this spectroscopical technique can be summarized as follows. The interface between two different media, characterized by the refractive indeces n_1 and

n_2, $n_1 > n_2$, is considered. A light beam is going from the dense medium 1 to the less dense medium 2. For this system the *refraction law* can be written

$$n_1 \sin\theta_i = n_2 \sin\theta_r, \tag{2.4}$$

where θ_i and θ_r are the angle of incidence and the refraction angle, respectively, both defined with respect to the surface normal. For a critical value of the incoming angle, $\theta_r = 90°$, $\sin\theta_i = n_2/n_1$. For this angle of incidence and beyond, all light is reflected back into medium 1. This process is known as *total internal reflection.*

In order to understand the phenomenon of attenuated total reflection, the refractive index of medium 2 must be written in a more general form,

$$\mu = n + ik. \tag{2.5}$$

The real part n is the regular refractive index, and the imaginary part corresponds to the absorption, where k is the so-called *extinction coefficient.* This extinction coefficient is related with the absorption coefficient in the Bouger-Lambert-Beer law (see Eq. 1.26 and 1.30) as follows:

$$\alpha'(\omega) = \frac{4\pi\tilde{\nu}}{X}k, \tag{2.6}$$

where X is the molar concentration and $\tilde{\nu}$ the wavenumber of the light. Hence, in the neighborhood of an absorption line of medium 2, the complex refractive index as given by Eq. 2.5 has to be used. Thus, a light beam will experience regular total reflection at the surface if the wavelength of the light does not correspond to any transition wavelength of the medium 2. However if the wavelength does correspond to a transition, the reflected beam will be *attenuated*, hence the name ATR.

2.4 Raman Spectroscopy

2.4.1 Confocal Microscopy

The essential features of a confocal microscope are shown in Fig. 2.8. The illuminating light beam (usually a laser beam) is focused to a tiny — in the ideal case diffraction-limited — spot on the sample with a lens or microscope objective (L1). The reflected or backscattered light is collected and recollimated by the same lens or objective. The collected light is separated from the incoming beam by a beam splitter, and is then focused through a pinhole onto the detector by a second lens or microscope objective (L2). Light originating from a part of the sample which is not located in the focal plane of L1, but closer or farther away, is blocked by the pinhole and does not reach the detector. As a result, this light will not distort the signal. This feature provides the most important difference of the confocal configuration with respect to conventional microscopy. In conventional microscopy those planes of the sample which are out

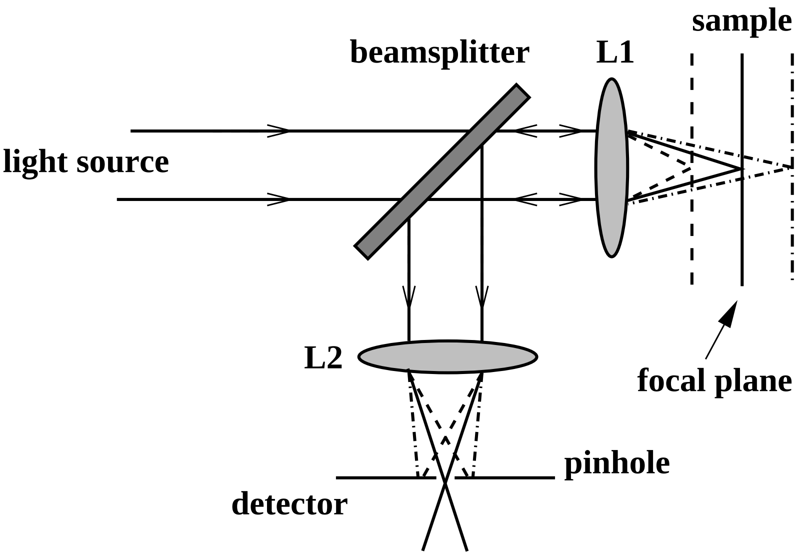

FIG. 2.8. The confocal principle. L1 and L2 are two lenses or microscope objectives.

of focus appear blurred in the image, whereas with a confocal setup, they do not contribute any signal and are dark.

Another important difference is that in a conventional microscope a certain field of view is illuminated and observed at the same time (wide-field imaging), whereas in a confocal microscope only single points are illuminated, and recording an image of the object requires raster scanning. On the other hand, also three-dimensional scans can be performed by combining two-dimensional image planes with a Z-scan of the sample. These raster scans can easily be performed mounting the sample on a piezo translator stage. This technique provides a significant improvement of both contrast and spatial resolution.

The resolution of a lens or an objective is described by its point-spread function (PSF). If the element has diffraction-limited performance, the PSF is given by the Airy function. In the plane, the *lateral resolution* can be obtained using a Rayleigh-like criterion; thus the minimum lateral distance between two points to be resolved, Δx or Δy, is given by the following expression

$$\Delta x = \Delta y = \frac{0.56\lambda}{NA}, \tag{2.7}$$

where λ is the light wavelength and NA the numerical aperture of the lens or objective. The latter is defined as

$$NA = n \sin\theta, \tag{2.8}$$

where n is the refractive index of the surrounding medium (e.g. air or oil) and θ the half angle of the maximum cone of light collected by the lens.

In the direction of the light beam (Z-direction), the *axial resolution* Δz corresponds to [38]

$$\Delta z = \frac{0.89\lambda}{(NA)^2}. \tag{2.9}$$

The pinhole diameter can also influence this resolution. If it is too large, the resolution — in particular in Z direction — will be worse than given by the above expressions.

2.4.2 Setup for Raman Spectroscopy

For the Raman measurements a custom-built confocal setup has been used. It was basically built by M. Bauer [39] and T. Schittkowsky [38] in two diploma theses, and was later refined as described in Ref. [40]. The setup combines the three-dimensional spatial resolution of a confocal microscope with the vibrational sensitivity of Raman spectroscopy. Hence, two- and three-dimensional images of the chemical composition of complex materials and mixtures of materials can be recorded. Further modifications of the original setup have been performed during this thesis, such as the inclusion of an inverted microscope. These modifications have been described in the publications [41, 42].

A schematic picture of the apparatus used in the present work is shown in Fig. 2.9. A laser beam is focused onto the sample by a microscope objective, the backscattered

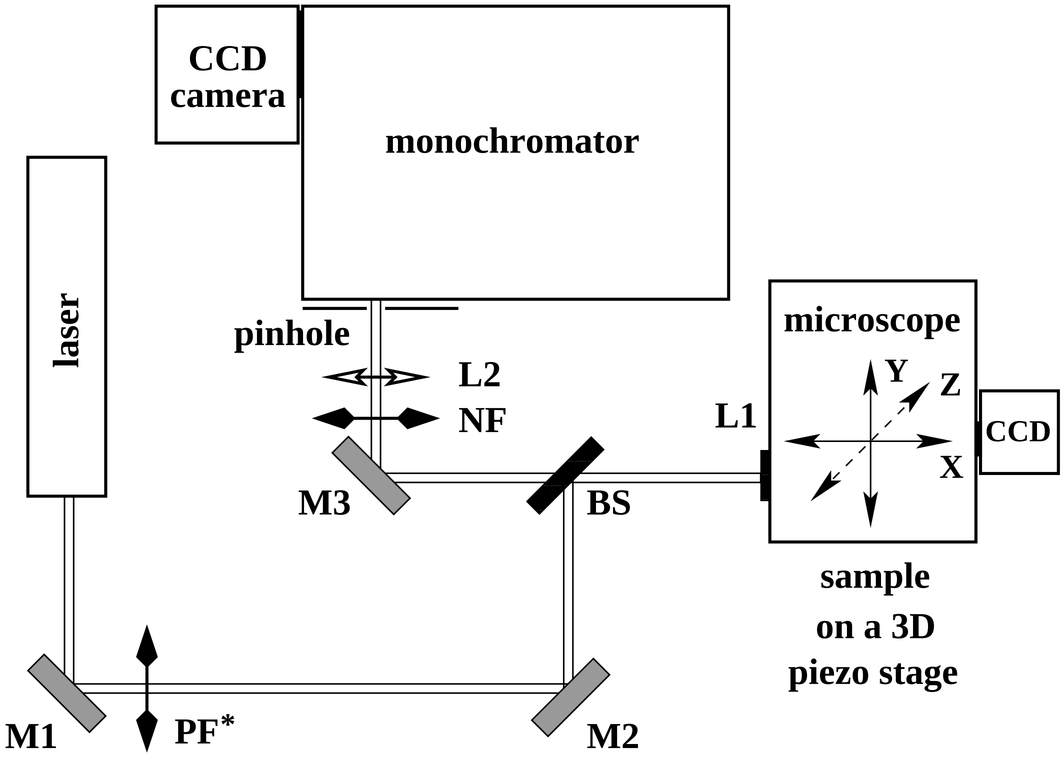

FIG. 2.9. Custom-built confocal Raman microscope. The details of the setup are explained in the text. ∗ Only required in the case of a HeNe laser as excitation source.

light is collected by the same objective and then focused through a pinhole into a monochromator. Finally, the dispersed light signal is recorded with a CCD detector.

Laser

As light source, in most of the experiments an unpolarized HeNe laser of 632.8 nm wavelength and 16 mW power manufactured by *Melles Griot* has been used. For another set of measurements, the source was a linearly polarized frequency-doubled cw Nd:YAG laser of 532 nm wavelength (*ADLAS325*) with a power of 30 mW. The intensity of the lasers was reduced with OD filters to an effective power of a few milliwatts on the samples. The working principle of both lasers has been explained in the previous section. In the case of the HeNe laser, a group of narrow fluorescence lines are emitted by the plasma tube and can contaminate the signal. These so-called *plasma lines* are suppressed with an interference filter (PF), which permits high transmission at 633 nm, and blocks most of the other spectral regions. The transmission width is about 10 nm. This interval can be slightly shifted to longer or shorter wavelengths by varying the angle between the filter and the incoming ray, which is around 90°. In the present setup, the angle is adjusted such that all residual plasma line transmissions are in the anti-Stokes side of the spectra. The filter was purchased from AHF Analysentechnik.

Beam splitter

The excitation beam is reflected by a beam splitter (BS) into a side port of the microscope (schematically depicted as L1). Two different beam splitter types have been used: a 50:50 nonpolarizing cube beam splitter and an interference filter at 45°. The *cube beam splitter* divides the incident beam of intensity I_0 into two beams of intensity $I_0/2$. Since confocal configuration is used, the backscattered light of intensity I_r passes again through the same beam splitter and is split into two components of $I_r/2$ (see Fig. 2.9). Hence, half of the laser power and the half of the collected scattered light are lost. If the laser power is sufficiently high, the first loss is irrelevant. If the scattered light signal is sufficient, the second loss is not very important either. But in cases in which the sample yields only weak Raman signals or cannot tolerate high laser intensities, so that the laser power has to be strongly attenuated for the measurements, this type of beam splitter is not the optimal choice.

An alternative in the latter cases is to use an *interference filter* at 45° (AHF Analysentechnik). This class of filters are designed so as to be highly reflective for a certain range of wavelengths, which has to be chosen such that the laser wavelength is close to its upper edge. At longer wavelengths, the filter has high transmission. Thus, the laser beam is reflected into the microscope (see Fig. 2.9) and the scattered light in the Stokes region is transmitted. With this dichroic beam splitter the signal loss is negligible, the plasma line filter can usually be omitted, and the Rayleigh line is strongly suppressed

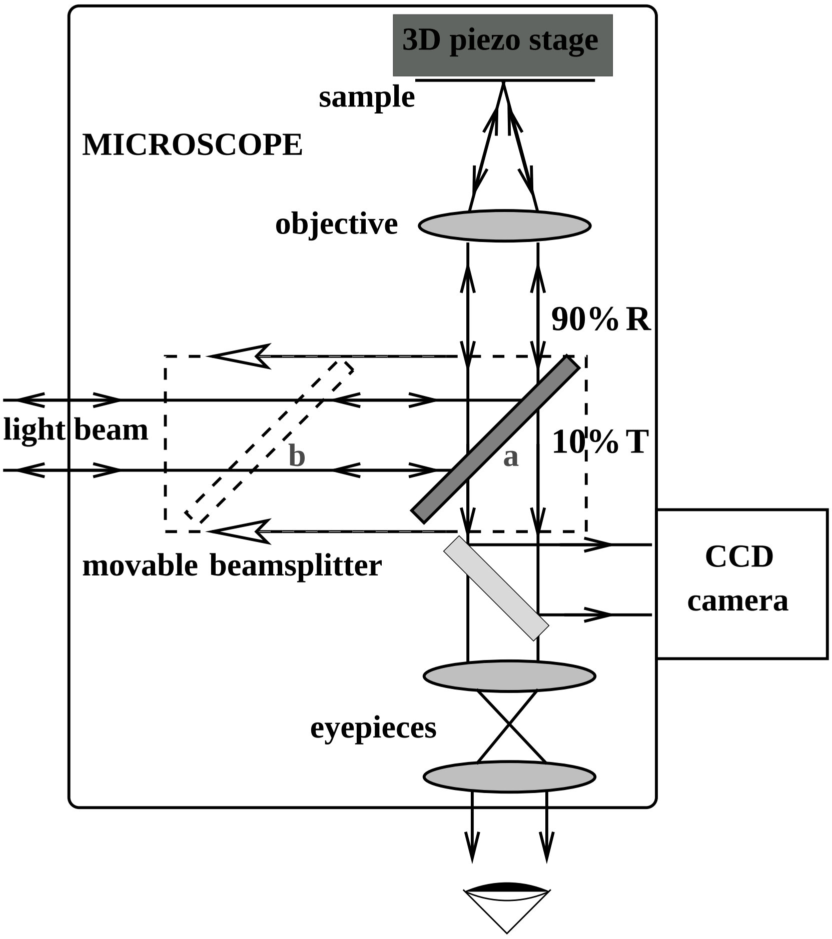

FIG. 2.10. Microscope and light path.

preventing damage of the camera. But it has also some disadvantages: The adjustment of the setup becomes much more complicated and, owing to the characteristics of these filters, the anti-Stokes region is also blocked and cannot be investigated.

Microscope

The task of the optical system L1 is to receive the light coming from the beam splitter, focus it onto the sample, collect the scattered light and redirect it again to the beam splitter. Originally, L1 was only a microscope objective but in the course of this thesis it was changed to an inverted microscope Swift M 100 with objectives of different magnifications and numerical apertures. Nikon PlanApo objectives 4× / 0.18, 10× / 0.45, 20× / 0.75, and a Leica PL Fluotar 100× / 0.75 are available. The sample holder is mounted on a three-dimensional piezo translator (TRITOR 102; Piezosystem Jena) whose maximum scan range is 100μm in each direction. The sample holder can accommodate solid samples, preferably on microscope slides, and quartz cuvettes for investigating liquids. In most cases the Raman spectra of solid samples were measured

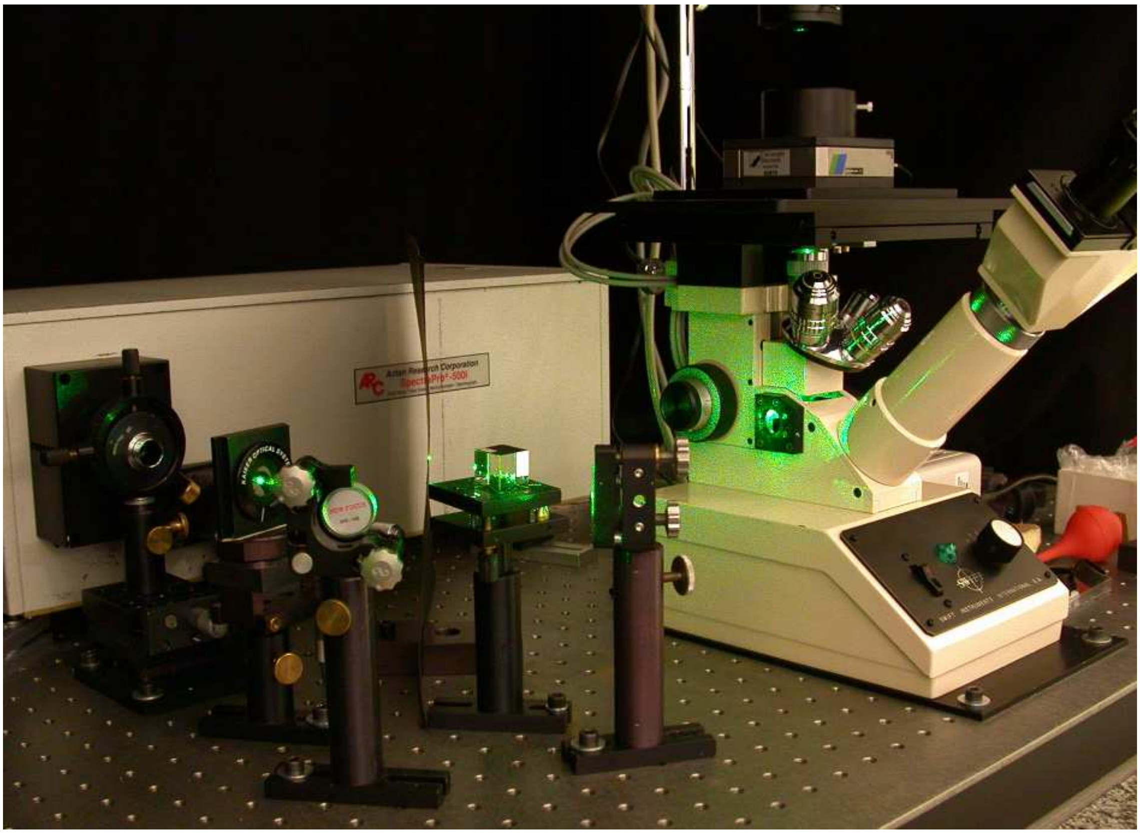

FIG. 2.11. Optical elements of the confocal setup including the monochromator and the inverted microscope.

with the 100× objective, whereas for solutions the 4× objective was used.

The microscope has been adapted in such a way that it can be used as a conventional microscope and as part of the confocal Raman microscope. It carries a movable beam splitter inside its body. When the beam splitter is in the *b* position, (see Fig. 2.10) the microscope acts as a conventional inverted microscope, in which the image of the sample can be observed directly with eyepieces, or by means of a small B/W CCD camera (Sanyo). When the beam splitter is shifted to *a*, the laser light coming from the external BS is reflected into the objective and focused onto the sample (see Fig. 2.10). The backscattered light is collimated by the same objective, and after being reflected by the microscope beam splitter, it leaves the microscope body. The movable beam splitter is highly reflective (∼ 90%); the transmitted fraction of the light (10%) allows for simultaneous observation of the sample during the measurements.

Notch filter

Fig. 2.9 shows that the scattered light, after leaving L1, passes through the external beam splitter and it is reflected through the notch filter (NF) by mirror M3. The holographic notch filter (Kaiser Optical Systems) suppresses the Rayleigh line by a factor of about 10^6. The inelastically scattered light and the residual light of the Rayleigh line are then focused into the monochromator by L2. L2 can be an achromat lens or a microscope objective of low magnification. Its NA must be adapted to the f-number of the monochromator. Similar to the plasma line filter, the blocking region of the notch filter can be slightly shifted by adjusting its orientation. The optics between the inverted microscope and the monochromator is shown in Fig. 2.11.

Pinhole and Monochromator

As mentioned previously, the entrance slit of the monochromator was replaced with a 50 μm pinhole (in some cases also a 80 μm pinhole) for confocal depth selection. Spectral dispersion is performed in a single monochromator (Acton Research Spectra-Pro-500i) with a grating of 300 grooves per mm, yielding a resolution of 2.6 cm^{-1} for the red excitation, and of 3.7 cm^{-1} for the green light. As was previously discussed, the resolution of grating spectrometers depends on the frequency range under investigation. The monochromator is mounted in an astigmatism-compensated Czerny-Turner configuration (see section 2.1, and Fig. 2.4), in which the exit slit is replaced by the CCD camera chip. A spectral window of $\sim$3500 cm^{-1} can be recorded simultaneously with the red laser, and of $\sim$5000 cm^{-1} with the green one.

CCD Camera

Raman spectra are recorded with a front-illuminated liquid-nitrogen-cooled CCD (Charge-Coupled Device) detector with 1340 × 100 pixels and an area of 27 mm × 2 mm (Princeton Instruments). Its operating temperature is in the range $-80°$ to $-120°$. The quantum efficiency is $\sim$ 40% between 600 and 800 nm and $\sim$ 25% at 532 nm.

Although the monochromator is astigmatism-compensated and produces an image height of only 2-3 pixels in the center of the chip, the image height increases strongly towards the edges. Therefore, complete vertical binning of the CCD chip (100 pixels) is used. This does not deteriorate the signal-to-noise ratio significantly, since the (dark) noise is determined by readout noise of the chip.

The spectra presented in this thesis are the sum of several spectral accumulations, each with 1 s integration time. Typical total acquisition times ranged between 15 s and 5 min. All experiments were performed at room temperature.

Chapter 3

Characterization of the Samples

3.1 Dyes for Organic Solar Cells

Ruthenium(II) complexes containing polypyridyl ligands have been widely studied as potential photosensitizers in solar cells [1–4]. Of particular interest is their use in dye-sensitized solar cells based on nanocrystalline films of TiO_2. The light is absorbed by the dye, then the photoexcited dye molecule transfers an electron to the conduction band of the semiconductor (TiO_2). The injected electrons percolate in the nanocrystalline TiO_2 to the anode. The oxidized form of the dye is rapidly reduced by redox mediators. Metal-to-ligand charge-transfer transitions dominate the visible absorption spectra of the dyes as well as the main features of their photophysical and redox behavior. Functional groups of the dye allow for efficient anchoring on the semiconductor surface and promote the electronic communication between the donor orbital of the dye and the conduction band of the semiconductor.

In this thesis, we mainly worked with two dyes which have ligands of different nature: the well-known $(Bu_4N)_2[Ru(dcbpyH)_2(NCS)_2]$ photosensitizer with cyano ligands and a new dye, $[Ru(dcbpyH_2)_2(bpy\text{-}TPA_2)](PF_6)_2$, with triphenylamine (TPA) moieties. The TPA unit is often used in organic solid-state dye-sensitized solar cells as a hole conductor [43–46]. Hence, this moiety was attached to the Ru complex as a ligand in order to improve the charge transfer to the hole transport layer. A more detailed discussion of the influence of this interface modification in solar cells can be found in Refs. [43] and [47].

The dye N719, cis-bis(isothiocyanato)-bis-(2,2'-bipyridyl-4,4'-dicarboxylato) ruthenium(II)-bis(tetrabutylammonium), or $(Bu_4N)_2[Ru(dcbpyH)_2(NCS)_2]$, Bu_4N = tetrabutylammonium and dcbpy = dicarboxybipyridine, (see Fig. 3.1), was purchased from Solaronix S.A. (Lausanne, Switzerland) and used as received. The dye Ru-TPA_2, bis-(2,2'-bipyridyl-4,4'-dicarboxylic acid)-2,2'-bipyridyl-4,4'-bis(vinyltriphenylamino) ruthenium(II) hexafluorophosphate, or $[Ru(dcbpyH_2)_2(bpy\text{-}TPA_2)](PF_6)_2$, bpy = bipyridine

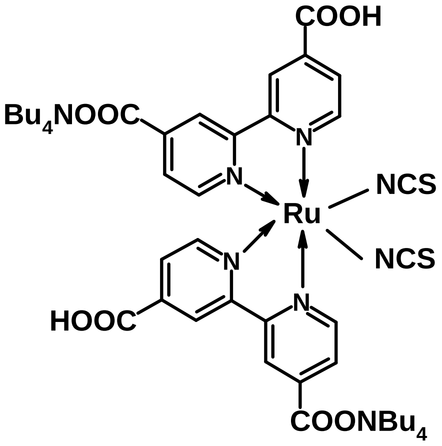

FIG. 3.1. Chemical structure of $(Bu_4N)_2[Ru(dcbpyH)_2(NCS)_2]$ (N719).

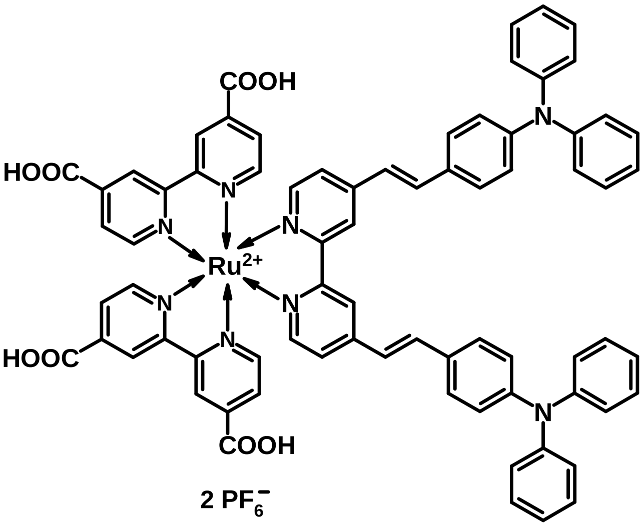

FIG. 3.2. Chemical structure of $[Ru(dcbpyH_2)_2(bpy\text{-}TPA_2)](PF_6)_2$ (Ru-TPA_2).

and TPA = triphenylamine, (see Fig. 3.2), was synthesized by K. Peter and M. Thelakkat as described in [47,48].

The aim of this chapter is to characterize the samples using different spectroscopical techniques: UV-VIS, Raman, and FTIR spectroscopy. The influence of the solvent on the UV-VIS spectrum, the effect of the laser wavelength on the Raman spectra, and the assignment of the absorption and vibrational bands will be discussed. This description of the dyes can be used as a reference for the rest of the chapters throughout this thesis. To provide further spectral information for the characterization of the complexes, also the UV-VIS, Raman, and FTIR spectra of tetra-n-butylammonium iodide, triphenylamine (TPA), and of the bpy-TPA_2 ligand were measured.

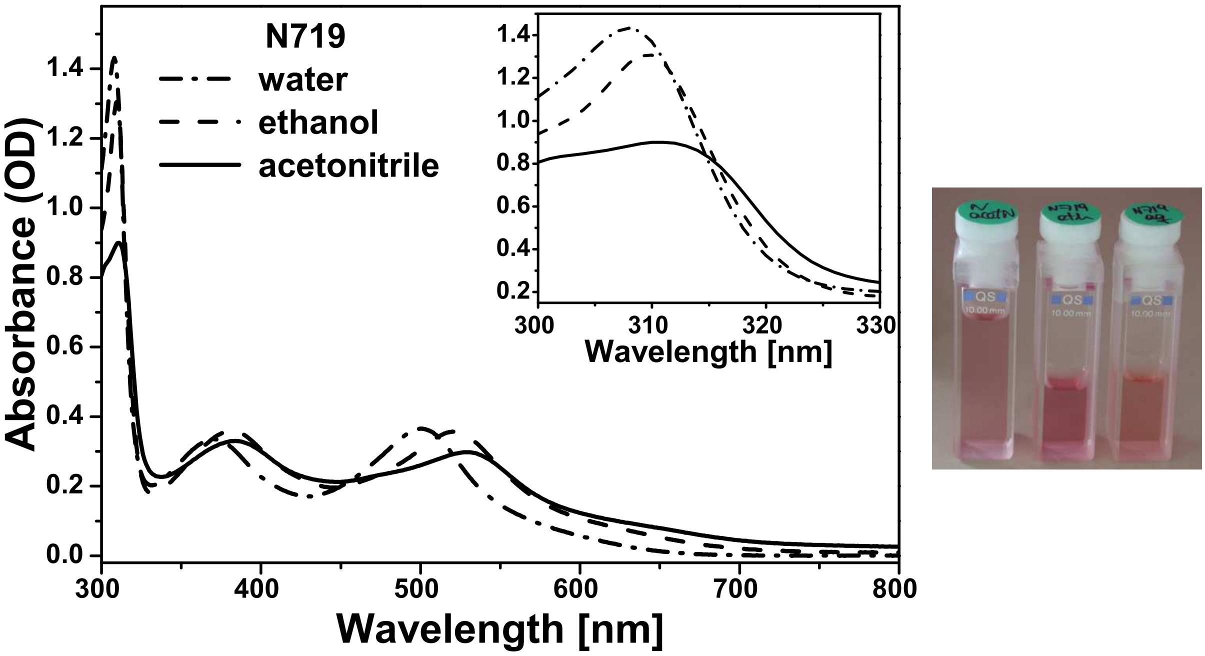

FIG. 3.3. Absorption spectra of N719 in different solvents. The inset shows the intraligand charge-transfer bands on an enlarged wavelength scale. The photograph on the right side shows the three solutions.

3.1.1 UV-VIS: Solvatochromism

UV-VIS absorption spectroscopy was performed with a Perkin-Elmer UV/VIS/NIR spectrophotometer. Scan rates were 240 nm/min. The spectral resolution was 2 nm over the spectral region of interest. The concentration of the dyes in the solvents was less than 3.5×10^{-5} M. The experiments were carried out in quartz cuvettes with 1 cm thickness. The absorption spectra of the investigated dyes in different solvents (doubly distilled water, ethanol, and acetonitrile) are shown in Fig. 3.3 and 3.4. The weaker absorption of the complex Ru-TPA$_2$ in water is a consequence of its poor solubility in this solvent.

In the visible region, the spectra of Ru(II) complexes containing polypyridyl ligands are dominated by bands arising from metal-to-ligand charge-transfer (MLCT) transitions, in which an electron is promoted from a ruthenium dπ orbital to the π system of the polypyridyl ligand. The bands in the UV are due to intraligand transitions ($\pi \rightarrow \pi^*$). The wavelength of the absorption maxima are listed in Table 3.1. The bpy-TPA$_2$ ligand of the Ru-TPA$_2$ complex exhibits a strong absorption band at ~392 nm when dissolved in ethanol and at 388 nm in acetonitrile. Most probably the bands which appear at ~395 nm in the UV-VIS spectra of the complete Ru-TPA$_2$ dye correspond to MLCT. However, a contribution of the ILCT transition of the bpy-TPA$_2$ ligand to these absorptions is not unlikely.

The energies and, in the case of Ru-TPA$_2$, also the shapes of the MLCT bands are

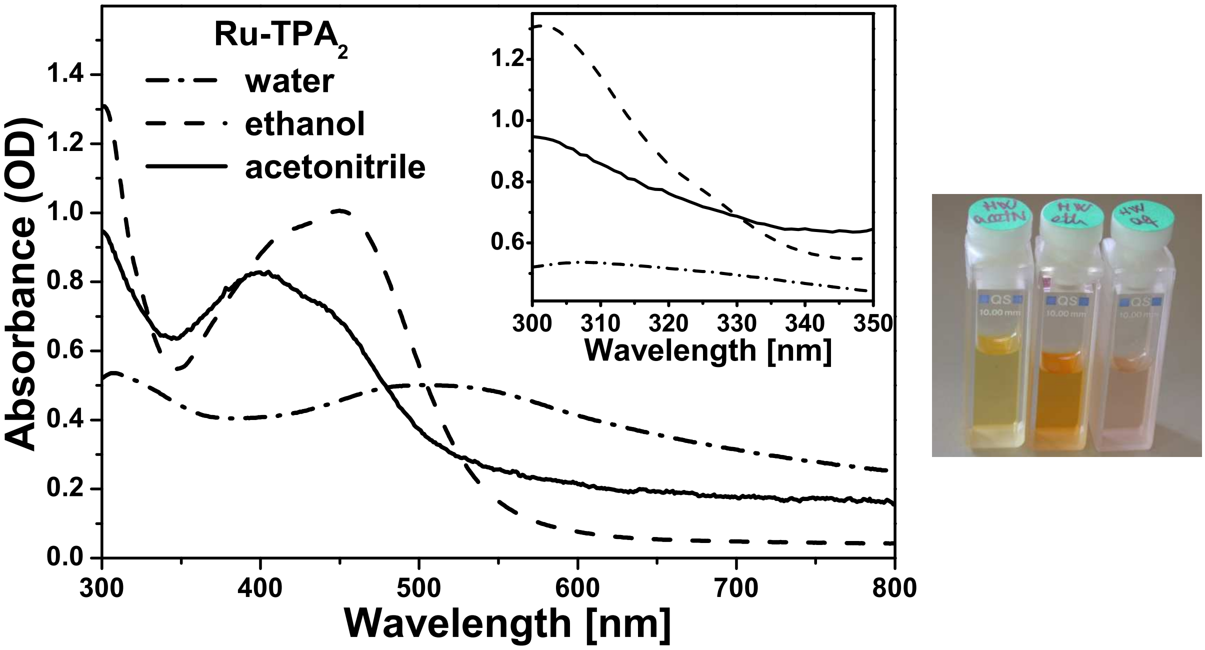

FIG. 3.4. Absorption spectra of Ru-TPA$_2$ in different solvents. The inset shows the intraligand charge-transfer bands on an enlarged wavelength scale. The photograph on the right side shows the three solutions.

strongly solvent-dependent, whereas the shifts of the intraligand bands are less pronounced. The solvent dependence of the wavelength of electronic transitions (solvatochromism) has been extensively studied in the literature [4, 49–54]. The solvatochromic shifts can be large for charge-transfer bands, as was discussed in detail in a review article by Chen and Meyer [53]. If the solvent can be approximated by a dielectric continuum, it is possible to calculate its contributions to these shifts from the known geometry of the solute and the dielectric properties of the solvent. But the dielectric continuum theory breaks down for charge transfer in amine or cyano complexes, because there are specific interactions between these ligands and the individual solvent molecules. These interactions exist in addition to the continuum effects and tend to dominate; hence, correlations with dielectric functions normally fail. Specific interactions arise from H-bonding or donor-acceptor interactions. In both cases, orbital mixing occurs between individual ligands and solvent molecules. Given the nature of the specific interactions, the donor number (DN) and acceptor number (AN) introduced by Gutmann are useful parameters for correlating MLCT solvent shifts. The Gutmann donor and acceptor number are dimensionless quantities which provide a relative measure of the Lewis acidity (electron pair acceptor ability) of the solvent [55].

The N719 transitions perform a blue shift with increasing Gutmann acceptor number. This effect can be due to the H-bonding of solvent molecules to the electron pair of the thiocyanate sulfur, as previously noted for other cyano and thiocyano complexes [4, 53, 56]. The blue shift increases with the number of CN ligands [53]. For water,

TABLE 3.1. Absorption of N719 and Ru-TPA$_2$ in different organic solvents at room temperature.

	absorption maxima [nm]		
complex / solvent	Intraligand CT	MLCT	
N719 / H_2O	308	370	500
N719 / C_2H_5OH	309	381	521
N719 / CH_3CN	311	383	529
Ru-TPA$_2$ / H_2O [a]	307	—	507
Ru-TPA$_2$ / C_2H_5OH [a]	299	396[b]	461
Ru-TPA$_2$ / CH_3CN [a]	294	394[b]	451

[a] Calculated with a Lorentzian Fit.

[b] ILCT transitions can also contribute to these absorption bands.

AN = 54.8; for ethanol, AN = 37.1; and for acetonitrile, AN = 19.3 [55]. Amine complex transitions, on the other hand, usually exhibit a red shift of the absorption band energies with increasing Gutmann donor number of the solvent. This correlation has been ascribed to H-bonding of the solvent with the amine groups [53, 54]. As in the case of cyano complexes, the correlation increases with the number of amine ligands [53]. In the Ru-TPA$_2$ solutions, water seems to act as if it had a higher donor number, causing a larger shift than ethanol. For water, DN = 18.0; for ethanol, DN = 20.0; and for acetonitrile, DN = 14.1 [55]. Another contribution which must be taken into account is the different protonation state of the carboxylic groups of the dyes in the different solutions, owing to the varying Lewis acidity of the solvents. The deprotonation of these moieties in the N719 complex produces shifts of the MLCT bands toward the UV region, as was observed in Ref. [4, 57]. The authors ascribed these shifts to the increase of the LUMO energy of the ligand causing the intraligand and MLCT transitions to shift to shorter wavelengths.

3.1.2 Raman Investigations

For measuring the Raman spectra we used a custom-built confocal setup described in chapter 2. It is centered around an inverted microscope Swift M 100. PlanApo objectives of different magnifications and numerical aperture values were used for focusing the laser and collecting the scattered light. The setup is equipped with an unpolarized HeNe laser ($\lambda = 632.8$ nm) and a linearly polarized frequency-doubled cw Nd:YAG laser ($\lambda = 532$ nm), both providing an effective power of a few milliwatts on the sample. In some of the measurements this power was reduced to avoid light-induced modifications of the dyes (see appendix A). Spectral dispersion is performed in a single monochromator (Acton Research SpectraPro-500i) with a grating of 300 grooves per mm, yielding a resolution of 2.6 cm^{-1} for the red excitation, and of 3.7 cm^{-1} for the green light.

The Rayleigh line is suppressed by a factor of about 10^6 with a holographic notch filter (Kaiser Optical Systems). Raman spectra are recorded with a liquid-nitrogen-cooled CCD detector with 1340 × 100 pixels (Princeton Instruments).

Raman spectra of the complexes were measured in a pristine powder state to avoid solvent effects and overlapping of their vibrational lines with the lines of the solvents. To this end, the complexes were pressed to pellets with KBr so they could be easily mounted in the sample holder. The sample holder was fixed to a three-dimensional piezo translator (TRITOR 102; Piezosystem Jena), which moved the pellet every second in the plane perpendicular to the irradiation path to avoid overheating and other laser-induced effects due to long exposure of the dyes to the beam. The spectra presented are the sum of several spectral accumulations, each with 1 s integration time, resulting in a total recording time of a few minutes. All experiments were performed at room temperature.

The absorption spectra of the dyes (Figures 3.3 and 3.4) show that at an excitation wavelength of 632.8 nm no significant contribution of resonance effects is expected. Moreover, the low absorption in this region reduces the probability of photodecomposition and other light-induced phenomena. Unfortunately, the normal Raman spectrum of N719 powder could not be measured with the red laser, owing to strong fluorescence. With the green line, however, we could excite a resonance Raman spectrum, since the N719 complex has its lowest MLCT transition close to this wavelength. As mentioned in chapter 1, when the frequency of the exciting beam is close to one of the electronic transitions of the system, the Raman intensity will become large. The vibrational modes which involve motions of that part of the molecule where the electronic transition is localized will be mainly enhanced, thus providing information about the resonant electronic level. In our measurements, a broad luminescence band close to 750 nm was simultaneously excited, which made it impossible to distinguish any Raman line above 2200 cm^{-1}. This luminescence band was also observed by Shoute and Loppnow on the completely protonated complex ($[\text{Ru(dcbpyH}_2)_2(\text{NCS})_2]$), also named N3 [58].

The Raman spectrum of Ru-TPA$_2$ could be measured with both irradiation wavelengths, with a very strong fluorescence background being present in both cases. The background was subtracted using fitting procedures. Due to the fluorescence, Raman lines above 2000 cm^{-1} could not be observed. No resonance enhancement is expected either at 632.8 nm or at 532 nm, but for the green excitation line, preresonance effects are possible. These results will be discussed later.

In addition, the Raman spectra of tetra-n-butylammonium iodide salt (TBAI), triphenylamine (TPA), and of the bpy-TPA$_2$ ligand, were recorded in a pristine powder state.

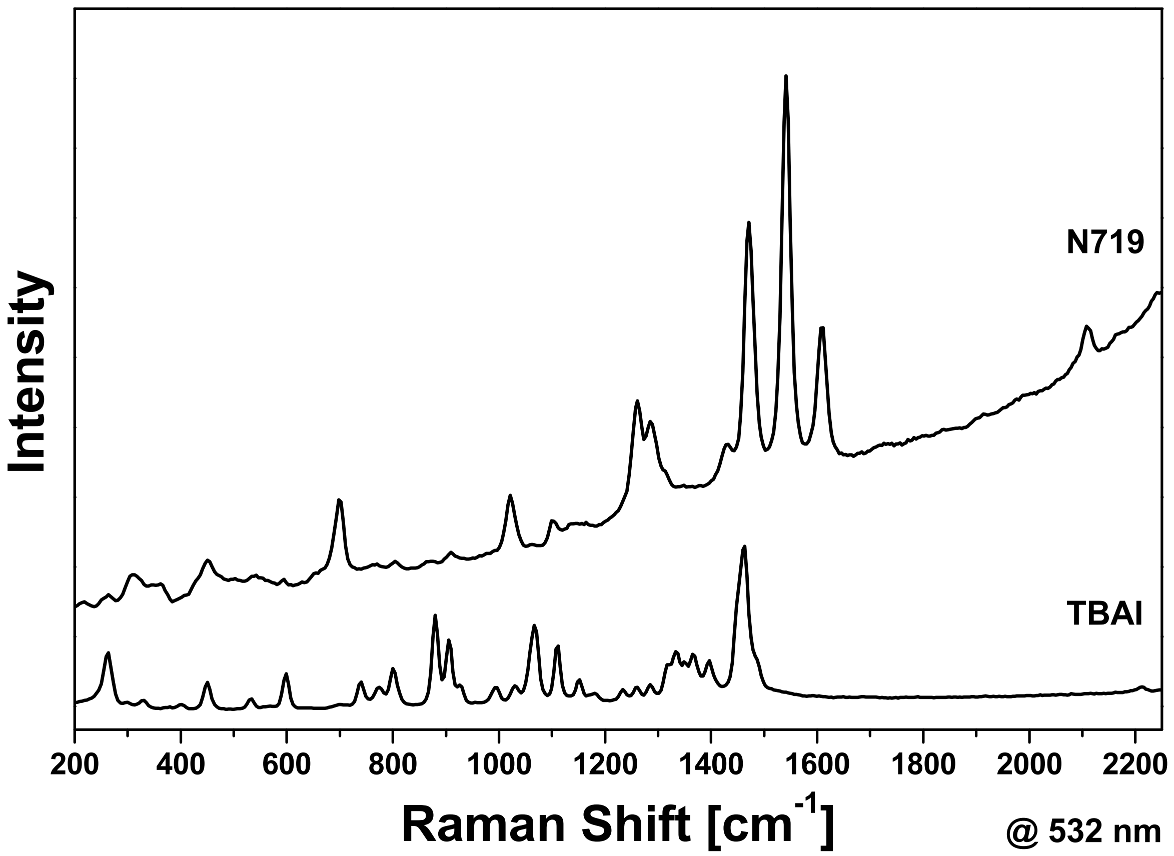

FIG. 3.5. Resonance Raman spectrum of N719, compared with TBAI.

N719

The resonance Raman spectrum (RRS) of the dye $(Bu_4N)_2[Ru(dcbpyH)_2(NCS)_2]$ and the normal spectrum of TBAI measured at 532 nm excitation wavelength are shown in Fig. 3.5. From the comparison of both signals we can conclude that there is no contribution of the vibrational lines of the tetrabutylammonium salt to the RRS of the complex. The spectrum is dominated by the bipyridine vibrations, whereas the lines corresponding to the thiocyanato ligand and to the carboxylic groups are very weak, almost not visible. The green laser excites the lower-energy MLCT band of the N719 molecule. Since the resonance Raman spectrum gives a direct fingerprint of the electronic transition, we can identify that the lowest-energy MLCT corresponds to the injection of an electron from the ruthenium atom to the acceptor ligands, the bipyridines.

The normal Raman and RRS of the N719 dye and similar complexes have already been described in the literature [2–4, 58–61]. Table 3.2 summarizes the results of this thesis. These data are compared with the nonresonant measurements performed by Finnie et al. at 1064 μm [59] and the RRS at 514 nm of Greijer et al. [3]. The resonance spectrum is characterized by the totally symmetric stretching vibrations of the bipyridine ligand

TABLE 3.2. Raman shift [cm^{-1}] and assignment of the bands observed in the powder of N719 and comparison with literature data.

N719 RRS @ 532 nm	N719^a (Ref. [3]) RRS @ 514 nm	N719 (Ref. [59]) @ 1064 μm	Vibrational Assignment
2108 (w)	2115 (w-m)	2100 (m)	ν(C=N) (SCN)
1726 (vw)	1729 (vw)	1723 (vw)	ν(C=O)
1610 (s)	1613 (s)	1609 (vs)	ν(C=C) (bpy)
1543 (vs)	1545 (vs)	1545 (m)	ν(C=C) (bpy)
1476 (s)	1470 (vs)	1470 (s)	ν(C=C) + ν(C=N) (bpy)
1430 (w)	—	—	ν(C=C) + ν(C=N) (bpy)
1313 (sh)	1302	1304 (w)	ν(C=C) intern-ring (bpy) + ν(C-O)
1287 (m-s)	1294	—	ν(C=C) intern-ring (bpy) + ν(C-O)
1263 (s)	1265	1266 (s)	ν(C=C) intern-ring (bpy) + ν(C-O)
1150 (vw)	—	—	i-p C-H wagging (bpy)
1105 (w)	1099	—	i-p C-H wagging (bpy)
1024 (m)	1024 (m)	—	ring breathing (bpy)
807 (vw)	812 (vw)	—	ν(C=S) (SCN)
701 (m)	704 (m)	—	i-p ring def (bpy)
454 (w)	—	—	o-o-p ring def (bpy)

v = very, s = strong, m =medium, w = weak, sh = shoulder, ν = stretching, bend = bending, def = deformation, i-p = in plane, o-o-p = out of plane

^{a} dye in ethanolic solution

at 1610, 1543, 1476, 1430, 1313, 1287 and 1263 cm^{-1} and the ring breathing and ring deformation at 1024 and 701 cm^{-1}, respectively. The lines corresponding to the carboxy groups are almost absent, because they are not directly involved in the charge-transfer transition. In the N719 complex, two carboxylic acids and two carboxylate groups are present. The acids have two nonequivalent oxygen atoms; the stretching (ν) vibrations of the C=O group appear usually at ~1700 cm^{-1}, whereas the ν(C-O) lines are between 1280 and 1315 cm^{-1}. In the deprotonated form, however, both oxygen atoms are considered equivalent and they exhibit both symmetric and antisymmetric bands. The $\nu_{asym}(\mathrm{COO}^-)$ is generally weak in the Raman spectrum and appears between 1550 and 1620 cm^{-1}, whereas the $\nu_{sym}(\mathrm{COO}^-)$ is strong and appears between 1360 and 1440 cm^{-1}.

The vibrational lines of the thiocyanate ligand are also not enhanced by the selective resonance effect, as was previously mentioned. For this reason, only a weak C=N stretching band of the NCS group at 2108 cm^{-1} can be observed; another very weak peak due to ν(C=S) is located at ~807 cm^{-1}.

Ru-TPA$_2$

To map the characteristic Raman lines and assign the vibrations of the different ligands of the [Ru(dcbpyH$_2$)$_2$(bpy-TPA$_2$)](PF$_6$)$_2$ dye, measurements were also performed on TPA and on the bpy-TPA$_2$ ligand. In Fig. 3.6 the spectra of the new dye Ru-TPA$_2$ are presented and compared with those of the ligands, obtained with the red and the green laser. It can be seen that the spectra of TPA are almost identical at both irradiation wavelengths, however no line of the bpy-TPA$_2$ ligand, of a intense yellow color, could be obtained with the green laser due to fluorescence. Only the relative intensity of some Raman lines seems to change with the variation of the wavelength for the Ru-TPA$_2$ complex. These changes will be discussed below.

A detailed list of the vibrational bands and their assignment is presented in Table 3.3. It is worth noticing that the lines of the donor ligand, bpy-TPA$_2$, dominate the spectrum. In addition, some lines of the bipyridines of weak or medium intensity are present, whereas no vibration of the carboxylic acids seemed to show up, although there are four protonated carboxy groups in the dye.

The spectra of triphenylamine (TPA) is composed of strong C=C stretching modes of the benzenes at 1605, and 1590 cm^{-1}, ring deformation bands (1000, 716 and 412 cm^{-1}), C-H bending, and C-H deformation lines (below 1350 cm^{-1}). Moreover, the weak to medium-intensity ν(C-N) of the linking nitrogen atom appear between 1315 and 1280 cm^{-1}.

In the signal of the bpy-TPA$_2$ ligand, the ring deformation lines of TPA decrease in intensity and the bands in the ν(C-N) and C-H bending region change their shape. New peaks of the C-H chain, in trans configuration (see Fig. 3.2), which attach the TPA to the bipyridine show up at ∼1630 cm^{-1} (ν(C=C)) and ∼1330 cm^{-1} (C-H def). Also some vibrations due to the bipyridine seem to be present.

The spectra of the complete dye is similar to that of the bpy-TPA$_2$ ligand, but some changes occur. The ν(C=C) of the conjugated alkene is weaker, new lines corresponding to bipyridine appear or increase in intensity at 1537, 1490 and 1024 cm^{-1} and, in the range 1250-1350 cm^{-1}, the shape of the lines changes again. Comparing the spectra of the complex measured with the red and the green laser, it turns out, firstly, that for the green excitation, the signal amplitude is slightly higher. Secondly, it can be noticed that the lines of bipyridine at 1537 and 1490 cm^{-1} are stronger when excited at 532 nm. The latter observation can be related to a preresonance effect in the complex, which could imply that the lower MLCT band corresponds to electron injection into a bipyridine unit. This is expectable since three bipyridines surround the ruthenium atom. As was mentioned in the introduction, the resonance effect appears gradually rather than abruptly, when approaching the absorption maximum, so we cannot exclude some influence of this effect on the spectra.

It was already mentioned that no lines of the protonated carboxylic acids could be

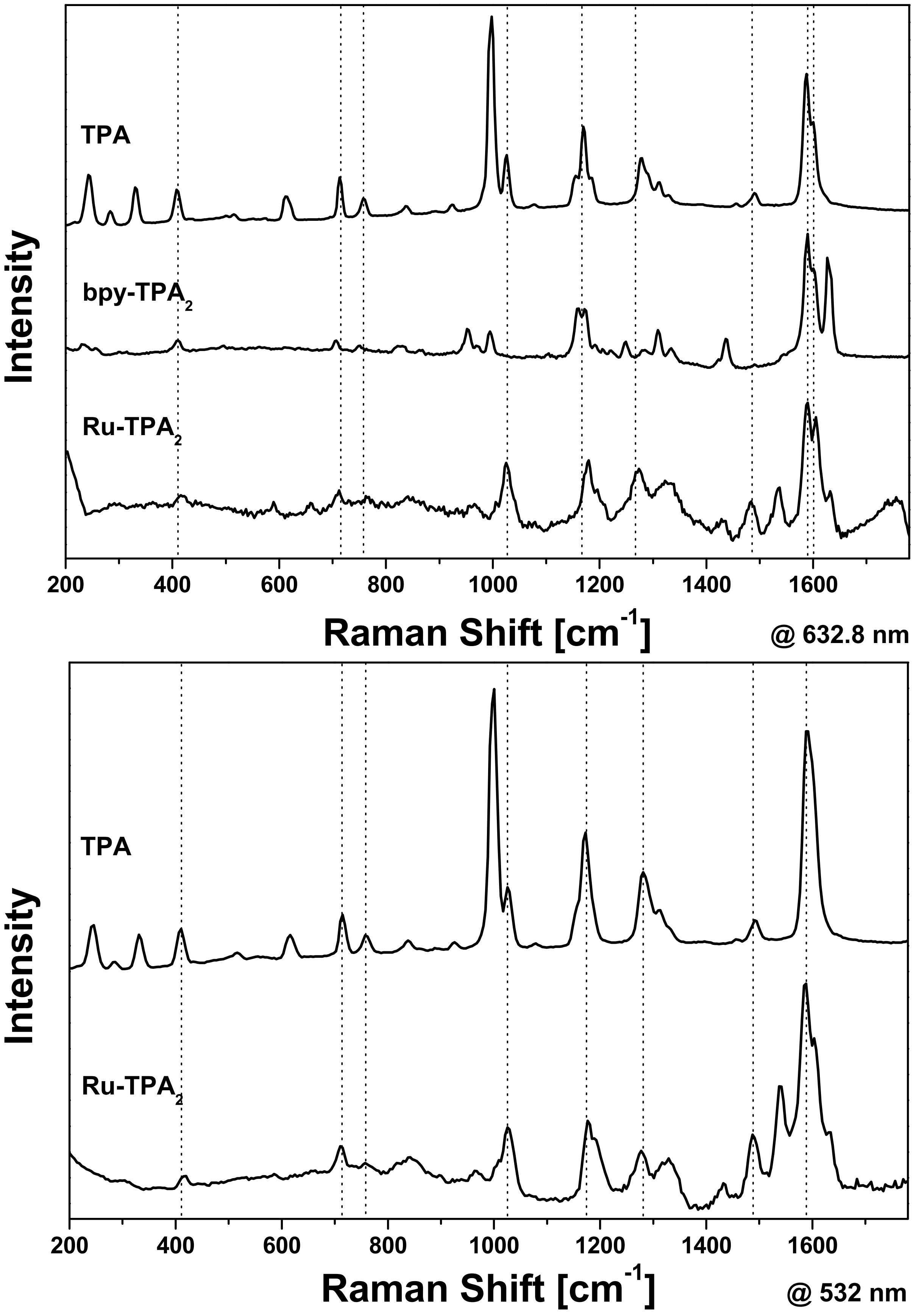

FIG. 3.6. Raman spectra of Ru-TPA$_2$ and its ligands.

TABLE 3.3. Raman shift [cm^{-1}] and assignment of the bands observed in the powder of TPA, bpy-TPA$_2$, and Ru-TPA$_2$ at 632.8 nm excitation.

TPA	bpy-TPA$_2$	Ru-TPA$_2$	Vibrational Assignment
—	1632 (vs)	1633 (m)	ν(C=C) (C-H chain, trans)
1605 (s)			ν(C=C) (monosubst. B)
—	1603 (vs)	1606 (vs)	ν(C=C) (monosubst. B) + ν(C=C) (bpy)
1590 (s)	1590 (vs)	1588 (vs)	ν(C=C) (monosubst. B)
—	—	1537 (m)	ν(C=C) (bpy)
1493 (w)	1493 (vw)	—	ν(C=C) (monosubst. B)
—	—	1490 (m)	ν(C=N) (bpy)
—	1440 (w-m)	1432 (w)	ν(C=N) (bpy)
1331 (w)	—	—	C-H bend
—	1334 (w)	1330 (w-m)	C-H bend + C-H def (C-H chain)
1314 (w-m)	1313(w-m)	—	ν(C-N) (TPA) + C-H bend
1295 (w-m)	—	—	ν(C-N) (TPA) + C-H bend
1281 (m)	1284 (w)	1273 (m)	ν(C-N) (TPA) + C-H bend
—	1252 (w-m)	1252 (sh)	ν(C-N) (TPA) ?
1190 (m)	—	1190 (sh)	C-H bend
1173 (m-s)	1175 (m)	1175 (m-s)	C-H i-p bend (monosubst. B)
1156 (m)	1164 (m)	—	C-H i-p bend
1028 (m)	—	—	C-H def (monosubst. B)
—	—	1024 (m-s)	ring breath (bpy) + C-H def (monosubst. B)
1000 (vs)	995 (w-m)	—	ring def (monosubst. B)
716 (m)	706 (w)	712 (w)	ring def
412 (w)	412 (vw)	415 (vw)	i-p ring def (monosubst. B)

ν = stretching, bend = bending, def = deformation, i-p = in plane
v = very, s = strong, m =medium, w = weak, sh = shoulder

seen, even though there are four of these groups in the complex. With the red laser, a shoulder above 1700 cm^{-1} is observed, but it is not clear whether this is a real peak or an artifact produced by the fit used to remove the background.

For the line assignment of this dye, two publications [62, 63] were used, in which the authors investigated polyaniline and poly(triphenylamine), respectively.

The lines of the PF_6^- anion of the Ru-TPA$_2$ were not observed in the recorded Raman spectra. Benial et al. [64] reported a strong band due to a stretching mode of the PF_6^- anion at 443 cm^{-1}, which was not found here either.

3.1.3 FTIR Investigations

Fourier transform infrared spectra of the samples were measured using a Bio-Rad Digilab FTS 40 FTIR spectrometer. The FTIR spectra of the dyes and of TBAI, TPA, and the bpy-TPA_2 ligand were measured in KBr pellets using typically 32 scans with a resolution of 4 cm^{-1}. The background was removed by subtracting the signal obtained with a pure KBr pellet.

N719

In Fig. 3.7 the FTIR spectra of N719 and of TBAI are shown. The upper graph shows almost the whole measured range, whereas in the lower graph the enlarged scale between 400 and 2250 cm^{-1} is presented. From the comparison of the two spectra it is obvious that at high wavenumbers, the ν(C-H) of the TBAI C-H chains can be observed at 2961, 2935, 2874 cm^{-1} in both spectra. In the lower-frequency range, only the line due to CH_2 deformation at 1467 cm^{-1} contributes to the total signal of the dye. Our results and line assignment are compared with published data in Table 3.4.

Compared to the resonance Raman spectrum of this dye, the IR spectrum is quite complicated, since lines due to all parts of the molecule seem to be present. The very strong ν(C=N) band of the thiocyanate group is present at 2102 cm^{-1}. Contrary to the Raman measurements, bands due to the protonated and deprotonated carboxy groups can be well distinguished. For the carboxylic acids the ν(C=O) modes appear at 1715 and 1673 cm^{-1}, and the ν(C-O) between 1310 and 1235 cm^{-1}. As far as the carboxylates are concerned, the $\nu_{asym}(COO^-)$ appears at 1612 and the $\nu_{sym}(COO^-)$ at 1374 cm^{-1}. The fact that there are two lines corresponding to the C=O stretching mode can be ascribed to the nonequivalence of the carboxylic groups in the complex, which leads to vibrations of different energy. This splitting of the bands has already been observed in the completely protonated sample (also named N3) [7]. In these experiments the ν(C=O) can be seen at 1740 and 1708 cm^{-1}, due to cis and trans carboxylic groups with respect to the other ligand or to the bipyridine, respectively. The rest of the important peaks are associated with ν(C=C), ν(C=N), or ring breathing of the bipyridines.

Ru-TPA_2

The FTIR spectra of $[Ru(dcbpyH_2)_2(bpy\text{-}TPA_2)](PF_6)_2$, of TPA and, of the bpy-TPA_2 ligand were recorded and compared with each other, similar as was done in the case of Raman measurements. The results are presented in Fig. 3.8.

As was pointed out previously in conjunction with the Raman spectra, the signals of the bpy-TPA_2 ligand dominate also the IR absorption. In all three spectra we can observe the strong bands of TPA corresponding to ν(C=C) of the monosubstituted benzene

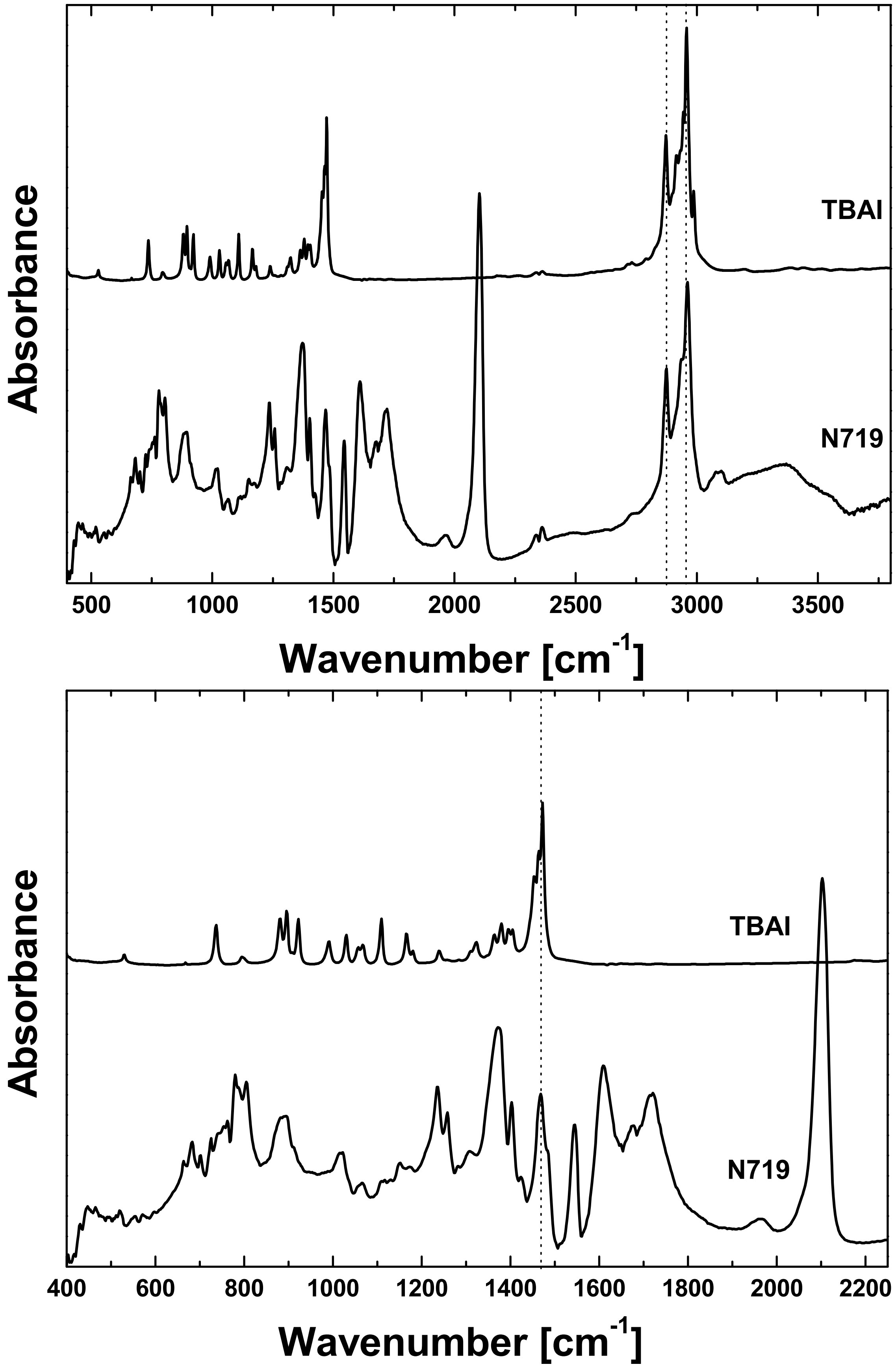

FIG. 3.7. FTIR spectra of N719 and TBAI in KBr pellets.

TABLE 3.4. Wavenumbers [cm^{-1}] and assignment of the absorption bands observed in the powder of N719 and comparison with literature data.

N719 KBr pellet	N719 (Ref. [7]) solid sample[a]	N719 (Ref. [59]) KBr pellet	Vibrational Assignment
2102 (vs)	2105 (vs)	2100 (m)	ν(C=N) (SCN)
1715 (m)	1719 (s)	1715 (s)	ν(C=O)
1673 (m)	—	—	ν(C=O)
1612 (s)	1627 (m-s)	1615 (m-s)	$\nu(\mathrm{COO}^-)$ asym + ν(C=C) (bpy)
1542 (m)	1543 (m)	1549 (m)	ν(C=C) (bpy)
1482 (sh)	—	—	ν(C=C) + ν(C=N) (bpy)
1467 (m)	1470 (m-s)	1480	CH_2 def (TBA)
1403 (w)	1409 (m-s)	1412	ν(C=C) + ν(C=N) (bpy)
1374 (s)	1375 (s)	1371 (m-s)	$\nu(\mathrm{COO}^-)$ sym
1309 (vw)	—	—	ν(C-O) + ν(C=C) intern-ring (bpy)
1258 (w-m)	—	—	ν(C-O) + ν(C=C) intern-ring (bpy)
1237 (m)	1235 (s)	1230 (vs)	ν(C-O)
1022 (m)	1019 (w-m)	—	ring breathing (bpy)

ν = stretching, bend = bending, def = deformation

v = very, s = strong, m =medium, w = weak, sh = shoulder

[a] photoacoustic FTIR spectrum

at 1585 and ~1490 cm^{-1}, the C-N stretching and C-H bending in the 1330-1280 cm^{-1} region, and the lines at 750 and 698 cm^{-1} characteristic of the monosubstituted benzene ring (C-H stretching and C-C def, respectively).

The FTIR spectrum of the bpy-TPA_2 ligand features new lines due to the bipyridine and the C-H chain (in trans configuration) connecting the TPA with the bipyridine unit. The ν(C=C) and ν(C=N) lines of bipyridine appear at 1615, 1543, 1421, and 1374 cm^{-1}. The band at 1508 cm^{-1}, could also be ascribed to bipyridine, but its intensity is much stronger as compared to the other bpy vibrations. Hence, we attributed it to ν(C=C) of the disubstituted benzene (attached to the C-H chain). The alkene group shows several bands of medium to weak amplitude, a ν(C=C) band at 1630 cm^{-1}, a C-H deformation band which overlaps a C-H bending band of TPA around 1330 cm^{-1}, and another weak C-H deformation at 968 cm^{-1}. The ν(C-N) at 1277 cm^{-1} and the lines at 750 and 698 cm^{-1} corresponding to the TPA decrease in intensity as compared to the other peaks. However, a new line at 836 cm^{-1}, corresponding to the 1,4-disubstituted aromatic rings shows up.

The signal of the complete dye contains in addition two ν(C=O) vibrations at 1722 and 1670 cm^{-1}, due to the nonequivalent carboxylic acids, as was also observed for the N719 dye. A ν(C-O) line appears at 1234 cm^{-1}, and probably the other bands

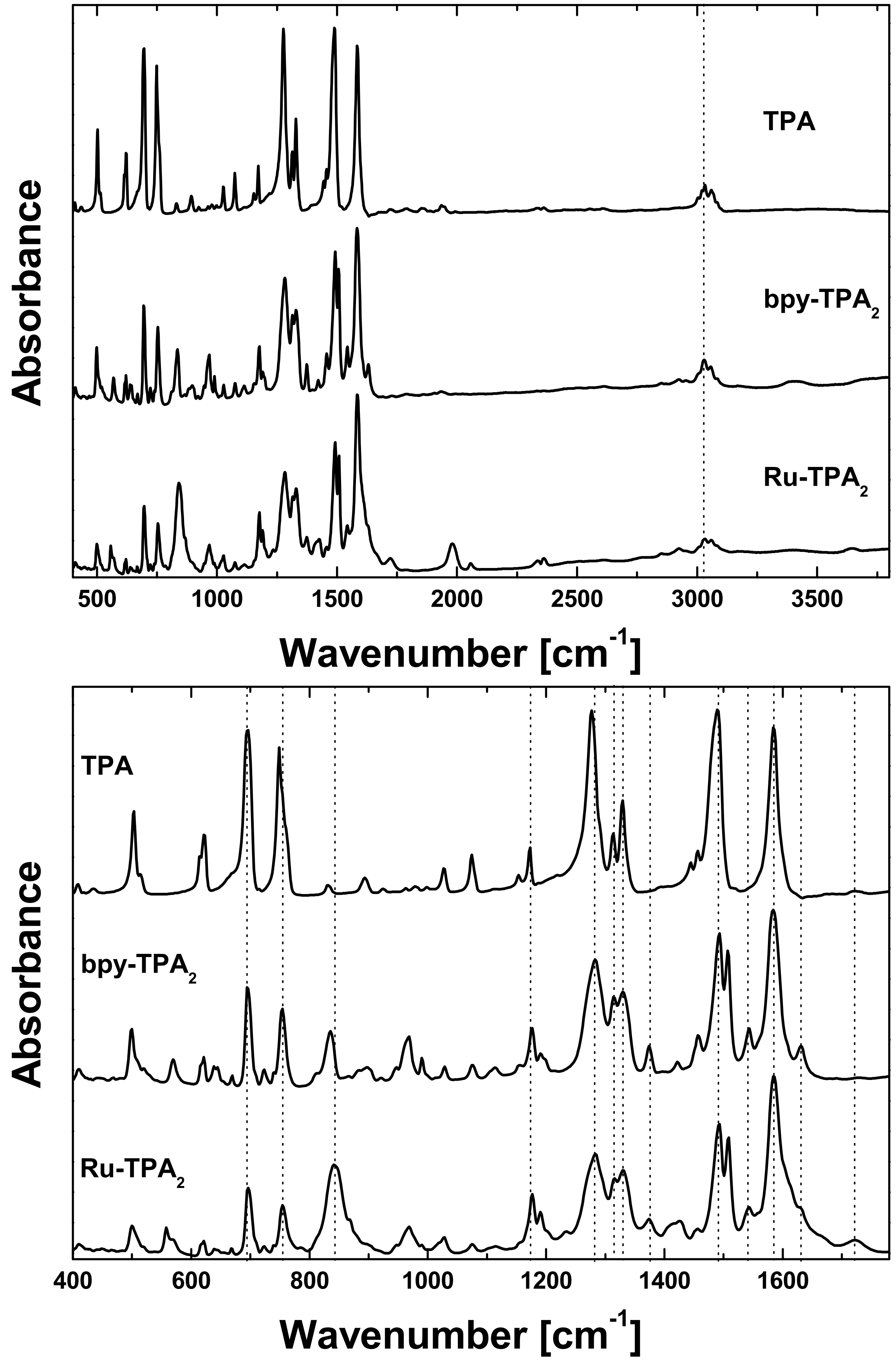

FIG. 3.8. FTIR spectra of Ru-TPA$_2$ and different ligands in KBr pellets.

TABLE 3.5. Wavenumbers [cm^{-1}] and assignment of the absorption bands observed in the powder of TPA, bpy-TPA_2 and Ru-TPA_2 in KBr pellets.

TPA KBr pellet	bpy-TPA_2 KBr pellet	Ru-TPA_2 KBr pellet	Vibrational Assignment
—	—	1722 (w)	ν(C=O)
—	—	1670 (sh)	ν(C=O)
—	1630 (w-m)	1630 (w-m)	ν(C=C) (C-H chain, trans)
—	—	1615 (sh)	ν(C=C) (bpy)
1585 (vs)	1585 (vs)	1585 (vs)	ν(C=C) (monosubst. B)
—	1543 (w-m)	1543 (w)	ν(C=C) (bpy)
—	1508 (s)	1508 (s)	ν(C=C) (disubst. B)
1490 (vs)	1493 (s-vs)	1493 (s)	ν(C=C) (monosubst. B)
1456 (w-m)	1456 (w-m)	1457 (vw)	ν(C=C) (TPA)
—	1421 (vw)	1426 (w)	ν(C=N) (bpy)
—	1374 (w-m)	1374 (w-m)	ν(C=N) (bpy)
1329 (m-s)	—	—	C-H bend
—	1330 (m-s)	1330 (m-s)	C-H bend + C-H def (C-H chain)
1313 (m-s)	1314 (m-s)	1316 (m-s)	ν(C-N) (TPA) + C-H bend
—	1292 (sh)	1292 (sh)	ν(C-N) (TPA) + C-H bend
1277 (vs)	1283 (s)	1283 (m-s)	ν(C-N) (TPA) + C-H bend
—	—	1234 (w)	ν(C-O)
—	1191 (w)	1191 (w)	C-H bend
1172 (w-m)	1176 (w-m)	1176 (w-m)	C-H i-p bend (monosubst. B)
1028 (w)	1028 (vw)	1027 (vw)	C-H def (monosubst. B)
—	968 (m)	968 (w)	C-H def (C-H chain, trans)

ν = stretching, bend = bending, def = deformation, i-p = in plane
v = very, s = strong, m =medium, w = weak, sh = shoulder

corresponding to this vibration are present, too, but overlapped by the strong ν(C-N) and C-H bending signals which are also in this region. It is worth mentioning that these bands corresponding to the carboxy groups are weak as compared to the strong TPA lines.

A strong peak corresponding to the PF_6 counterion at ~838 cm^{-1} was reported in the literature [64], which is in agreement with our measurements.

There are two bands at 1980 and 2058 cm^{-1} which could be ascribed to overtones or combinational bands, but it is difficult to explain their exact origin and the reason of their large amplitude.

3.2 Titanium Dioxide

Photoelectrochemical cells based on dye-sensitized nanocrystalline TiO_2 have shown promising prospects for practical applications and also have stimulated enormous interest in fundamental research. These solar cells have a sandwich structure of TiO_2/dye/electrolyte or hole conductor between two current collecting electrodes. Nanocrystalline titania (nc-TiO_2) films provide huge interior surfaces for attachment, which ensures high light harvesting efficiencies. The porous structure of nc-TiO_2 enlarges the surface area by a factor of about 1000 as compared to a flat surface. The use of a compact layer of TiO_2 between the working electrode, FTO (fluorine-doped tin oxide) in our case, and the nc-TiO_2 layer helps to avoid short circuiting and loss of current through recombination at the FTO electrode. The introduction of such a layer enhances the maximum current output by three to four orders of magnitude [43, 65].

TiO_2 is a wide-band-gap semiconductor. The energy gap, E_g, varies between 3.0 and 3.2 eV, depending the structural modification of the material. In nature, there are three different crystalline forms of TiO_2: anatase (tetragonal), rutile (tetragonal) and brookite (orthorhombic). Furthermore, two high-pressure phases of titania are known: TiO_2-II and TiO_2-III.

Anatase
tetragonal (D_{4h}^{19})
2 formula units per unit cell
6 Raman active modes (A_{1g}+$2B_{1g}$+$3E_g$)
3 IR active modes (A_{2u}+$2E_u$)

Rutile
tetragonal (D_{4h}^{14})
2 units
4 Raman active modes (A_{1g}+B_{1g}+B_{2g}+E_g)
4 IR active modes (A_{2u}+$3E_u$)

Brookite
orthorhombic (D_{2h}^{15})
8 formula units per unit cell
36 Raman active modes ($9A_{1g}$+$9B_{1g}$+$9B_{2g}$+$9B_{3g}$)

TiO_2-II and TiO_2-III (D_{2h})

The functional properties of TiO_2 depend significantly on the modification (e.g. the anatase form is more photoactive). Overall, it seems that the phases of TiO_2 are closely related to the preparation methods and processing techniques [66].

It was suggested by X-ray diffraction (XRD) studies [67] that the nanophase materials exhibit neither long-range nor short-range order, while Raman scattering studies showed that crystalline order exists in the nanophase. The TiO_2 powders and/or nanophase materials present all the essential Raman features observed in the Raman spectra of single crystals, with similar phonons frequencies. The most common phases observed in TiO_2 nanoparticles are rutile and anatase, although also brookite accompanying anatase has been observed [68].

In this second part of chapter 3, different titania substrates are characterized which were used in the experiments (see chapter 5).

3.2.1 Raman Investigations

Raman scattering can be used as a morphological probe for TiO_2 materials as well as a simple and efficient technique to evaluate the particle size. A rigorous determination of the crystallite sizes can, in principle, be obtained by the measurement of the lowest-frequency Raman peak ($\sim$20 cm^{-1}), whose energy varies inversely with the crystallite size. Unfortunately, with the present setup and at room temperature, it cannot be detected.

In the case of anatase, the morphology can also be determined using the low-frequency E_g mode. This mode is well known as a marker for the crystallography of anatase: It appears at 143 cm^{-1} in single crystals and shifts to 154 cm^{-1} in nanocrystalline materials. Similar phenomena of frequency downshift were found in the case of oxygen deficiency or under hydrostatic pressure [66]. The width (FWHM) of the E_g mode varies from 11 cm^{-1} in single crystal to 25 cm^{-1} in nanoparticles [69]. This peak becomes sharper, as the crystal size increases. There are other factors than the size effects that can contribute to the broadening of the Raman and XRD peaks such as the existence of defects which are always present in real particles [70]. All peaks are broadened by finite-size effects in comparison with samples of larger crystals [70].

Blocking and nanocrystalline TiO_2 layers

The TiO_2 blocking layer (bl-TiO_2) was prepared by spray pyrolysis of an aerosol of titanium(IV)bis(acetoacetonato)di(isopropanoxylate) in ethanol, as described in Ref. [65]. The measured thickness of the layer was about 150 nm (since for this value the authors obtained the best performance [65]).

The nanocrystalline anatase paste was provided by A. Hinsch of the Fraunhofer Institut für Solare Energiesysteme (ISE) in Freiburg. It was prepared in the following way. Starting from titanium(IV) isopropoxide, the nc-TiO_2 was obtained by hydrolysis and hydrothermal treatment in an autoclave. This TiO_2 was mixed with

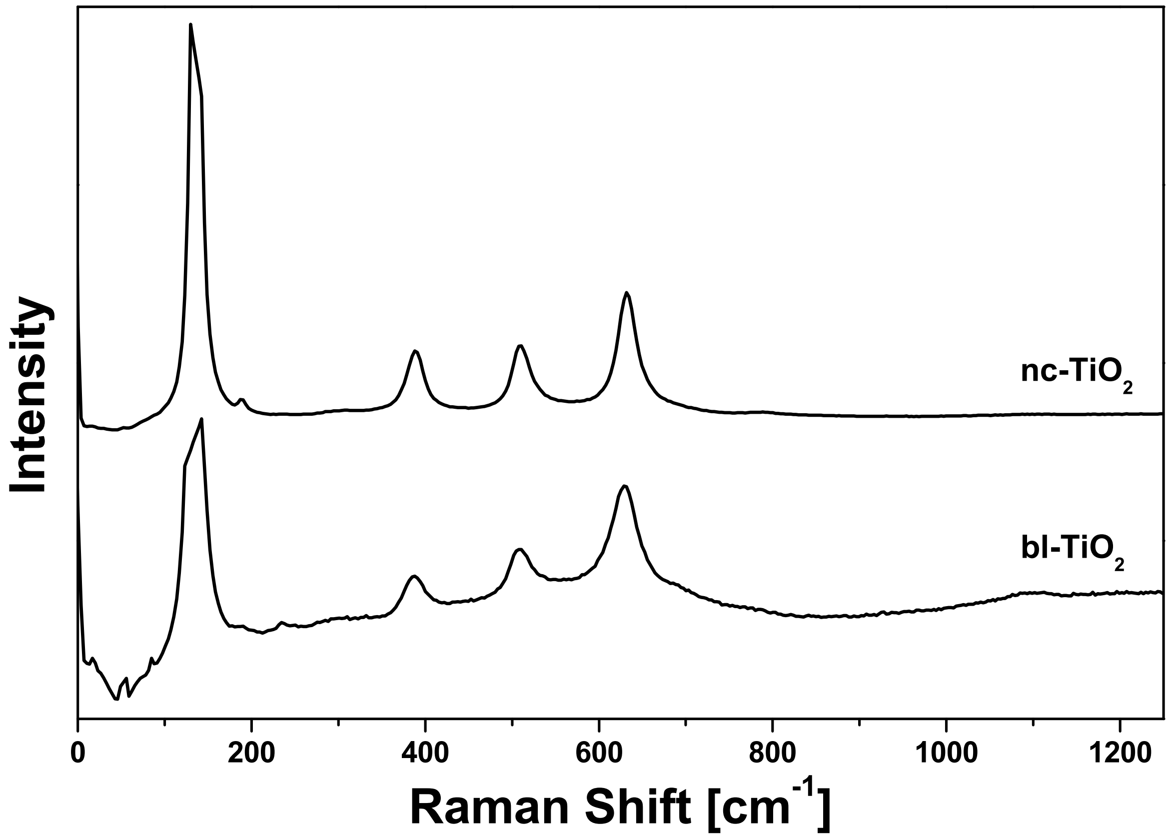

FIG. 3.9. Raman spectra of blocking-TiO$_2$ and nc-TiO$_2$ layer excited with 632.8 nm.

HNO_3/H_2O/polyethylene glycol to get the nc-TiO$_2$ paste. Finally the nc-TiO$_2$ was deposited on the compact titania layer by screen-printing. The thickness of the resulting film was ~ 3 μm.

In Fig. 3.9 the Raman spectra of both layers are shown. Both signals correspond to anatase. As stated earlier in the introduction, the anatase modification has 6 Raman-active modes (A_{1g}+$2B_{1g}$+$3E_g$). In single crystals these modes are located at: 144 (E_g), 197 (E_g), 399 (B_{1g}), 513 (A_{1g}), 519 (B_{1g}), and 639 cm^{-1} (E_g). All lines are present in the observed spectra.

The E_g mode at 144 cm^{-1} is narrower and more intense in the nc-TiO$_2$ than in the blocking layer. Also the other modes are slightly narrower. As was mentioned in the introduction, this mode can be used as a marker for the crystallography of anatase. It becomes sharper and shifts to lower frequencies, as the crystal size increases. Hence, we conclude that the crystallinity of the nc-TiO$_2$ paste is higher than in the blocking layer, i.e. the size of the crystals is bigger. The presence of shoulders and other very weak peaks in the spectra of the bl-TiO$_2$ suggests that it contains a small quantity of another TiO$_2$ modification.

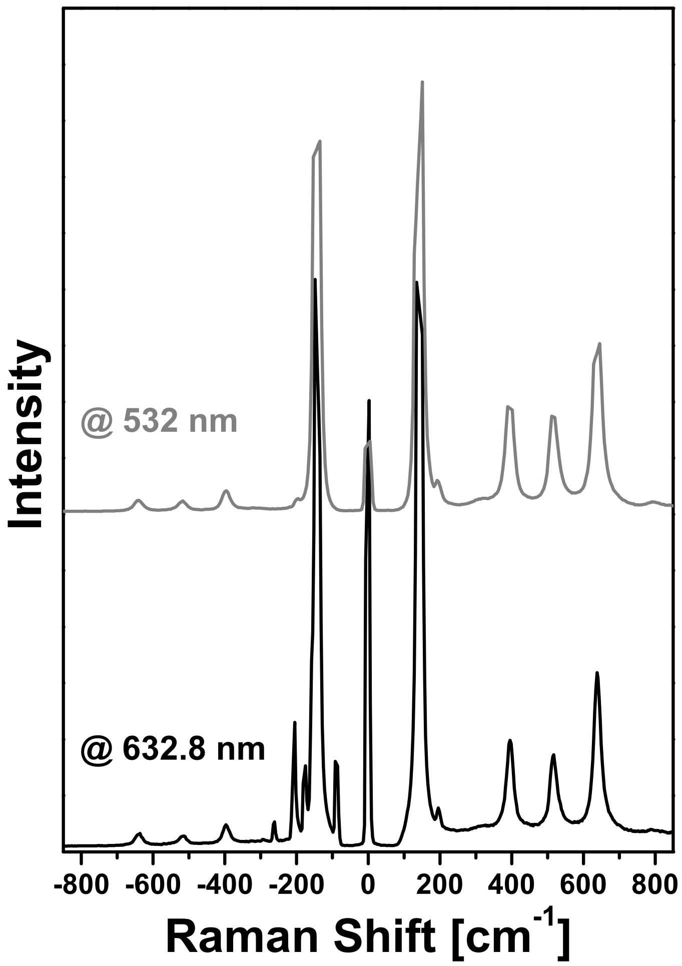

FIG. 3.10. Raman spectra of anatase powder, measured with both lasers.

TiO_2 anatase powder

In some experiments also anatase powder was used. Raman spectra of the white powder were measured with the red laser at 632.8 nm and with the green one at 532 nm. The results are shown in Fig. 3.10. No big differences between the spectra appear, since TiO_2 does not absorb in the visible range. The lines obtained with the green light seem to be broader, but this is only due to different resolution of the monochromator in both spectral ranges. No morphologic distortion or other laser-induced effects were observed under irradiation, even for very high powers.

3.2.2 FTIR Investigations

The FTIR spectrum of the anatase powder was measured in KBr pellets with a Digilab FTS 40 FTIR spectrometer using typically 32 scans with a resolution of 4 cm^{-1}. The background was removed by subtracting the signal obtained with a pure KBr pellet.

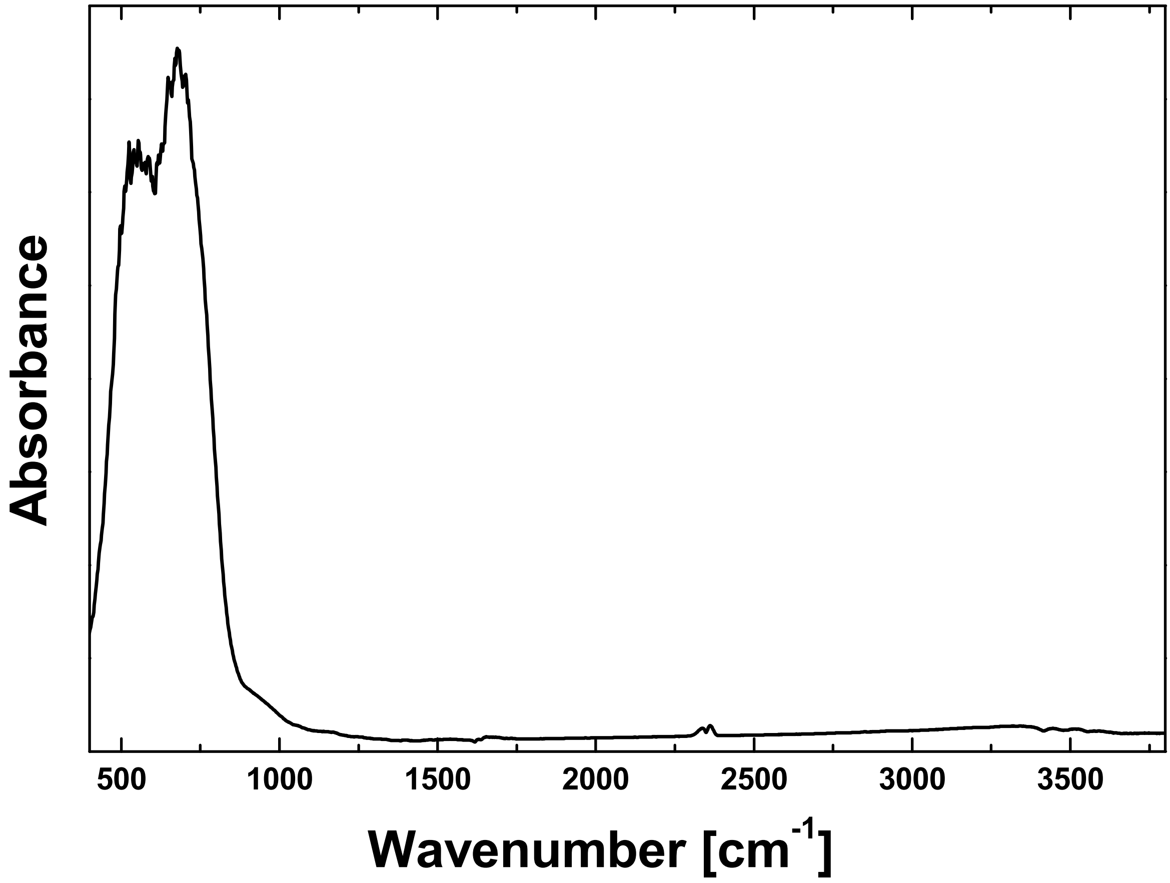

FIG. 3.11. FTIR spectrum of anatase powder in KBr pellets.

Only two strong bands at 558 and 681 cm^{-1} can be observed in the recorded range, which correspond to E_u vibrations of the titania (see Fig 3.11).

3.3 Summary and Conclusions

In the first part of this chapter two dyes with ligands of different nature were characterized. The first one was the well-known $(\text{Bu}_4\text{N})_2[\text{Ru}(\text{dcbpyH})_2(\text{NCS})_2]$ photosensitizer with cyano ligands (N719) and the other one was a new dye, $[\text{Ru}(\text{dcbpyH}_2)_2(\text{bpy-TPA}_2)](\text{PF}_6)_2$, with triphenylamine (TPA) moieties (Ru-TPA_2).

UV-VIS absorption experiments show solvatochromic shifts of the electronic transitions of the two dyes due to H-bonding and donor-acceptor interactions between the ligands and the solvent molecules. The N719 transitions exhibit a blue shift with increasing Gutmann acceptor number, as was already observed for other cyano and thiocyano complexes. In contrast, the Ru-TPA_2 transitions show a red shift with increasing Gutmann donor number of the solvent, except for water, which causes a larger shift than ethanol. An extra contribution of the different deprotonated states of the dyes has also to be taken into account.

The resonance Raman spectrum of N719 suggests that the lowest MLCT transition corresponds to the injection of an electron into the bipyridine ligands. The lines of the TPA ligand dominate the recorded Raman spectra of Ru-TPA$_2$ both with the red and with the green laser. With the green excitation, the bipyridine lines seem to be stronger indicating the influence of preresonance effects. A detailed vibrational line assignment has been performed both, for Raman and FTIR spectra.

In the second part, different types of TiO$_2$ substrates and powders have been described. The Raman and FTIR spectra have been shown and the lines have been assigned to vibrations. The crystallinity of the different samples has been also briefly discussed.

Chapter 4

SERS and SERRS of the Dyes

Surface-enhanced Raman scattering (SERS) is a powerful analytical tool for studying the adsorption of organic molecules on metal surfaces [29, 31, 32]. It is widely accepted that SERS is a complex phenomenon that has its origin in two different mechanisms. The first one is the so-called electromagnetic (EM) effect, which is due to resonances of the incident electromagnetic field with the surface plasmons of the metallic nanostructure. This long-range effect seems to be responsible for the main contribution to the enhancement. The second mechanism is the chemical or charge transfer (CT) effect, which corresponds to photoinduced dynamic charge transfer between the metal and the molecule. This short-range contribution depends on the nature of the system and the experimental conditions. The chemical interaction seems to play an important role, since not all molecules show SERS spectra, but special combinations of adsorbed molecule and metal are required [32]. These two mechanisms operate simultaneously giving rise to the total enhancement. SERS data provide highly sensitive information about the orientation of the adsorbate with respect to the metal surface (EM) and about the nature of the interaction of the molecule with the colloidal system (CT). This technique is described in more detail in the theoretical introduction.

The objective of this chapter is to study the influence of different solvents on the adsorption of two ruthenium dyes on colloidal nanoparticles and their spectroscopic properties. The effects of the solvent on electronic transitions of dye molecules have been extensively studied in the literature; see, e.g., Refs. [4, 49–54]. The wavelength of the absorption maxima of Ru(II) complexes exhibit distinct solvent-dependent shifts (solvatochromism). Solvatochromic shifts can be large for charge-transfer bands, as was already discussed in chapter 3. On the other hand, it was found by Waterland and Kelley using polarized femtosecond transient spectroscopy that the dynamics of the $Ru(dcbpyH_2)_2(NCS)_2$ complex is strongly dependent on the solvent and the excitation wavelength [71]. In the work of Streiff and McHale [54], no solvent dependency was found for any of the vibrational frequencies of the resonance Raman active modes of $[Ru(NH_3)_4bpy]^{2+}$. Webb et al. suggested in Ref. [72] that a close association of

$[Ru(bpy)_3]^{2+}$ with water can produce differences in the resonance Raman spectra, which are a fingerprint of the excited state of the dye. The effects of solvent and electrolyte on the Raman spectrum of $Fe(phen)_2(CN)_2$ adsorbed on a silver electrode, and the adsorption of $[Ru(CN)_5(pyS)]^{-4}$ on different substrates and in different solvents were investigated with SER spectroscopy by Corio et al. [56, 73]. These authors conclude that the chemical nature of solvents and electrolytes plays a decisive role in the SERS of species adsorbed on the electrochemical interfaces, since it can determine the bonding to the surface (electrodes in their case).

In the present study, dyes with ligands of different nature were investigated in order to obtain a better understanding of the influence of the interactions between solvent, complex, and substrate. The role of the different enhancement mechanisms in SERS will be discussed in this context. The dyes were the ruthenium complexes N719 and Ru-TPA_2, which have already been characterized in the previous chapter. Water, ethanol, and acetonitrile were used as solvents, and the SERS substrates were colloidal silver and gold solutions. Part of the results that are presented in this chapter have been published in Ref. [42].

4.1 Experimental Description

The colloidal silver solution was prepared according to [74], using 10 mL of 10^{-2} M $AgNO_3$ solution, which was added dropwise to 90 mL of a 3×10^{-3} M hydroxylamine hydrochloride ($NH_2OH\cdot HCl$) solution.

The gold colloid was prepared by reducing $HAuCl_4$ with sodium citrate following procedure I described in Ref. [22].

The pH of the solutions was adjusted with 1M NaOH solution and measured with commercial pH indicator paper.

For the SERS studies, 1:5 mixtures of dye solution/aqueous colloidal solution were prepared. The concentration of the complexes in the colloidal solutions was below $6\cdot10^{-6}$ M. SERS experiments were carried out in quartz cuvettes of 1 cm thickness.

Also the SERS spectra of tetra-n-butylammonium iodide, triphenylamine (TPA), and bpy-TPA_2 were measured to obtain further spectral information.

The majority of the measurements were performed with the unpolarized HeNe laser at 632.8 nm. Few spectra were recorded with the green laser at 532 nm. For this excitation, resonance and preresonance effects are important, as was already discussed previously.

4.2 SERS in Silver Solutions at 632.8 nm

4.2.1 Acidic pH Values

The aqueous silver solution, as prepared, had a pH value between 4 and 5. The milky-yellow solution had a UV-VIS absorption band around 430 nm with a FWHM of ~130 nm. Under these conditions the first part of the measurements were conducted. When the dye solutions were added to the aqueous colloidal solutions to produce the final SERS samples, sometimes aggregation occurred [75] leading to precipitation of the metal nanoparticles with the adsorbed dye. The spectra could then be measured either in the solution or by focusing on the precipitate. Usually the signals were identical, but in the spectra obtained from the precipitate, the lines of the solvents were less pronounced and better spectra could be recorded. In the case of N719, however, slightly different signals were measured, when the solvent was water or ethanol (see Fig. 4.1). For water, the signal recorded in the precipitate is marked as water(I) and that of the solution as water(II). The behavior in ethanol was similar as in water. In Fig. 4.1 the spectra in water are presented, since the H_2O lines have almost no overlap with the lines of the dye in the spectral region of interest.

N719

The bipyridine lines predominate in the SERS spectra of N719, as was already reported by other authors for RS [59], RRS [15,76], SERS [3,61,77], and SERRS [78–80] experiments on the same dye and similar complexes. Minor differences in the intensities of these bands are present between the spectra of the complex in different solvents (see Fig. 4.1). The symmetric stretching mode $\nu(COO^-)$ appears in the aqueous solution, whereas it is completely missing in acetonitrile. The $\nu(C{=}O)$ mode shows the opposite behavior; its intensity decreases from acetonitrile to water. The thiocyanate band at $\sim 2150\ cm^{-1}$ varies in the same way, and in the water(I) spectrum it shows a shoulder at lower frequencies.

In the article of Finnie et al. [59], the regular Raman spectra of $Ru(dcbpyH_2)_2(NCS)_2$, $(Bu_4N)_2[Ru(dcbpyH)_2(NCS)_2]$, and $(Bu_4N)_4[Ru(dcbpy)_2(NCS)_2]$ powders were recorded with an excitation wavelength of 1064 nm. At this wavelength no resonance effects are present. The comparison of the present results with those of Finnie et al. leads to the conclusion that the dye behaves as fully protonated in acetonitrile and partially or completely deprotonated in water and ethanol.

The pK_a values of deprotonation of $Ru(dcbpyH_2)_2(NCS)_2$ (fully protonated complex), also named N3, were determined by spectrophotometric titration by Nazeeruddin et al. in Ref. [4]. UV-VIS measurements were performed in a 1:5 ethanol/H_2O mixture over the pH range 1-11. The ground-state pK_a's can be obtained from the relationship between the change in the optical density or the peak maximum with the pH for a given

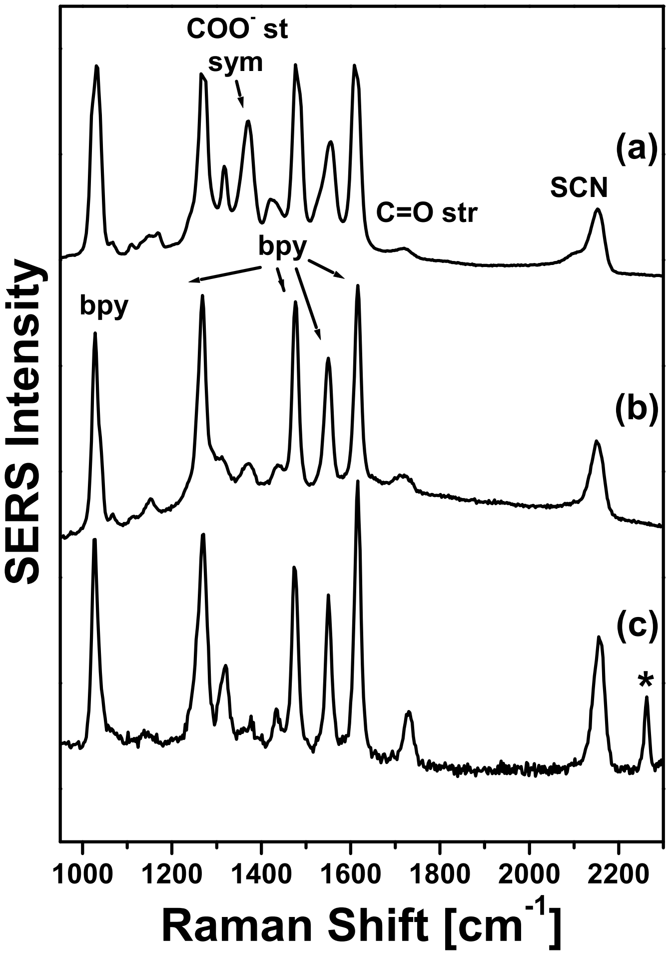

FIG. 4.1. SERS spectra of N719 at pH 4–5 in **(a)** water (I), **(b)** water (II), and **(c)** acetonitrile with the silver colloid at 632.8 nm excitation. The behavior in ethanol is similar as in water. ⋆ Line of acetonitrile.

wavelength. The inflexion points provide the pK_a values. The authors observed that the dissociation of the carboxy groups occurs stepwise, with the first deprotonation step (one carboxy group of each dcbpy unit) having pK_a = 1.5 and the second step (all carboxylic groups being dissociated) pK_a = 3; see the deprotonation sequence in Fig. 4.2. This non-simultaneous dissociation suggests that the pyridyl subunits are nonequivalent, as it is also suggested by the presence of separate IR lines corresponding to the different groups (see chapter 3).

According to these results, the majority of the $(Bu_4N)_2[Ru(dcbpyH)_2(NCS)_2]$ molecules should be completely dissociated at pH values of 4–5. For the acetonitrile solution, however, some correction factors have to be included. The pK_a values increase with increasing concentration of organic solvents, as was discussed in Ref. [81]. The presence of acetonitrile as a cosolvent produces a stronger effect on the pK_a values than other organic cosolvents studied, (e.g., ethanol). This behavior is mainly attributed to two

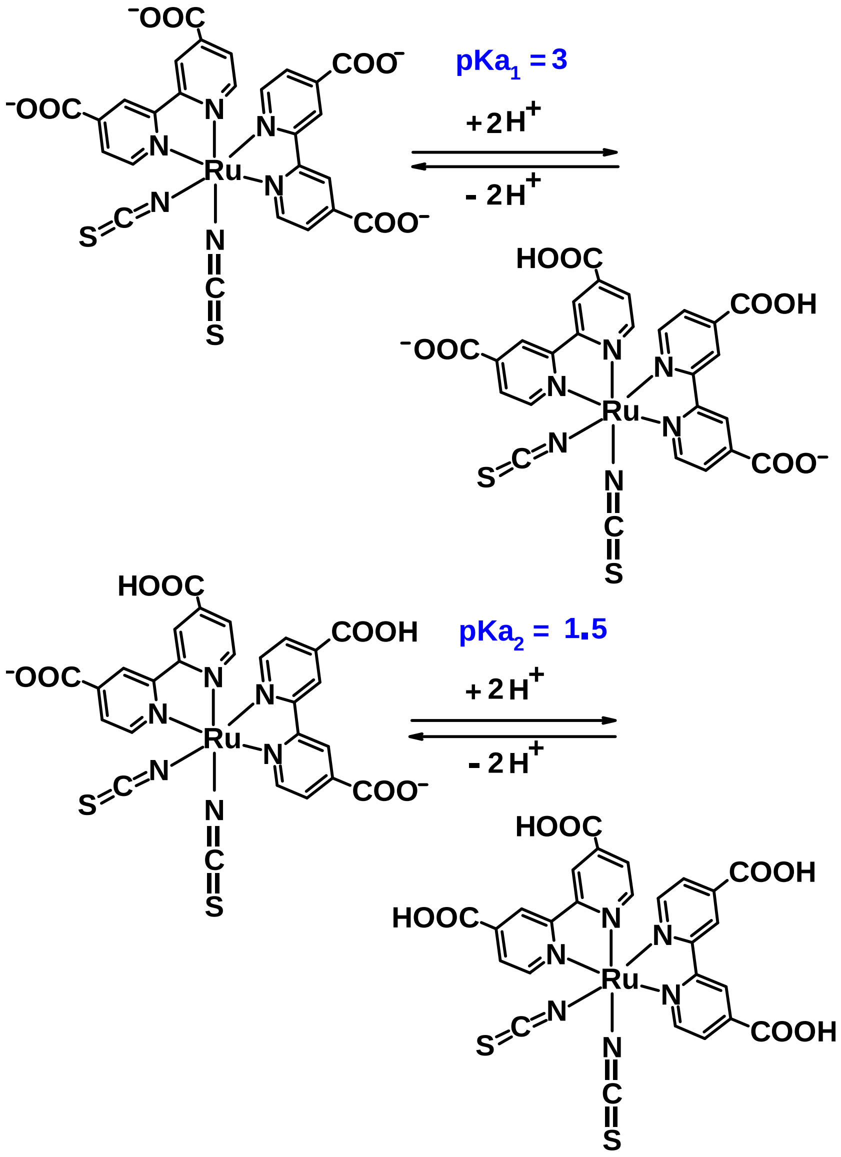

FIG. 4.2. Deprotonation sequence of the fully protonated complex N3.

effects, solute-solvent interaction and proton-solvent interaction. Acetonitrile is considered to be both a poorer acceptor and a poorer donor of hydrogen bonds as compared to water. Thus, acetonitrile is not able to stabilize the carboxylate groups, since it cannot establish H-bonds with them (*solute-solvent interaction*). On the other hand, acetonitrile is a very weakly basic solvent and does not favor the dissociation of the carboxylic acid (*proton-solvent interaction*). In Ref. [81], the dissociation constants for several dicarboxylic acids in various hydroorganic media were measured. The correction factors of the pK_a of a 1:5 acetonitrile/H_2O mixture were between 0.7 and 1.5 as compared to the pure water solution, and between 0.3 and 0.9 as compared to 1:5 ethanol/H_2O. Thus, it can be concluded that in the acetonitrile solutions investigated here the majority of the molecules are not completely dissociated.

TABLE 4.1. Raman shift [cm^{-1}] and assignment of the bands observed in SERS spectra of N719 at pH 4–5 in different solvents with the silver colloid; excitation wavelength, 632.8 nm.

Powder RRS @ 532 nm	SERS/H_2O^a Ag solution	SERS/CH_3CN Ag solution	Vibrational Assignment
—	2153 (m)	2156 (s)	ν(C=N) (SCN)
2108 (w)	2092 (w)	—	ν(C=N) (SCN)
1726 (vw)	1710 (vw)	1729 (m)	ν(C=O)
1610 (s)	1615 (vs)	1616 (vs)	ν(C=C) (bpy)
—	1555 (m)	—	ν(COO^-) asym ?
1543 (vs)	1540 (sh)	1550 (m)	ν(C=C) (bpy)
1476 (s)	1478 (vs)	1476 (vs)	ν(C=C) + ν(C=N) (bpy)
1430 (w)	1420 (w)	1430 (w)	ν(C=C) + ν(C=N) (bpy)
—	1370 (m-s)	—	ν(COO^-) sym
1313 (sh)	1318 (w)	1319 (w)	ν(C=C) intern-ring (bpy) + ν(C-O)
1287 (m-s)	1270 (vs)	1268 (vs)	ν(C=C) intern-ring (bpy) + ν(C-O)
1263 (s)			ν(C=C) intern-ring (bpy) + ν(C-O)
1024 (m)	1030 (vs)	1028 (vs)	ring breathing (bpy)

ν= stretching, s = strong, m = medium, w = weak, v = very, sh = shoulder

^{a} water(I)

After this first overview of the state of the dye in the different solvents, a more detailed analysis of the observed spectra follows. In acetonitrile the complex is partially protonated, but the COO^- vibrations (with delocalized charges) cannot be seen. On the other hand, the C=O vibration of the undissociated carboxylic acid (with localized charges) is strongly enhanced. A very strong thiocyanate band is found at 2156 cm^{-1}, significantly shifted in comparison with the position at ~2100 cm^{-1} as was measured with RRS at 532 nm and compared with the results of other spectroscopic studies of this dye [1,4,59] in the previous chapter. This indicates that the molecule is adsorbed via its NCS groups, which have free electron pairs. Binding through the carboxylate moieties does not seem to occur. The solvent molecules surround the carboxy groups and keep the Bu_4N unit *bound or attached* to the COO^-, thus avoiding direct contact with the colloidal surface. The lack of signals of the deprotonated forms could be explained with the help of the surface selection rules of the EM mechanism. The vibrations perpendicular to the surface are more strongly enhanced than the parallel modes. Taking this into account, we can expect that the dissociated carboxy groups are tilted with respect to the rest of the molecule, which must be perpendicular to the metallic surface.

In water and in ethanol the dye also binds through its COO^- moieties, as can be deduced from the observation of the symmetric stretching mode of the COO^- group at 1370 cm^{-1}. Two different spectra can be distinguished, the spectrum in the water solution (II), where the complex appears to be half deprotonated, and that measured in the water-dye precipitate (I), where it is found to be almost completely dissociated. In the first spectrum (water (II)), the COO^- line begins to appear, whereas the thiocyanate and the C=O line decrease in intensity. In the second type (water(I)), the C=O band is almost absent, and a shoulder at lower frequencies ($\sim$2100 cm^{-1}) appears on the ν(SCN) line showing the presence of non-equivalent thiocyanate groups. We ascribe these lines to the SCN groups which are either free or bonded to metallic particles, respectively. A further discussion of the bands and their vibrational assignment is contained in Table 4.1.

Ru-TPA$_2$

The SERS spectra of the Ru-TPA$_2$ complex in different solvents with the silver colloid are shown in Fig. 4.3. This complex also appears to be adsorbed on the metallic nanoparticles in different ways for different solvents, as was discussed before for N719. The different binding behavior has a bigger influence on the Ru-TPA$_2$ spectra due to its structure (see Fig. 3.2). The pK_a of this dye is unknown, but from the similar structure one can assume that it should be close to the values measured for the N3 complex. It should be stressed that for this complex the signals in ethanol and in water are different.

When the dye is dissolved in acetonitrile, the SERS signal corresponds mainly to the bpy-TPA$_2$ part and the missing of the strong bpy lines can be noticed. The complex behaves as if it is fully protonated, and seems to attach to the silver particle only via its donor ligands, the TPA (triphenylamine), whose nitrogen atom shows a high affinity to silver. In water it behaves as half or fully deprotonated; the molecule can also bind through its COO^- groups, and a mixture of the signals as observed in acetonitrile and in ethanol is measured. In ethanol, it is almost completely deprotonated. Both bonding mechanisms are possible, but the affinity of the carboxylate groups to silver appears to be higher, and only the signal corresponding to the [Ru(dcbpy)$_2$] part can be observed. Hence, this spectrum is very similar to that of N719. A very weak ν(C=O) shoulder appears in it, indicating that there are still a few protonated carboxy groups present. It is noticeable that in acetonitrile we could not observe the dicarboxybipyridine part, and in ethanol no signal of the TPA arms was seen. Taking into account the EM surface selection rules would not be sufficient to explain the recorded spectra; the chemical or charge-transfer mechanism must be considered as well to understand these strong differences. A deeper discussion of the bands and their vibrational assignment is contained in Table 4.2. The ν(OH) line of the carboxylic-acid groups was not observed in any of the recorded spectra. In some cases it might overlap with the OH bands of the water, but in the majority of the measurements these bands were not seen either.

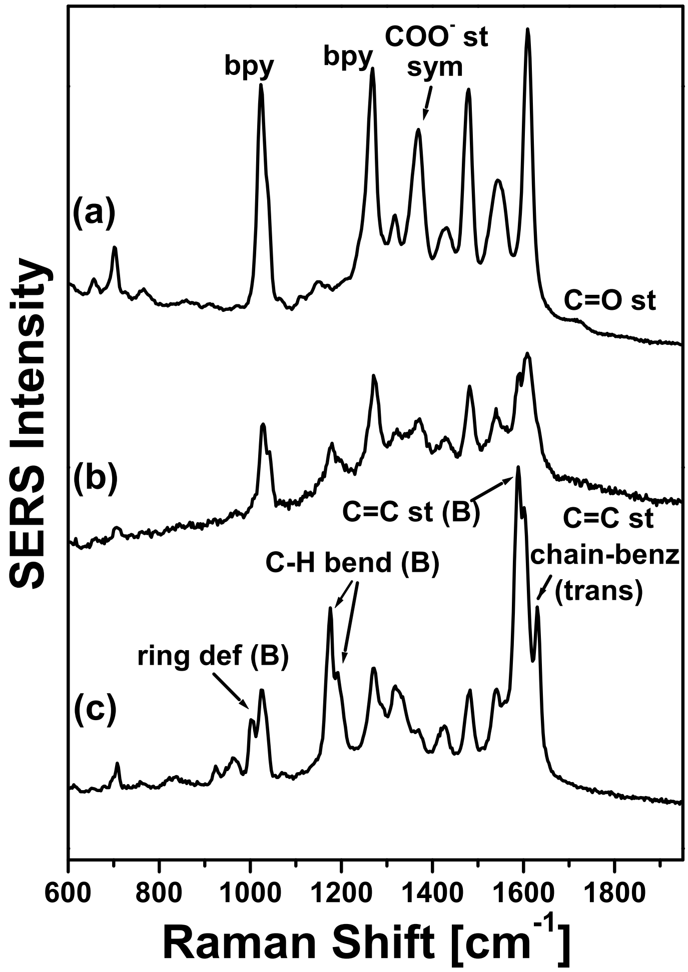

FIG. 4.3. SERS spectra of Ru-TPA$_2$ at pH 4–5 in **(a)** ethanol, **(b)** water, and **(c)** acetonitrile with the silver colloid at 632.8 nm excitation.

Discussion

The fact that the dyes are adsorbed on the colloidal systems in different ways depending on the solvent can be attributed to two different effects. The first one is the solute-solvent interactions which produce variations in the pK_a values and result in differences of the protonation state of the complexes as discussed previously. In Ref. [82] the SER spectra of thiophene-2-carboxylic acid were studied at different pH values, suggesting that the adsorption geometry is pH-dependent, since the molecules were chemisorbed on the metal through different groups. On the other hand, a pH dependence of the SERS of 2,2'-bipyridine adsorbed on silver colloids has been reported in the literature, identifying different kinds of adsorbates [80, 83]. The second effect is H-bonding and donor-acceptor interactions which seem to play an important role in a similar way as for the electronic transitions of the dyes. In acetonitrile, which is an acceptor for hydrogen bonds, the dyes bind through their electron-donor ligands. In water, which is both a

TABLE 4.2. Raman shift [cm^{-1}] and assignment of the bands observed in SERS spectra of Ru-TPA_2 at pH 4–5 in different solvents with the silver colloid; excitation wavelength, 632.8 nm.

Powder	SERS/C_2H_5OH Ag solution	SERS/CH_3CN Ag solution	Vibrational Assignment
—	1704 (vw)	—	ν(C=O)
1633 (m)	—	1630 (s)	ν(C=C) (C-H chain, trans)
—	1609 (vs)	—	ν(C=C) (bpy)
1606 (vs)	—	1603 (vs)	ν(C=C) (monosubst. B) + ν(C=C) (bpy)
1588 (vs)	—	1586 (vs)	ν(C=C) (monosubst. B)
—	1556 (sh)	—	ν(COO^-) asym ?
1537 (m)	1540 (m)	1539 (m)	ν(C=C) (bpy)
1490 (m)	1478 (vs)	1480 (m)	ν(C=N) (bpy)
1425 (w)	1422 (w-m)	1420 (w-m)	ν(C=N) (bpy)
—	1366 (s)	—	ν(COO^-) sym
1330 (w-m)	—	1323 (m)	C-H bend + C-H def (C-H chain)
—	1316 (w-m)	—	ν(C=C) intern-ring (bpy) + ν(C-O)
1273 (m)	—	1281 (m)	ν(C-N) (TPA) + C-H bend
—	1266 (vs)	—	ν(C=C) intern-ring (bpy) + ν(C-O)
1252 (sh)	—	—	ν(C-N) (TPA)?
1190 (sh)	—	1194 (m)	C-H bend
1175 (m-s)	—	1173 (s)	C-H i-p bend (monosubst. B)
1024 (m-s)	1025 (vs)	1026 (m)	ring breath (bpy) + C-H def (monosubst. B)
—	—	1000(m)	ring def (monosubst. B)

ν = stretching, bend = bending, def = deformation, i-p = in plane
v = very, s = strong, m =medium, w = weak, sh = shoulder

hydrogen bond acceptor and a hydrogen bond donor solvent, the complexes also bind through their electron-acceptor ligands. Finally in ethanol, a hydrogen bond donor, the Ru-TPA_2 complex only binds through its electron-acceptor ligands, whereas N719 still binds via both ligands.

In order to better understand the importance of the different contributions to this effect, solutions with a different deprotonation state were also investigated. To this end, some drops of 1M aqueous NaOH solution were added to the solutions, thus changing the pH to basic values.

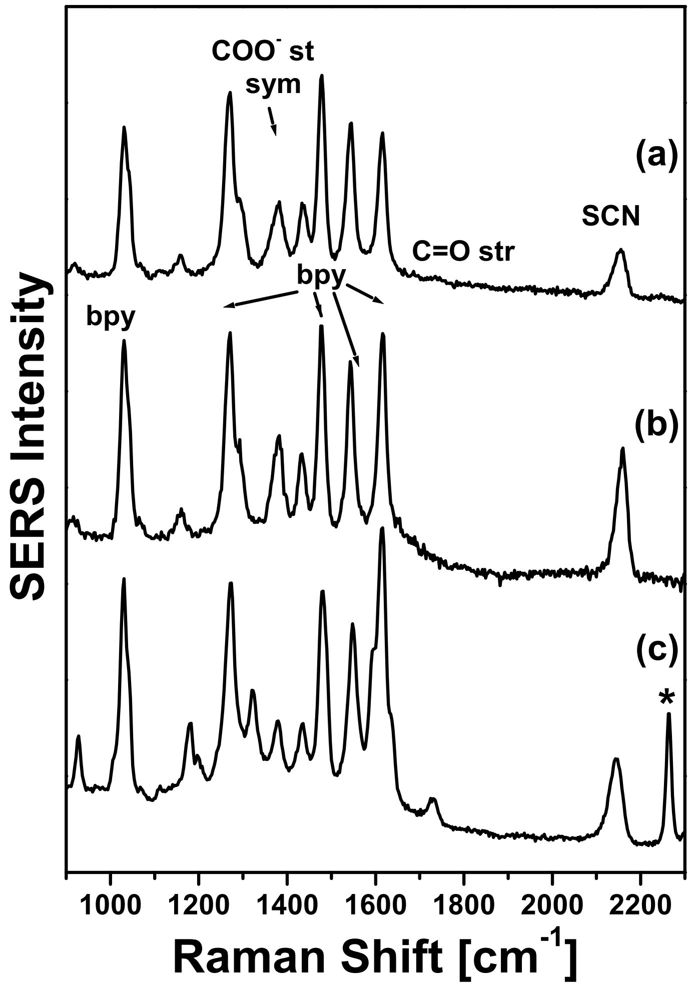

FIG. 4.4. SERS spectra of N719 at pH 12 in **(a)** water, **(b)** water with NaCl, and **(c)** acetonitrile with the silver colloid at 632.8 nm. The behavior in ethanol is similar as in water. ⋆ Line of acetonitrile.

4.2.2 Basic pH Values

The resulting solutions had a final pH value of 12. The results of the SERS measurements show that the behavior is similar, but softened. According to the discussion in the first section of this chapter, at pH 12, even with the corrections for the acetonitrile solutions, the majority of the carboxylic acids must be deprotonated.

It is common in SERS experiments to add further (so called exogenous) compounds in order to activate the colloid or prevent its aggregation [84]. To study the influence of an electrolyte some drops of a saturated aqueous NaCl solution were added to the aqueous dye-silver colloidal solution. The result of this measurement can be seen in Fig. 4.4 together with the other spectra of N719.

The behavior of N719 in ethanol is, as was also found for the acidic pH value, similar to that in water. The spectrum of the aqueous solution does not change very much

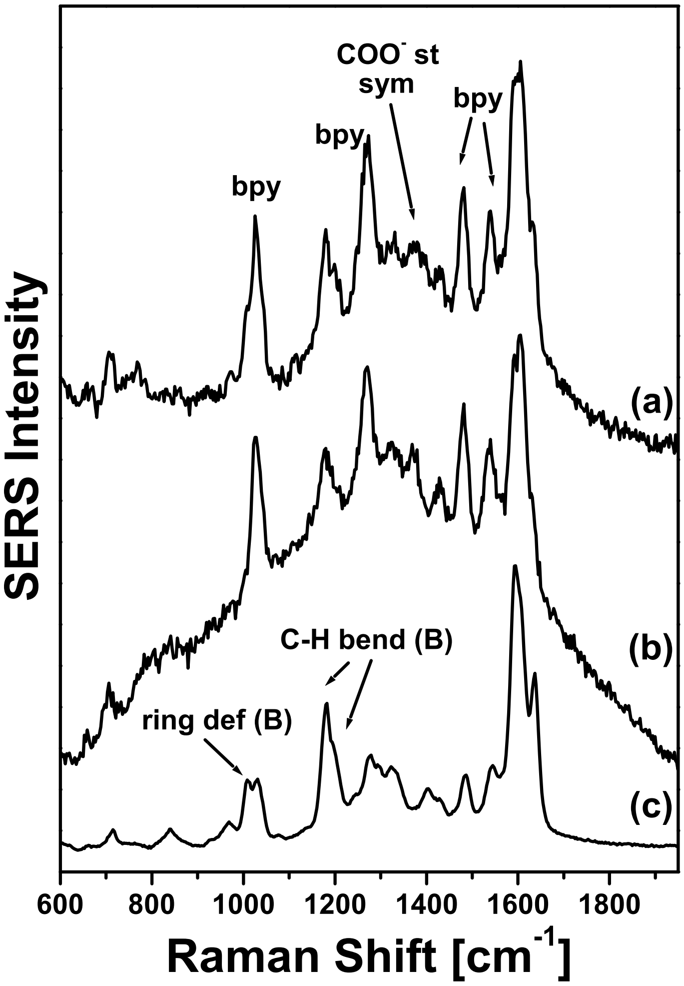

FIG. 4.5. SERS spectra of Ru-TPA$_2$ at pH 12 in **(a)** ethanol, **(b)** water, and **(c)** acetonitrile with the silver colloid at 632.8 nm.

either, but bigger differences appear in the acetonitrile solution. First of all, the line of the carboxylate groups is present and the one corresponding to the protonated form is surprisingly also visible, but much weaker. Moreover, the ν(C=N) band shifts from 2156 cm^{-1} as observed at pH 4–5 to 2144 cm^{-1}, and some "shoulders" show up around the line at 1615 cm^{-1} indicating changes in the absorbing configuration. In both aqueous solutions the thiocyanate line appears at ~2154 cm^{-1} indicating that there is also adsorption via this moiety; it is particularly strong in the sample with NaCl. The presence of the Na$^+$ ions seems to favor the attachment through this ligand, as was already observed by P. Corio et al. in the binding of Fe(phen)$_2$(CN)$_2$ to silver electrodes [56].

The results obtained for Ru-TPA$_2$ in the basic solutions are shown in Fig. 4.5. The behavior is similar to that of the acidic solutions. In the acetonitrile solution, the dye seems to be still attached only by its donor ligand, whereas in the ethanolic and aqueous solutions, a mixture of the signals of both moieties is present.

In summary, even at basic pH values there is an influence of the nature of the solvent on the way how the molecules bind to the metallic particles. In acetonitrile, an acceptor for hydrogen bonds, the binding is favored through their electron-donor ligands. In water and ethanol, both hydrogen bond donors, they are also attached through their acceptor ligands, the dicarboxybipyridines. It is worth noticing that the affinity of the TPA ligands to silver seems to be higher than that of NCS, especially in acetonitrile solution.

4.3 SERRS and Preresonance Effects in Silver Solutions at 532 nm

One of the most interesting properties of SERS, and in particular SERRS, is their high sensitivity, which however, is not equal for all molecules or species adsorbed on the metallic surface, as was already discussed in the introduction. The Raman bands of impurities can be selectively enhanced, even if they are present in a much lower concentration, overlapping the signals of the adsorbate under study and, thus, deforming the results [30, 84]. Therefore, very pure materials have to be used for this kind of experiments.

We have also investigated the influence of the solvents on the adsorption of the dyes on the colloidal metallic particles with surface-enhanced resonance Raman spectroscopy in the case of the N719 complex, and with preresonant effects, for Ru-TPA$_2$. For this purpose a new silver colloid was prepared and measurements at different pH values were performed to clarify the influence of the deprotonation state of the sample. Also the influence of NaCl was studied. Unfortunately, the presence of an organic impurity, or a reaction of the dye with NaOH and/or NaCl gave rise to an additional signal which overlapped the main lines of the complexes in the new solutions. Therefore only few measurements recorded in old solutions can be used in our discussion.

In Fig. 4.6, the spectra of the dye N719 at acidic conditions in water and acetonitrile are shown (in ethanol the behavior is similar as in water). The spectra recorded with both lasers are very similar, but with characteristic differences due to the resonance effect. The thiocyanate band is very weak in the resonant spectra since it does not participate in the corresponding electronic transition. Its position is shifted with respect to the powder spectrum, indicating that this ligand actively participates in the surface binding of the molecule to the metallic particle. In water, the presence of the $\nu(\mathrm{COO}^-)$ at 1370 cm^{-1} shows that the molecule is also bonded to the silver particle via the carboxylate groups, and the lack of this line in the acetonitrile solution, accompanied by the presence of a weak $\nu(\mathrm{C{=}O})$, indicates that here the interaction is not occurring through these ligands. Furthermore, the amplitude of the bands is strongly

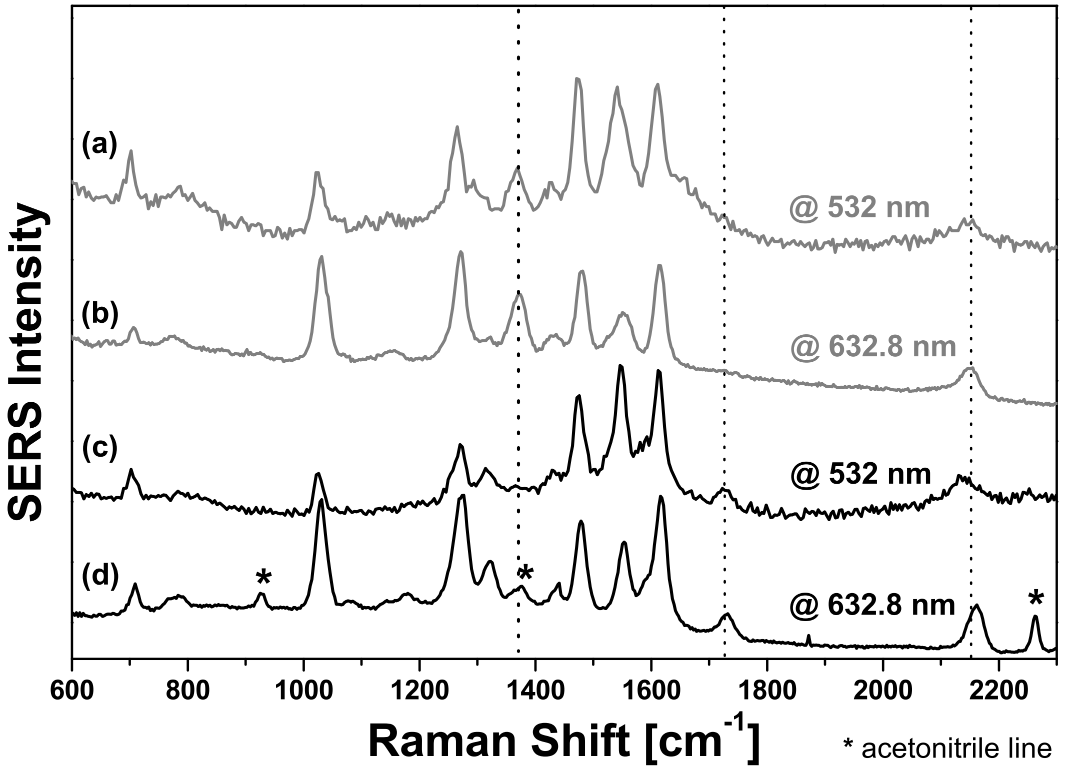

FIG. 4.6. SERS and SERRS spectra of N719 at pH<7 in **(a,b)** water and **(c,d)** acetonitrile with silver colloidal solution.

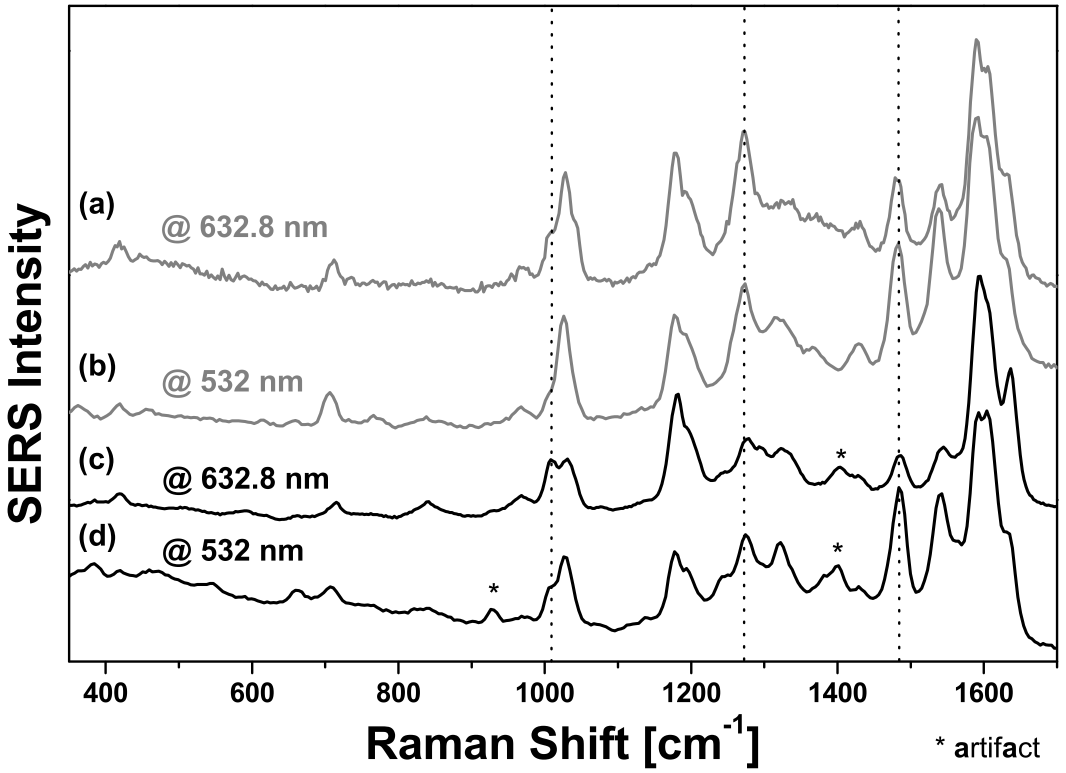

FIG. 4.7. SERS spectra of Ru-TPA$_2$ at pH>7 in **(a,b)** ethanol and **(c,d)** acetonitrile with silver colloidal solution.

influenced by the resonance. The comparison of the SERRS spectra with the RRS of N719 powder (shown in Fig. 3.5) reveals that only the vibrations related with the anchoring to the colloidal system seem to be affected by the adsorption.

For Ru-TPA$_2$, one can see that under basic conditions, in ethanolic and acetonitrile solutions, the spectra are very similar to those observed with the red excitation (see Fig. 4.7). A slight enhancement of the lines corresponding to the bipyridines seems to occur, as was also noticed for the powder signal. In ethanolic solution, the bands at $\sim$1370, 1280, and 1030 cm^{-1}, which are assigned to vibrations of the dicarboxybipyridine ligand involved in the binding of the molecule, do not seem to vary very much due to preresonant effects, whereas the lines at 1539 and 1480 cm^{-1} are clearly affected. These two last peaks were ascribed to the bpy units to which the MLCT seems to take place. This difference may be explained taking into account that these two processes occur in different bipyridines: In the first case, the molecule attaches to the metallic nanoparticle via one of the dicarboxylate ligands; in the second, the electron injection of the lowest MLCT takes place from the ruthenium atom to the bpy of the bpy-TPA$_2$. However, since more results are not available a more detailed interpretation cannot be given.

A new strong band above 3650 cm^{-1} and a background between 3000 and 3600 cm^{-1} due to NaOH appeared in the basic SERS and SERRS spectra of the samples, especially when NaCl was present. The strong line is assigned to the Ag-OH$^-$ vibration. This vibration is affected by resonance effects with the green laser, appearing strongly at 3653 cm^{-1}. For the red excitation this line is much weaker, in some cases not even detectable. But in the solutions with NaCl, this band is enhanced (but still always much weaker than with the green laser) and exhibits large shifts to higher wavenumbers, appearing at $\sim$3680 cm^{-1}.

4.4 SERS in Gold Solutions at 632.8 nm

4.4.1 Acidic pH Values

The aqueous gold solution, as prepared, had a pH value between 4 and 5. The dark red/purple solution featured a UV-VIS absorption band around 528 nm with FWHM of $\sim$120 nm (see Fig. 4.8). In the acidic aqueous gold solutions of both dyes, no SERS signal was observed at all, and in the ethanolic solutions the SERS effect was very weak. In acetonitrile, on the other hand, the enhancement was very strong and the spectra of both dyes could readily be measured. This can be related with the markedly different UV/VIS spectra of the two acetonitrile gold solutions in Fig. 4.8. The vibrational spectra did not show pronounced qualitative differences from the signals recorded in the silver solutions; only quantitative changes occurred.

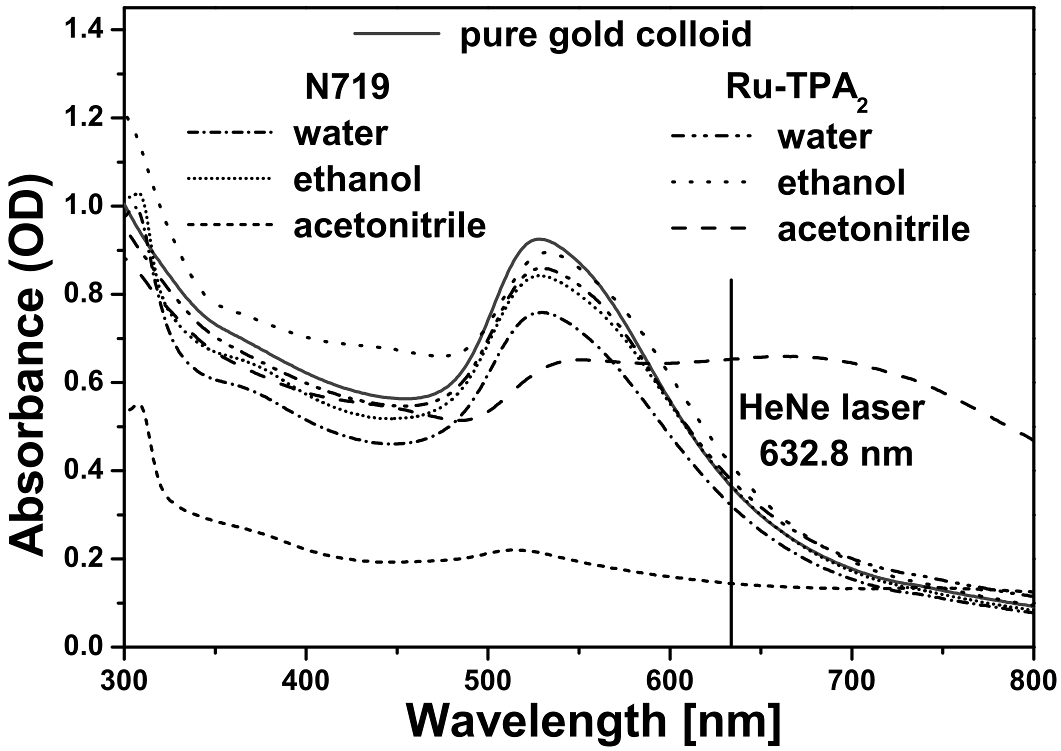

FIG. 4.8. Absorption spectra of the gold colloid with N719 and Ru-TPA$_2$ complexes in different solvents.

In the SERS spectrum of N719 in acetonitrile, the ν(C=N) band of the thiocyanate group at $\sim$ 2150 cm^{-1} turned out to be much stronger and slightly blue shifted (at 2142 cm^{-1}) as compared to the silver solution (see Fig. 4.9). This might be related to a stronger binding of the SCN group to Au than to Ag, as was observed in other studies of Au/SCN and Ag/SCN systems [73, 85]. Apart from this difference the spectrum is like the one recorded on silver: The ν(C=O) appears at 1728 cm^{-1}, the bipyridine lines at 1615, 1550, 1477, 1427, and 1028 cm^{-1}, and the ν(C=C) + ν(C-O) at 1320 and 1267 cm^{-1}, respectively.

The SERS spectrum of Ru-TPA$_2$ in acetonitrile is very similar to that obtained with silver, in which the signal of the bpy-TPA$_2$ ligand is dominating. But in the case of gold, the signal is also affected by some kind of resonance enhancement (SERRS) effects (see Fig. 4.8), since the absorption is shifted to longer wavelengths. This presumably indicates that a charge-transfer mechanism is present in both SERS and SERRS, playing an important role in the enhancement of the Raman spectra. The SERS lines of the dye are at 1629, 1603, 1586, 1540, 1488, 1425, 1326, 1280, 1193, 1173, 1026, and 1002 cm^{-1}.

It is well-known that the SERS effect is stronger with silver than with other metals. Nevertheless, the complete absence of SERS signals in aqueous gold solutions and the weak effect in ethanol is very surprising. Apparently, the interaction with gold is

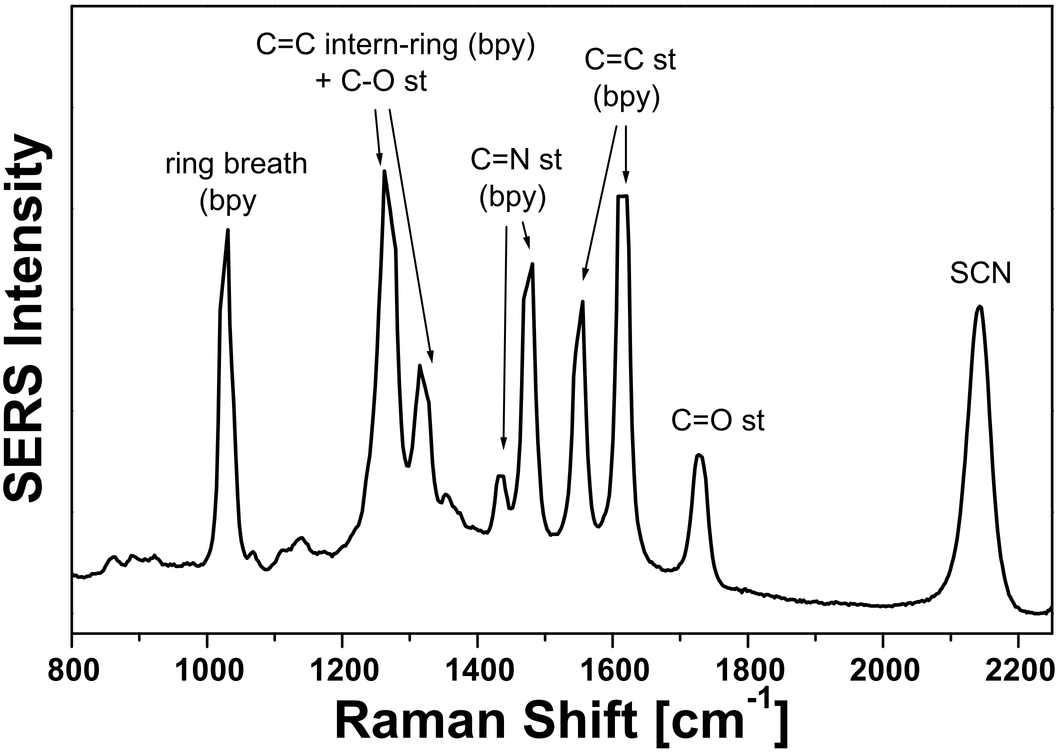

FIG. 4.9. SERS spectrum of N719 at pH 4–5 in acetonitrile with the gold colloid at 632.8 nm excitation.

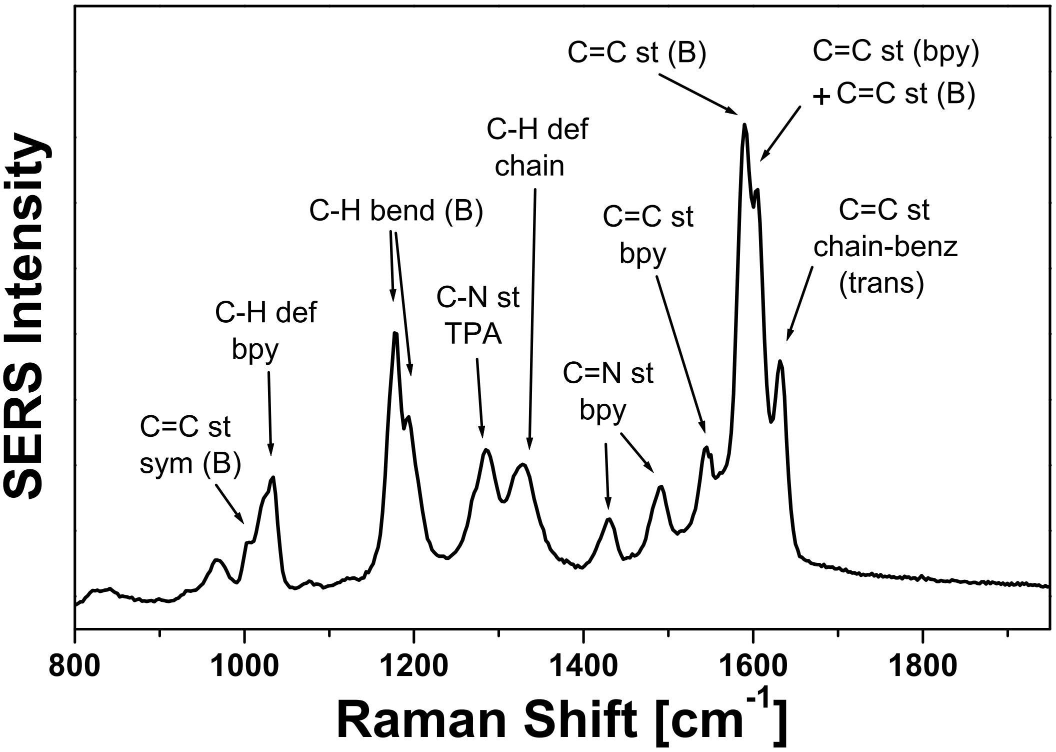

FIG. 4.10. SERS spectrum of Ru-TPA$_2$ at pH 4–5 in acetonitrile with the gold colloid at 632.8 nm excitation.

not strong enough to break the hydrogen bonds between the carboxylic groups and the solvent molecules. The authors of Ref. [49] mentioned that the amine ligands also form H bonds with the solvent molecules and that these bonds produce shifts of the electronic transitions (solvatochromism), as was discussed in the first part of this section. In addition, H-bonding of the solvent molecules to the electron pair of the thiocyanate sulfur can occur, which prevents the NCS groups from attaching to the metallic nanoparticles. Strong hydrogen bonding of hydroxylic solvents with CN moieties was also reported by Corio et al. in Ref. [56]. This hydrogen bonding is less efficient in ethanol, however. Ethanol is a weaker Lewis acid than water, which explains that some contact of the dye with the metallic surface is possible.

In acetonitrile strong SERS signals can be measured for both dyes, and, in addition, a resonant effect is present, mainly for the Ru-TPA$_2$ dye, due to a red shift of the UV-VIS absorption maximum. The corresponding transition involves a charge transfer between the complex and the metallic nanoparticle.

4.4.2 Basic pH Values

By adding few drops of the NaOH solution to the dyes in acetonitrile, a pH of 12 was adjusted. The N719 spectrum is similar to that with the silver colloidal solution: The line of the carboxylate groups appears and the band corresponding to the protonated form is also visible, but much weaker. Moreover, the ν(C=N) band shifts to lower wavenumbers, and some “shoulders” show up around the line at 1615 cm^{-1} indicating changes in the absorbing configuration. Similarly, the Ru-TPA$_2$ complex behaves as in the silver solution and no variations seem to appear with the increase of the pH value. Moreover, the influence of NaCl as an electrolyte in the gold colloidal solutions was briefly investigated, and the results show that the binding via the donor ligands is favored, as was observed with the silver colloid.

4.5 Measurements of bpy-TPA$_2$

In order to get a deeper understanding of the previous discussions of the different behaviors of the dyes in different solvents, in particular the Ru-TPA$_2$, the results of the measurements performed on the bpy-TPA$_2$ ligand will be briefly reviewed. The normal Raman and FTIR spectra of the pristine powder were already shown in the previous chapter. Its intense yellow color prevented the recording of the Raman spectrum with the green laser, due to very strong fluorescence. However, for the complete dye (Ru-TPA$_2$) it could be recorded, as was already shown.

The ligand was dissolved in different solvents, and SERS measurements were performed in the silver and gold colloidal solutions with the two laser excitations. The bpy-TPA$_2$ does not dissolve in water, so no results in this solvent could be obtained. This could

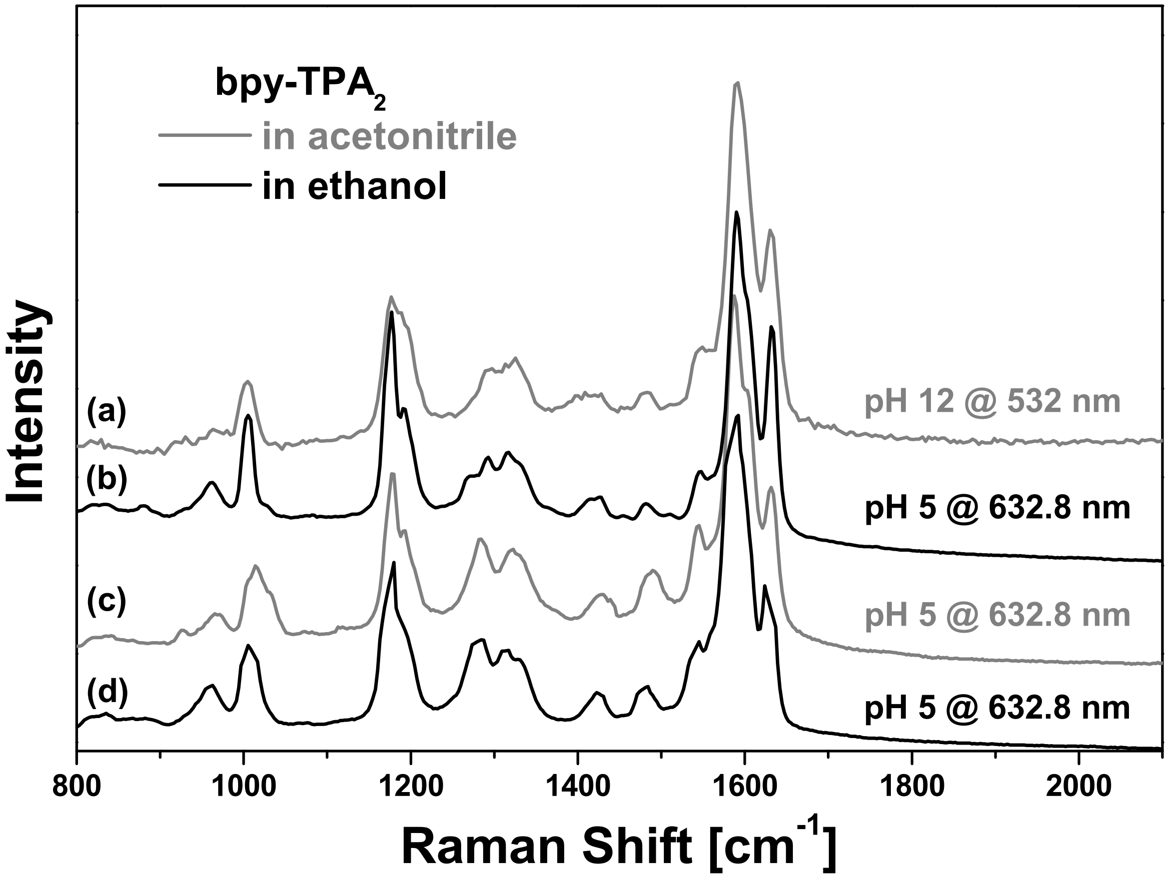

FIG. 4.11. SERS spectra of bpy-TPA$_2$ in different solvents and conditions in **(a,b)** silver and **(c,d)** gold colloidal solution.

---

explain why the Ru-TPA$_2$ dye is poorly soluble in water. The SERS spectra of the ligand in different solvents and colloids at different pH values are shown in Fig. 4.11.

There are several points to be discussed about these results. First of all, it is evident that all spectra are almost identical. The change of solvent and colloidal system does not seem to affect the SERS signal and, therefore, the way of binding to the nanoparticles. Second, the SERS spectra of the bpy-TPA$_2$ are much more similar to the normal Raman spectrum of the dye (Ru-TPA$_2$) than the powder signal and identical to the SERS spectrum of Ru-TPA$_2$ in acetonitrile. This fact can be explained taking into account the binding way of the ligand to the nanoparticles. All nitrogen atoms have very high affinity to the metallic colloid, so the ligand attaches via the N atoms of the TPA and via the N atoms of the bpy. The vibrations of the bipyridine are affected by the presence of the silver or gold particle, which plays a similar "role" as the ruthenium atom with the other part of the complete dye, thus modifying the vibrational spectra. The ν(C=C) and ν(C=N) of the bipyridine show up between 1400 and 1550 cm^{-1}, and the lines of the ν(C-N) of TPA and the C-H vibrations of the chain act as if they were

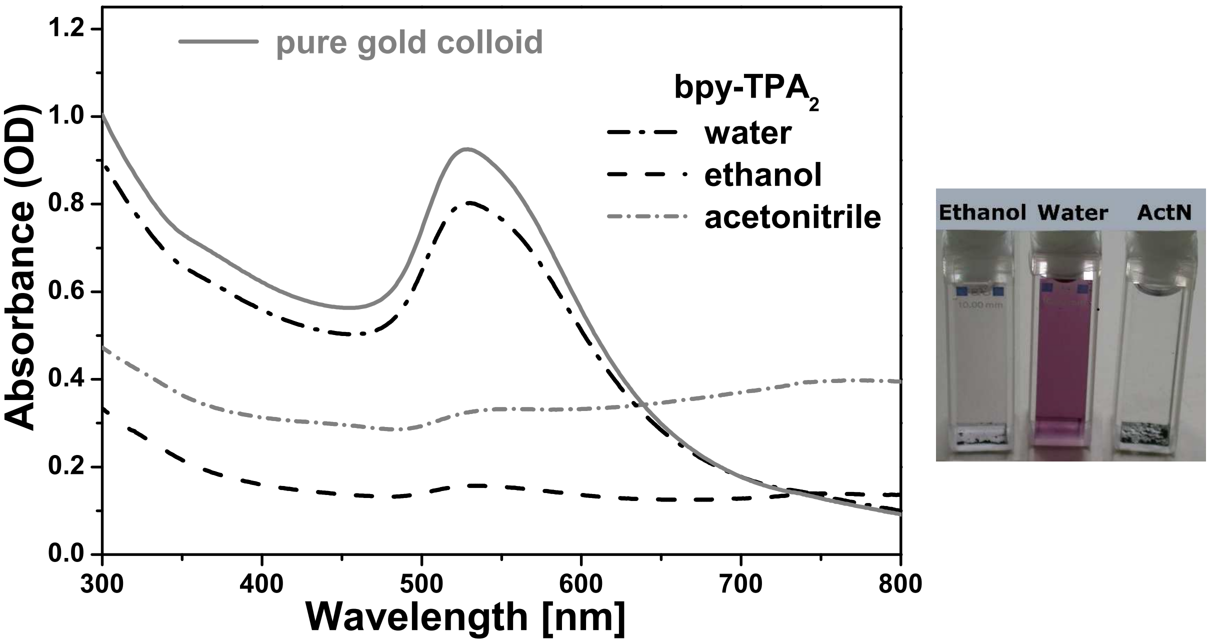

FIG. 4.12. Absorption spectra of the gold colloid solution with the bpy-TPA$_2$ ligand in different solvents. The photograph on the right side shows the three dye solutions.

in the complete dye. Also the C-H bending of the benzenes and the ring breathing of the bipyridines are influenced in this way.

The third point to be pointed out is the presence of strong SERS in ethanolic gold solution. The UV-VIS absorption spectra of the gold colloid solution with bpy-TPA$_2$ in different solvents can be seen in Fig. 4.12. As it was found for the acetonitrile solutions of the complete dyes N719 and Ru-TPA$_2$ (see Fig. 4.8), the absorption maximum shifts to longer wavelengths indicating a charge transfer between the ligand and the metallic nanoparticle. But in the case of bpy-TPA$_2$, also the ethanolic solution shows this effect. This difference can be ascribed to the different charge distribution of the ligand, as compared to the complete complex, and to the fact that it can also bind via the nitrogen atom of the bpy unit.

No influence of the pH value on the SERS spectra of bpy-TPA$_2$ was found, similar to the case of the acetonitrile solutions of the Ru-TPA$_2$ complex. In addition, no effects seem to appear with the change of irradiation wavelength, except for a slight decrease in the intensity of the lines at 1025 and 1175 cm^{-1} with the green excitation (see Fig. 4.11). No preresonance effects occur, since the ILCT transition is at far shorter wavelengths than the lowest MLCT band of Ru-TPA$_2$. With the addition of the electrolyte NaCl, the SERS intensity increases drastically and a new band shows up at 240 cm^{-1}, which is ascribed to a Na$^+$-Ag vibration.

4.6 Summary and Conclusions

The analysis of the recorded spectra reveals that the dyes are adsorbed on the colloidal systems in different ways depending on the solvent. At acidic pH values, when dissolved in acetonitrile (hydrogen bond acceptor solvent), the dyes do not deprotonate completely and bind via their electron-donor ligands, whereas in water (both hydrogen bond donor and hydrogen bond acceptor) they also bind via their electron-acceptor ligands. In ethanol (hydrogen bond donor), N719 has the same behavior as in water, whereas Ru-TPA$_2$ only binds through its electron-acceptor ligands.

At basic pH, there is still an influence of the nature of the solvent on the way how the molecules attach to the metallic particles. In acetonitrile, acceptor for hydrogen bonds, the binding via their electron-donor ligands is favored, whereas in water and ethanol, hydrogen bond donors, they also bind through their acceptor ligands, the dicarboxybipyridines.

The SERRS signals of the dye N719 are very close to the SERS spectra recorded with the red laser, but with the characteristics of the resonance effect. The comparison with the RRS of N719 powder indicates that only the vibrations related with the anchoring to the colloidal system are likely to be affected by the adsorption. For Ru-TPA$_2$, the spectra are also very similar for both excitation wavelengths with a slight enhancement of the lines corresponding to the bipyridines due to preresonance effects.

Furthermore, it turned out that in aqueous gold solutions of the dyes no SERS signal is produced and in ethanolic gold solutions the SERS effect is very weak. This can be ascribed to the smaller affinity of the complexes to gold as compared to silver, which apparently has the consequence that the interaction between dye and gold nanoparticle is not strong enough to break the hydrogen bonds between the dye and the solvent molecules.

Strong SERS signals were recorded for both complexes in the gold solution when dissolved in acetonitrile, and, moreover resonance effects are present, mainly for the Ru-TPA$_2$ dye. The UV-VIS absorption maximum shifts because of a charge transfer between the complex and the metallic nanoparticle. The similarities of the SERS and the SERRS signals of Ru-TPA$_2$ indicate the important role of the chemical enhancement mechanism. Charge transfer, H-bonding, and donor-acceptor interactions are crucial for the interpretation of the observed spectra. The variation of the pH to basic values has the same influence as for the silver solution: N719 shows small variations in its adsorption configuration, whereas the spectra of Ru-TPA$_2$ do not change at all, confirming the strong affinity of the TPA ligands to the gold.

Finally, it is pointed out that the presence of the electrolyte NaCl seems to favor the binding via the donor ligands.

Chapter 5

Adsorption of the Dyes on TiO_2

Ruthenium(II) complexes containing polypyridyl ligands are widely used as photosensitizers in solar cells, as was already mentioned previously. In photovoltaic cells, the dye adsorbed on TiO_2 nanoparticles is excited by absorbing visible light, transferring an electron to the conduction band of the TiO_2. The efficiency of the charge injection process is strongly dependent on the type of binding of the dye to the semiconductor. This suggests that the surface-anchoring form plays an important role for the solar cell efficiency, and it also influences its stability. Therefore, the characterization of the complex adsorption on the titania surface is very important in order to deeply understand the sensitization phenomenon, and then, optimize the performance of the sensitized cells and enhance their quantum yield. However, the manner in which the dye molecules interact with the TiO_2 is not yet well understood and still remains an open question.

The semiconductor/adsorbate interface has been largely studied in the literature using different techniques. Among these, vibrational spectroscopies are the most informative tools, since they are able to offer structural information about both titanium dioxide and photosensitizers, as well as the relevant changes induced by the chemisorption on the semiconductor surface [2, 7, 59, 69, 86–95].

In this chapter UV-VIS, Raman, resonance Raman, FTIR, and ATR-FTIR spectroscopies have been used to investigate the nature of binding of two Ru-bpy complexes on TiO_2. Two types of TiO_2 nanoparticle substrates were used: The first one was a nanocrystalline anatase paste deposited by screen-printing on a compact titania layer on a FTO glass substrate forming a film of $\sim$3 μm thickness, and the second one was anatase nanopowder. Both systems have been described in chapter 3. The dyes are the well-known N719 and the newly synthesized Ru-TPA$_2$ dye, which have already been described and characterized in previous chapters. Both of them contain carboxy moieties as anchoring groups.

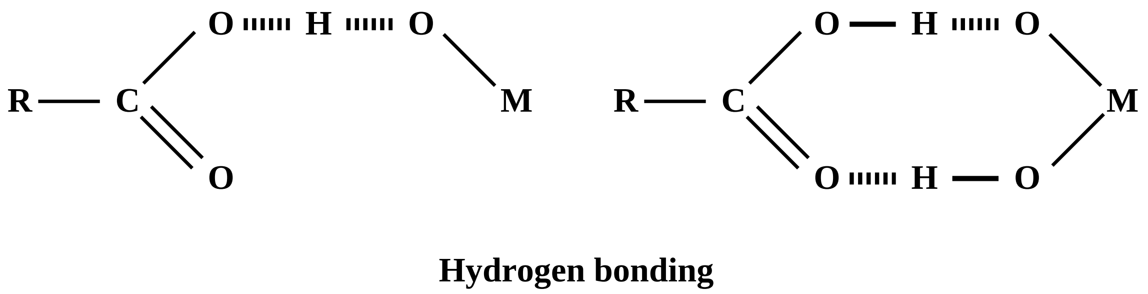

FIG. 5.1. Different types of coordination: physisorption.

5.1 Types of Coordination

The carboxy groups can coordinate in different ways to metal ions: Simply by physical adsorption via hydrogen bonding (see Fig. 5.1) or via chemical bond formation with a unidentate linkage, a bidentate (or chelating) linkage, or a bridging linkage (see Fig. 5.2). A metal ion can interact equally with the two oxygen atoms of the (COO^-) group in the bidentate form. However, this equivalence disappears in the unidentate form since the ion interacts only with one of those oxygen atoms, resulting in an ester type bond between the carboxylic acid group and the TiO_2 surface. In the bridging form, a metal ion interacts with one of the oxygen atoms, and another metal ion interacts with the second oxygen atom. When one of the ions is replaced by a hydrogen atom of a water molecule, the system is in the pseudobridging configuration.

An empirical correlation between the (COO^-) stretching frequencies of simple carboxylato complexes and the types of (COO^-) coordination has been proposed by Deacon and Phillips [96]. These authors have examined the structures and vibrational frequencies recorded for a number of acetate salts in the solid state, and proposed the following rule. When the frequency difference between the asymmetric and symmetric carboxylate bands in the adsorbed state is lower than that in the free state, the anchoring mode is either of bidentate chelation or bridging type. If the difference is greater than or equal to that in the free state, the anchoring mode is unidentate. This criterion has been frequently used to identify the carboxylate anchoring mode of ruthenium dicarboxylic complexes [7, 59, 90], although the authors of Ref. [96] mention that extrapolation of their results to more complicated systems such as dicarboxylates may be not very accurate.

Resonance Raman spectroscopy has been widely used to investigate the type of anchoring. Umapathy et al. [86] were the first to study the surface interactions of ruthenium polybipyridyl complexes with the colloidal semiconductor TiO_2 using RRS and time-resolved resonance Raman spectroscopy. They concluded that $Ru(dcbpy)_3$ adsorbs on the TiO_2 surface through the solvation layer, whereas $Ru(dcbpy)_2(H_2O)_2$ is directly physisorbed via the water ligands of the complex. RRS measurements on surfaces of

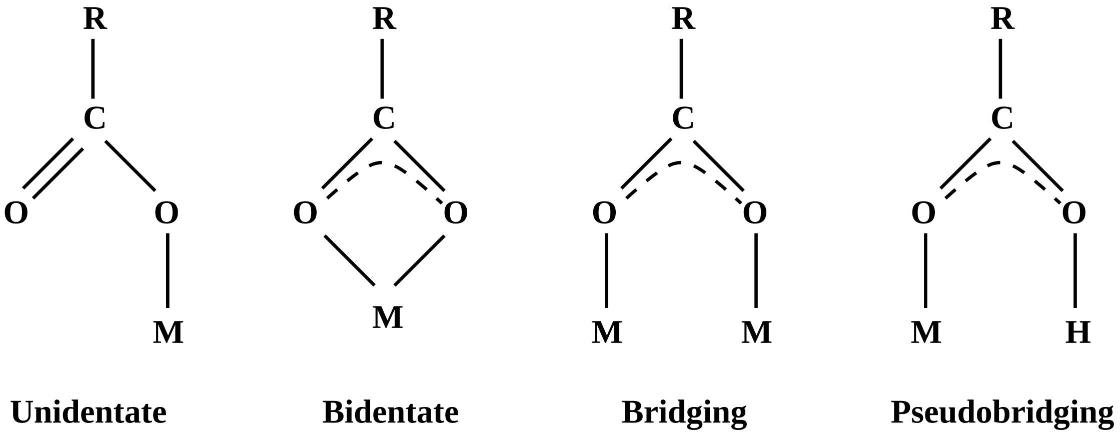

FIG. 5.2. Different types of coordination: chemisorption.

metal oxides containing Ru-bpy dyes were performed by Meyer et al. [88]. They concluded that the attachment to SnO_2, In_2O_3, and TiO_2 occurs via an ester bond, and that for SiO_2 the binding occurs in two ways, the majority by a chelating carboxylato linkage and the minority by ester formation. A recent publication of Shoute and Loppnow [94] reported that the N3 dye (the completely protonated form of N719) is adsorbed on the surface of TiO_2 nanoparticles via carboxylate bidentate or bridging bonds. The authors also concluded that the bridging type provides weak electronic coupling between N3 and the TiO_2 nanoparticle, and that the adsorption increases the absolute resonance Raman cross section of each mode and reduces the solvent reorganization energies.

Moreover, FTIR and ATR-FTIR spectroscopies are very useful to clarify the type of adsorption. The FTIR experiments of Murakoshi et al. [90] on $Ru(dcbpy)_2(NCS)_2 \cdot 2H_2O$ dye molecules adsorbed on TiO_2 nanocrystalline films supported the idea of the formation of an ester-like linkage on the strongly dye-covered TiO_2 films. The red shift in the UV-VIS spectra indicates that the formation of such strong bonds affects the electron distribution of the dye-covered TiO_2 film. Nara et al. [91] discussed the theoretical basis between the correlation of the vibrational frequencies of the carboxylate group and the types of adsorption to a divalent metal ion proposed in Ref. [96] with a molecular orbital study. It was demonstrated that such a correlation is related to changes in the CO bond lengths and the OCO angle. In Ref. [92], P. Falaras compared the FTIR data of TiO_2 powders sensitized with the mononuclear $Ru(dcbpy)_2(SCN)_2$ and the trinuclear $Ru(dcbpy)_2[\mu\text{-}(CN)Ru(CN)bpy_2]_2$ complexes which have a completely different molecular structure. The results prove that the chemical adsorption occurs via formation of ester-like linkages.

The complexes $Ru(dcbpyH_2)_2(NCS)_2$, $(Bu_4N)_2[Ru(dcbpyH)_2(NCS)_2]$, and $(Bu_4N)_4$-$[Ru(dcbpy)_2(NCS)_2]$ (also named N3, N719, and N712) adsorbed on TiO_2 have been investigated by Finnie et al. [59] with FTIR spectroscopy, and by Nazeeruddin et al. [7]

with ATR-FTIR. Finnie et al. studied the coordination of the dyes and of benzoic acid (which should show similar coordination), and concluded that the carboxylate attaches via bidentate chelate or bridging coordination to the TiO_2 surface using two carboxylic-acid groups per dye molecule. Similar results have been obtained by Nazeeruddin et al., who came to the conclusion that these dyes bind to the TiO_2 surface with two of their four carboxylic-acid groups in a bridging coordination.

5.2 Measurements of the Dyes Adsorbed on TiO_2 Paste

The preparation of the nanocrystalline titania substrates and their spectroscopic properties have been described in chapter 3. The substrates were immersed in $5{\cdot}10^{-4}$ M dye solutions. Dye coating was carried out at room temperature during 18-22 h. Thereafter, the physisorbed dye molecules were rinsed away by dipping the samples in dry ethanol. This rinsing process was repeated several times. Finally, the coated substrate was dried in air.

The dye N719 was dissolved in a mixture of acetonitrile and tert-butanol (volume ratio 1:1), forming a dark reddish-brown solution. In order to investigate the effect of the solvents on the adsorption spectra, samples with the dye dissolved in water, ethanol, or acetonitrile were prepared following the same procedure. Also, ethanol solutions of the Ru-TPA_2 dye were prepared. No solvent-dependent measurements were performed on this complex due to the lack of sufficient material.

5.2.1 UV-VIS Spectroscopy

The UV-VIS absorption spectra of both dyes adsorbed on the TiO_2 substrates are shown in Fig. 5.3. For comparison, the corresponding absorption of the substrate is also plotted. In the upper graph, the absorption spectra correspond to the dye/substrate systems, whereas in the lower panel, the contribution of the TiO_2 film has been subtracted. In Fig. 5.4, the absorption spectra of the complex N719 prepared in different solvents are presented.

It can be noticed that the electronic transitions are slightly influenced by the adsorption (see Fig. 5.3). The absorption shifts to lower energies when the complexes are attached to the semiconductor surface, in particular for the dye Ru-TPA_2. A similar effect was reported in Ref. [90] for $Ru(dcbpy)_2(NCS)_2$, where the band shifts were ascribed to the interaction between the dye molecule and the TiO_2 surface through the carboxylic groups. However, this behavior is contrary to that reported in Ref. [58]: The dye N3 (the completely protonated form of N719), when adsorbed on TiO_2 in DMSO solution,

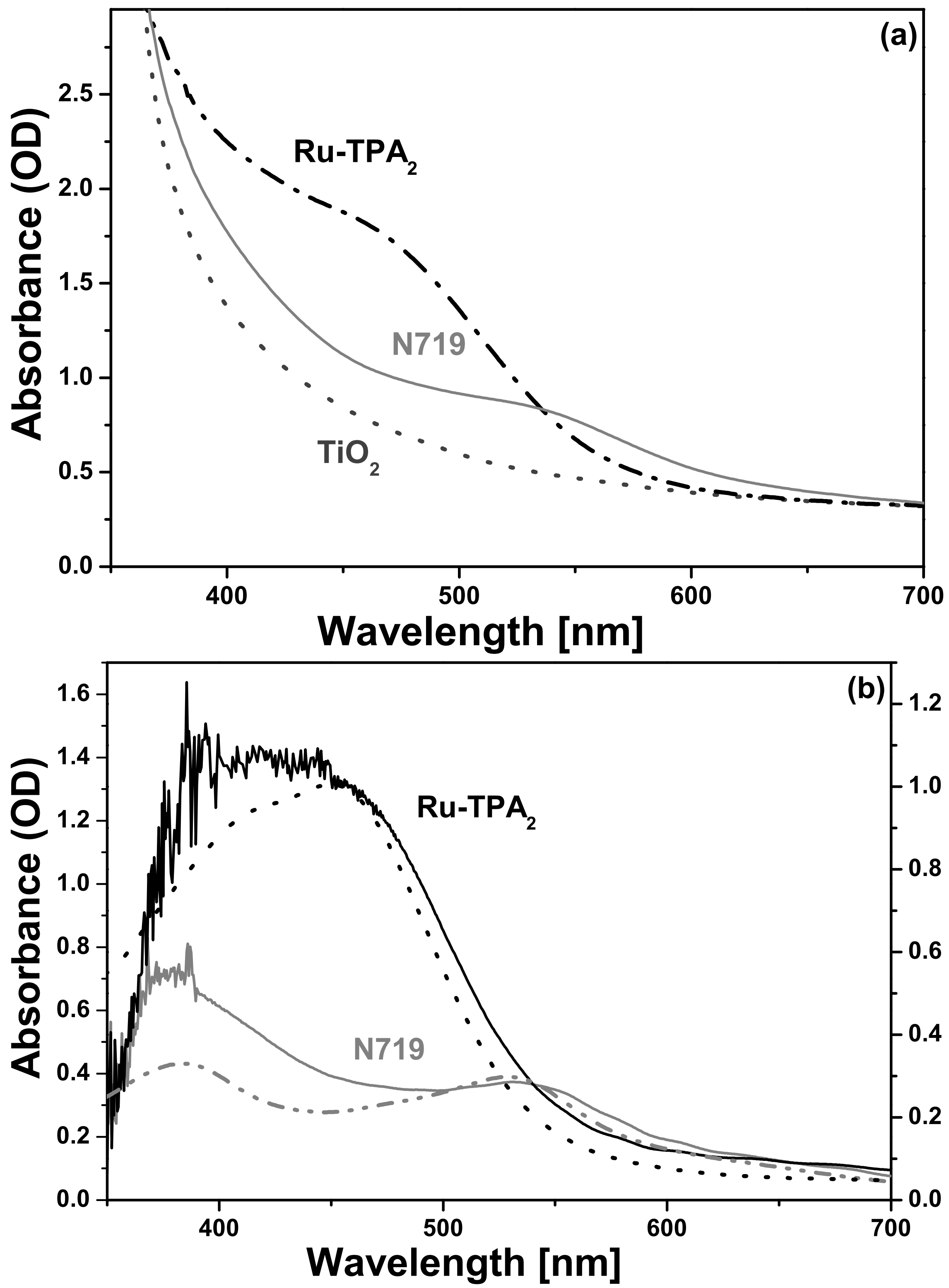

FIG. 5.3. Absorption spectra of the Ru-dyes adsorbed on TiO$_2$ paste films. The solid curves in part **(b)** represent the same data as in part **(a)**, but with the TiO$_2$ spectrum subtracted. In part **(b)**, the spectra of N719 dissolved in acetonitrile and Ru-TPA$_2$ in ethanol are shown for comparison (dash-dotted and dotted line, respectively).

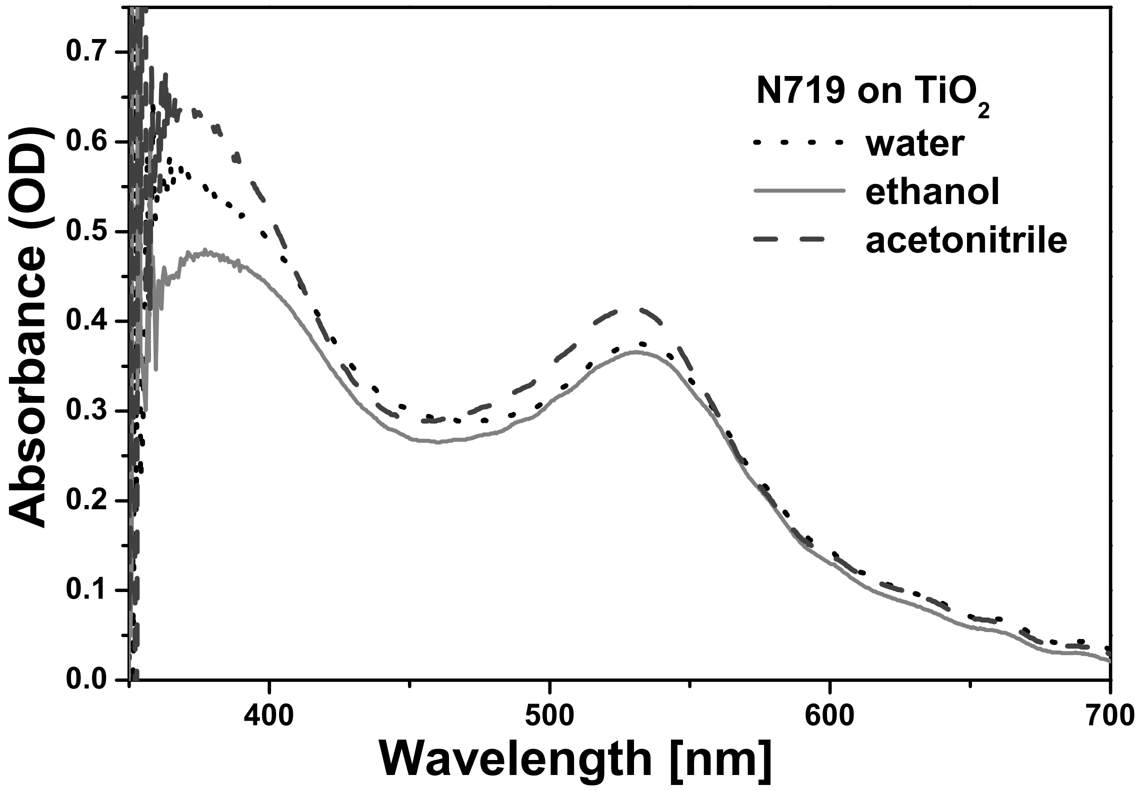

FIG. 5.4. Absorption spectra of N719 adsorbed on TiO_2 paste prepared in different solvents.

slightly shifted its absorption bands to higher energies. The spectra of N719 adsorbed on the titania film show only small differences when prepared in different solvents.

5.2.2 Raman Spectroscopy of N719

Raman spectra with 632.8 nm excitation wavelength

It was already discussed in chapter 3 that the normal Raman spectrum of N719 powder could not be measured with the red laser due to strong fluorescence. However, when the dye is adsorbed on the TiO_2 substrate, weak lines can be observed (see Fig. 5.5). This strong quenching of the fluorescence and the concomitant signal enhancement can be ascribed to surface-enhanced Raman effects. SERS effects of molecules adsorbed on semiconductor surfaces have been reported in the literature [18, 19]. Hugot-Le Goff, Falaras, and co-workers described a similar effect in ruthenium polypyridyl complexes adsorbed on TiO_2 [2, 69, 87, 89]. Nevertheless, the authors could not separate the resonance effects due to the excitation wavelength of the investigated dyes from the SERS contribution, concluding that the signals were affected by SERRS effects. Hence, this is the first time that the Raman spectrum of Ru-bpy dyes adsorbed on TiO_2 is

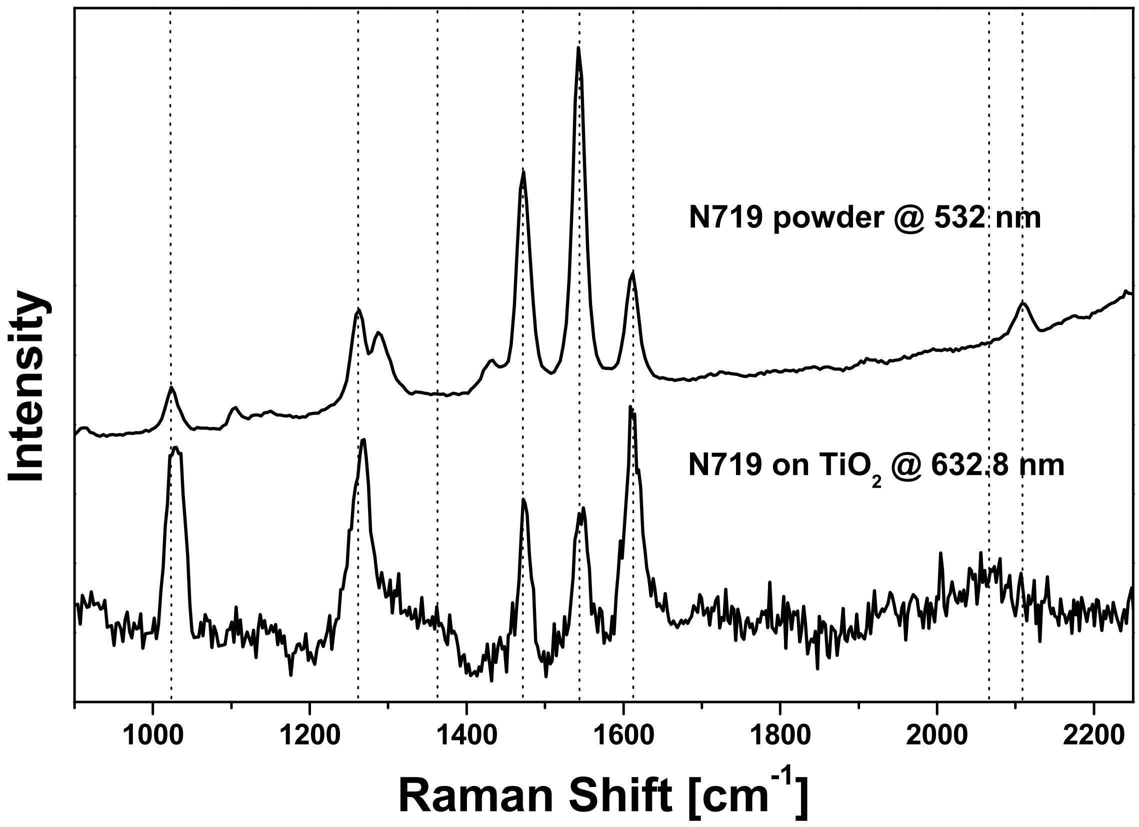

FIG. 5.5. Raman spectra of N719.

obtained without the resonance condition, only by means of SERS enhancement. The usual two mechanisms of SERS seem to be present: First, the e.m. enhancement produced by the nanostructured titania film, and second, the chemical enhancement or charge-transfer between the dye and the substrate. The latter is very important for the working principle of solar cells.

The spectrum presented in Fig. 5.5 (bottom) is the result of 300 spectral accumulations, each with 1 s integration time, after having subtracted the fluorescence background, (see below). A very weak, broad and blue-shifted ν(C=N) line of NCS appears at ~2080 cm^{-1}. The low intensity of this vibration indicates that the NCS ligand is not directly involved in the adsorption, but the large blue shift of its position shows that structural changes in the dye occur upon adsorption affecting this mode. When the dye is attached to metallic nanoparticles (see chapter 4) through this moiety, the ν(C=N) line is strong and largely red-shifted. However, in Ref. [58] it was reported for the dye N3 (the completely protonated form of N719) that the bands of thiocyanate were unaffected since they did not participate in the binding. These differences can be ascribed to differences of the systems: Here, a TiO_2 film and the dye N719; in Ref. [58], an aqueous/DMSO colloidal TiO_2 solution and the complex N3. The adsorption seems to be stronger in the first case, as was already observed by comparing the UV-VIS

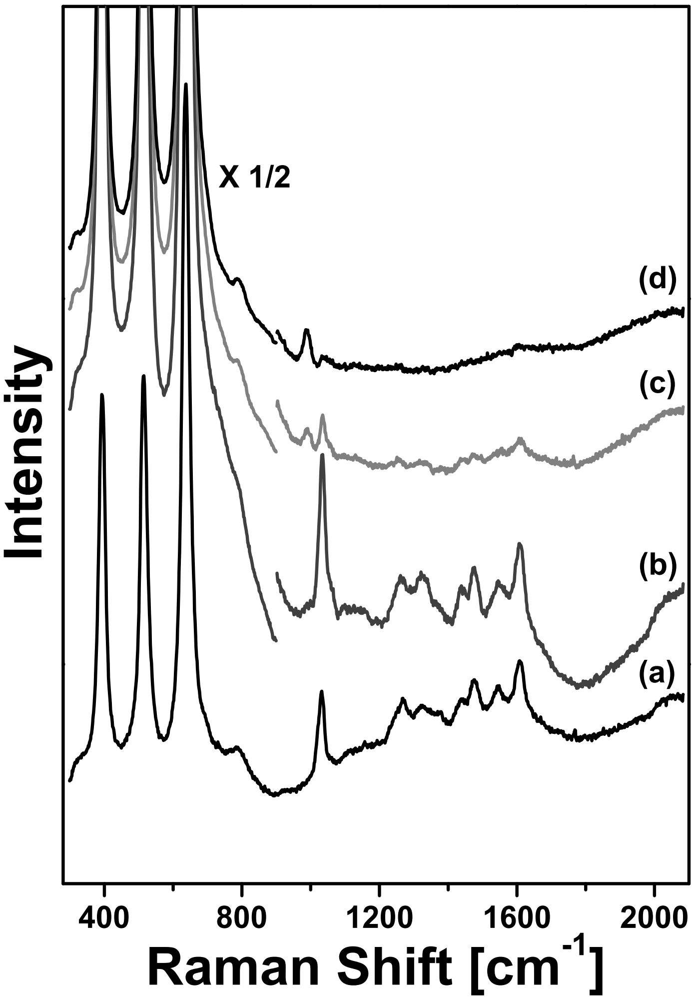

FIG. 5.6. Temporal sequence of Raman spectra of the dye N719 adsorbed on TiO_2 paste excited at 632.8 nm. Spectra **(b)**,**(c)**,**(d)** were recorded with 3× higher laser power as compared with spectrum **(a)**. In spectra **(b)**,**(c)**,**(d)** the Raman signals below 820 cm^{-1} have been divided by two and shifted vertically for better visibility.

absorption spectra (see the previous subsection).

The stretching modes and the ring breathing of the bipyridine are slightly shifted in comparison to the RRS spectrum, and the relative intensity is determined by the SERS effect rather than by resonance (compare with the results on Ag and Au in chapter 4). No ν(C=O) vibration appears in the spectrum. On the other hand, a shoulder shows up around 1370-1380 cm^{-1}, but it cannot be well resolved. This band is assigned to $\nu_{sym}(COO^-)$. Moreover, the C-C ring and C-O stretching modes in the 1250-1350 cm^{-1} region are strongly affected by adsorption and SERS effects. The line at 1265 cm^{-1} shifts to higher frequencies and increases in intensity, whereas the one at 1287 cm^{-1} almost disappears. The facts that no ν(C=O) vibration is present, the ν(C-O) modes region is strongly altered, and the appearance of the $\nu_{sym}(COO^-)$ vibration, indicate that the coordination of the carboxy ligands to the TiO_2 occurs via bidentate or bridging bonds (see Fig. 5.2).

It was mentioned before that there is a broad background signal underneath the vibrational bands, hence, the fluorescence is not quenched completely by the adsorption. This is probably due to a residual amount of unadsorbed molecules. The background slowly disappears under laser irradiation, and simultaneously Raman lines of the complex show up. With prolonged irradiation time the signal is affected undergoing structural transformations, until the dye is completely damaged and its lines disappear (see Fig. 5.6). In Ref. [2] it was reported that the surface of dye-sensitized electrodes was rapidly damaged if an electron donor was not added to the solution. In the present study, the Raman spectra are affected by the lack of a hole transport layer or an electrolyte for reducing the oxidized dye molecules, and also by thermal degradation of the sample due to high laser powers. Other parameters have to be optimized for recording a spectrum as well. For example, using a small-magnification objective, even with a high numerical aperture (NA), the strong fluorescence will prevent any successful measurement. On the other hand, if a high-magnification and high-NA objective is used, the sample can easily be damaged, since the laser beam will be focused in a very tiny spot. Hence, the presented spectra were recorded with very low laser power. This is the reason for the low quality of the obtained spectra, which in addition, have to be recorded at the same spot of the sample in order to bleach the fluorescence background, at least to some extent. Therefore, it was not possible to accumulate the signal of different points to avoid overheating, as it was done in previous measurements.

It is worthwhile noticing that very strong Raman lines corresponding to the TiO_2 substrate can be observed. When the irradiation intensity is increased, also the vibrations of the titania are affected (see Fig. 5.6, (b)). When the dye is completely damaged and its signal disappears, the lines of the semiconductor recover their original structure (see Fig. 5.6,(d)). This is consistent with strong adsorption of the dye on the semiconductor surface, since in the absence of the adsorbate the TiO_2 is not affected by the laser irradiation, as it was reported in chapter 3. Charge-transfer between the dye and the semiconductor surface is photoinduced by the excitation beam. The transfer of electrons influences the electronic levels of the TiO_2, and under high intensities, this shows up as a change of the Raman lines. Finally, when the dye is completely degraded and does not show any signal, no charge-transfer can take place, and the semiconductor Raman bands return to their original state.

In order to investigate the effect of the solvents on the adsorption of the dyes on the semiconductor, substrates with aqueous, ethanolic and acetonitrile solutions of N719 have been prepared, and their Raman spectra recorded. The results do not show any noticeable difference; hence, there is no indication of different anchoring configurations.

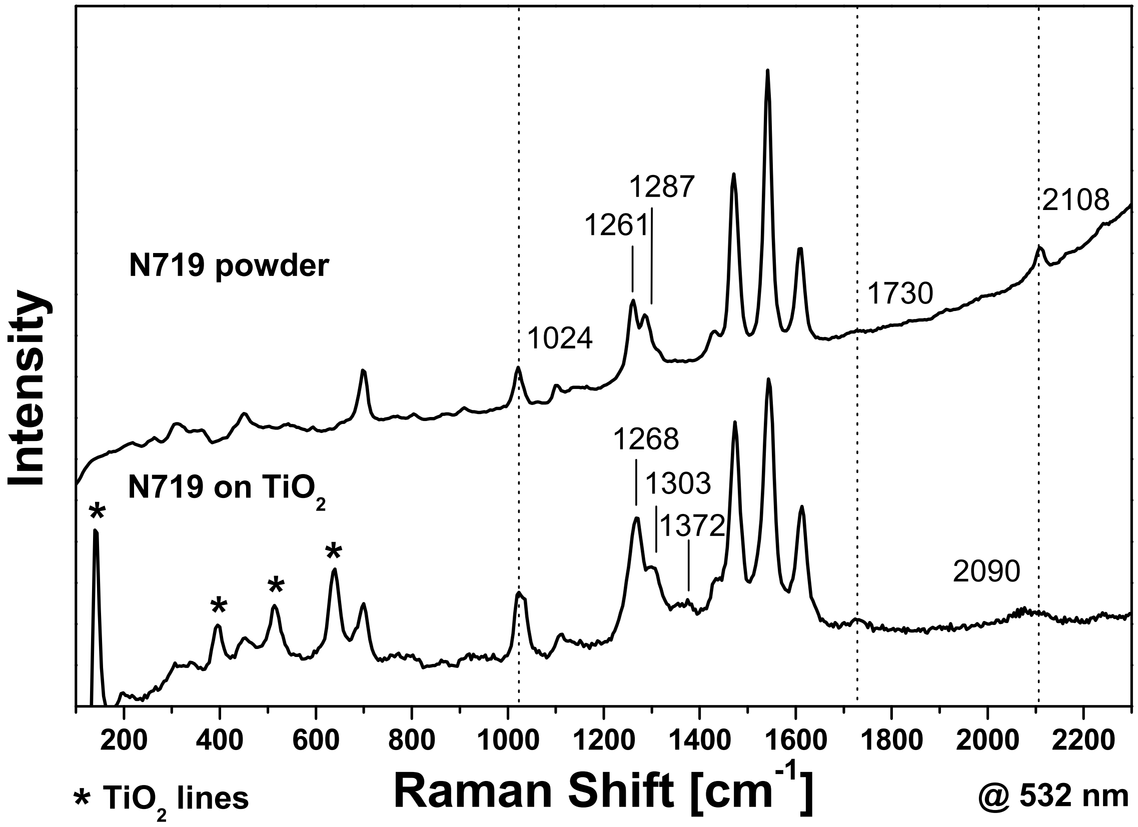

FIG. 5.7. Raman spectra of N719 excited at 532 nm.

Raman spectra with 532 nm excitation wavelength

New measurements have been conducted with the green laser, whose photon energy matches the lower-energy absorption band of the dye and of the dye/substrate system. Thus, at 532 nm also resonance effects are involved, which allows us to reduce the laser intensities for recording a spectrum. In these samples a good signal to-noise-ratio is obtained due to the SERRS enhancement (resonance effect, in addition to the SERS produced by the TiO_2 substrate). The spectra were recorded accumulating the signal at different points in order to avoid overheating. One disadvantage of the presence of resonance effects is that both the adsorbed and the non-adsorbed molecules contribute to the resulting spectra. It is obvious that the spectra of the adsorbed molecules are also enhanced by SERS effects, hence appearing with stronger intensity, however, also some amount of non-adsorbed molecules may be present on the surface and contribute to the spectrum.

The SERRS spectrum of N719 adsorbed on the TiO_2 film is shown in Fig. 5.7 (bottom). A weak thiocyanate band appears at ~2090 cm^{-1}. This line is blue-shifted as compared to the RRS spectrum indicating that structural changes of the dye occur upon adsorption affecting this mode, as it has already been observed with the red

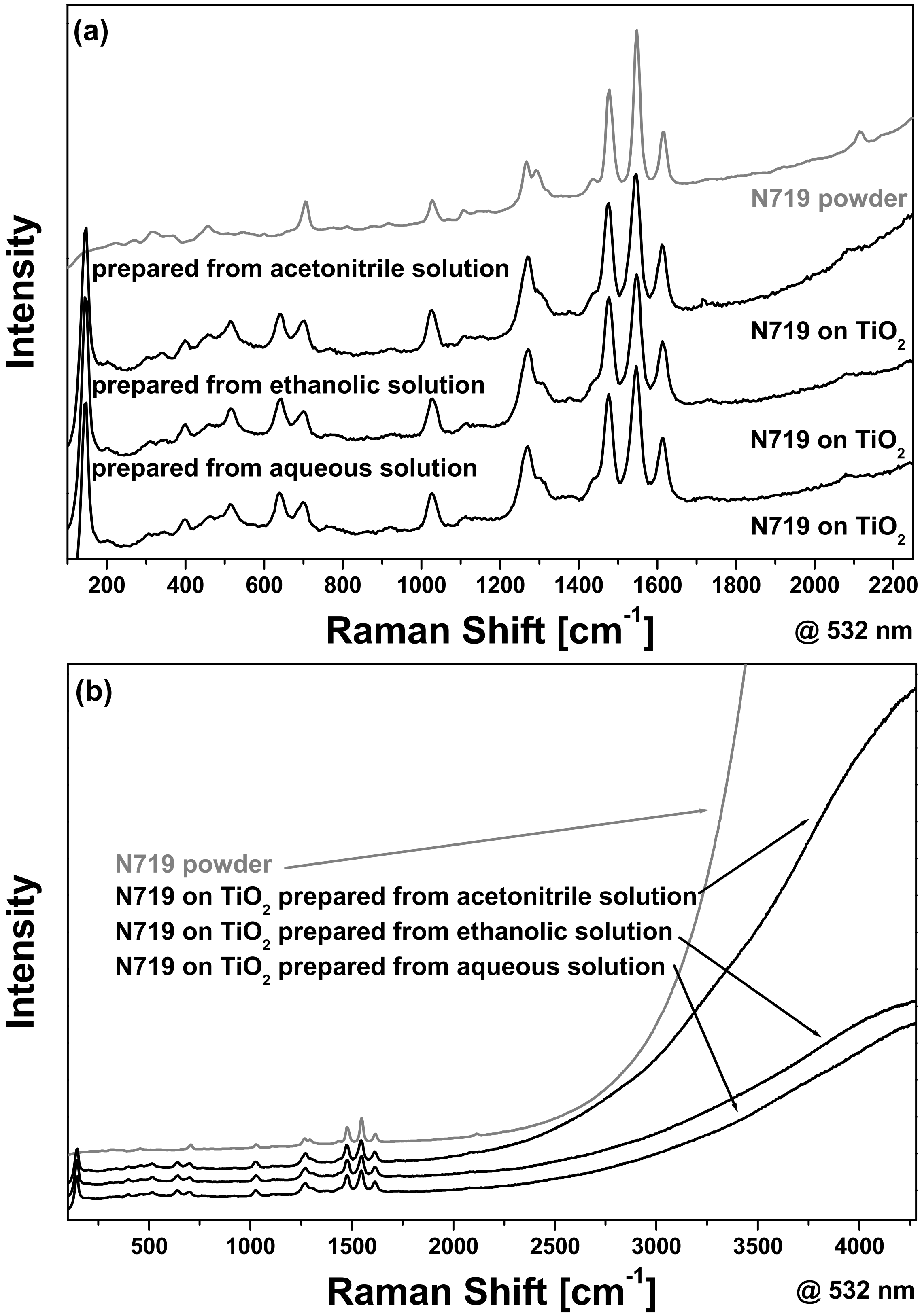

FIG. 5.8. Raman spectra of N719 adsorbed on TiO2 paste excited at 532 nm. Part **(b)** shows the signals in a broader spectral range.

laser. The relative intensity of the bipyridine vibrations in the 1400-1600 cm^{-1} region is determined by the resonance effect. The ν(C=O) does not seem to change with the adsorption. A new weak band, assigned to $\nu_{sym}(COO^-)$, appears at 1372 cm^{-1}. The relative intensity and the position of the lines corresponding to C-C ring and C-O stretching modes in the 1250-1350 cm^{-1} region are strongly affected by adsorption. The bpy ring breathing exhibits an enhancement in comparison with the RRS owing to SERS. The results at this irradiation wavelength are consistent with those obtained with the red laser, confirming that the coordination of the carboxy ligands to the TiO_2 occurs via bidentate or bridging bonds. The presence of the C=O stretching mode can be explained by the contribution of the non-adsorbed molecules to the spectrum. Another plausible interpretation is that the free ligands can also contribute since the complex is not attached to the surface through the four carboxy ligands for steric reasons [7, 59]. These free carboxylic-acids groups can eventually form H-bonds with the surface (see Fig. 5.1). Similar conclusions were reported in Ref. [58] for the dye N3.

Weak TiO_2 lines are observed in the SERRS spectrum (see Fig. 5.7). The complete absence of these bands has been reported in previous studies [2,58,94]. Hugot-Le Goff et al. performed voltage-dependent studies on dye-sensitized titania electrodes in acetate buffer with an electron donor. The authors explained that at certain electrostatic potentials, the surface charge of the TiO_2 is so strong that the semiconducting nature of the material is lost and the interface layers obtain a metallic character, thus quenching the anatase bands. In the present study, a similar effect takes place at the semiconductor surface: Under resonant irradiation, the dye is very efficiently excited and a large amount of electrons is promoted to the TiO_2 conduction band. Hence, the surface charge increases strongly and the substrate loses, at least to some degree, its semiconducting nature. Since in the present system no hole acceptor is present, the accumulating charge is limited and the bands of the titania still appear but with low intensity.

As was already observed with the red laser, after intense irradiation the dye is affected by the illumination. First, the relative intensity of the TiO_2 bands increases with respect those lines of the dye. Under prolongated and high irradiation the dye is damaged, so the injection of charges to the semiconductor decreases, and the TiO_2 recovers its semiconducting nature and shows strong Raman lines. Finally, the same degradation process as with the red laser takes place. The dye signal disappears, and the TiO_2 Raman lines return to their normal state.

Small differences appear between the spectra of the complex adsorbed on TiO_2 prepared in different solvents, see Fig. 5.8. A slightly more intense $\nu_{sym}(COO^-)$ line seems to be present in the spectrum of the dye prepared in water, and the strength of the remaining luminescence is stronger in the acetonitrile sample than in the others. The luminescence at ~750 nm is strongly quenched by the adsorption, but still a small, residual signal remains. In Ref. [58], the authors ascribe it to the non-adsorbed molecules. According to this argument, it can be concluded that when the dye is prepared in acetonitrile the molecules have a slightly smaller affinity to the semiconductor film, although the UV-VIS spectrum corresponding to this solvent shows a higher absorption (see Fig. 5.4).

5.2.3 ATR-FTIR Spectroscopy of N719

In order to complement the results obtained with Raman spectroscopy at two different excitation wavelengths, FTIR spectra of the complex adsorbed on the TiO_2 substrate have been recorded as well. The FTIR spectra of N719 powder have already been characterized in chapter 3. Owing to high absorption and scattering of light on the titania film/glass surface, the normal FTIR spectroscopy cannot be performed, and attenuated total reflection (ATR) spectroscopy has to be used. The fundamentals and the experimental setup of ATR-FTIR were described in chapter 2.

The FTIR spectra were measured using a Bio-Rad Digilab FTS 40 FTIR spectrometer equipped with an ATR accessory plugged directly into the same spectrometer. Typically 100 scans were averaged at a resolution of 4 cm^{-1}. The IR optical path was flushed with dry air. The FTIR spectra of the anchored dyes were obtained by subtracting the IR spectrum of the blank TiO_2 films from the spectrum of the dye-coated films of the same thickness. For comparison, the spectrum of the pure dye was also recorded with this technique. The complex N719 was dissolved in ethanol and layer by layer was deposited on a glass substrate. When the solvent had evaporated, a film of dye powder remained on the glass. The glass substrates were previously treated with a sulfochromic acid solution to improve the adsorption of the sample.

The spectra of the dye N719 in powder state and adsorbed on the TiO_2 substrate are compared in Fig. 5.9. From the observation of the signals, it can be concluded that the complex is strongly affected by the adsorption. Unfortunately, no rigorous quantitative analysis of the spectra can be performed, but for comparison of various peak intensities the intensity of the bipyridine ν(C=C) mode at 1542 cm^{-1} has been used as an internal standard.

First, the differences between the normal FTIR spectrum of the dye measured in a KBr pellet, and the ATR-FTIR signal will be discussed. In the reflection spectrum only one ν(C=O) mode can be observed shifted to lower frequencies (around 1702 cm^{-1}), whereas the $\nu_{sym}(COO^-)$ and $\nu_{asym}(COO^-)$ bands are split, each one appearing as two peaks instead of one. The band at 1237 cm^{-1}, ascribed to ν(C-O), slightly shifts to lower wavenumbers and increases in intensity. The preparation of the powder film, for which the dye is dissolved in ethanol, can influence the state of the carboxy groups, producing differences between this spectrum and the one recorded in KBr pellets. Small variations in the relative intensity of other bands can also be observed.

In the spectrum of the adsorbed dye, more pronounced changes occur in the lines

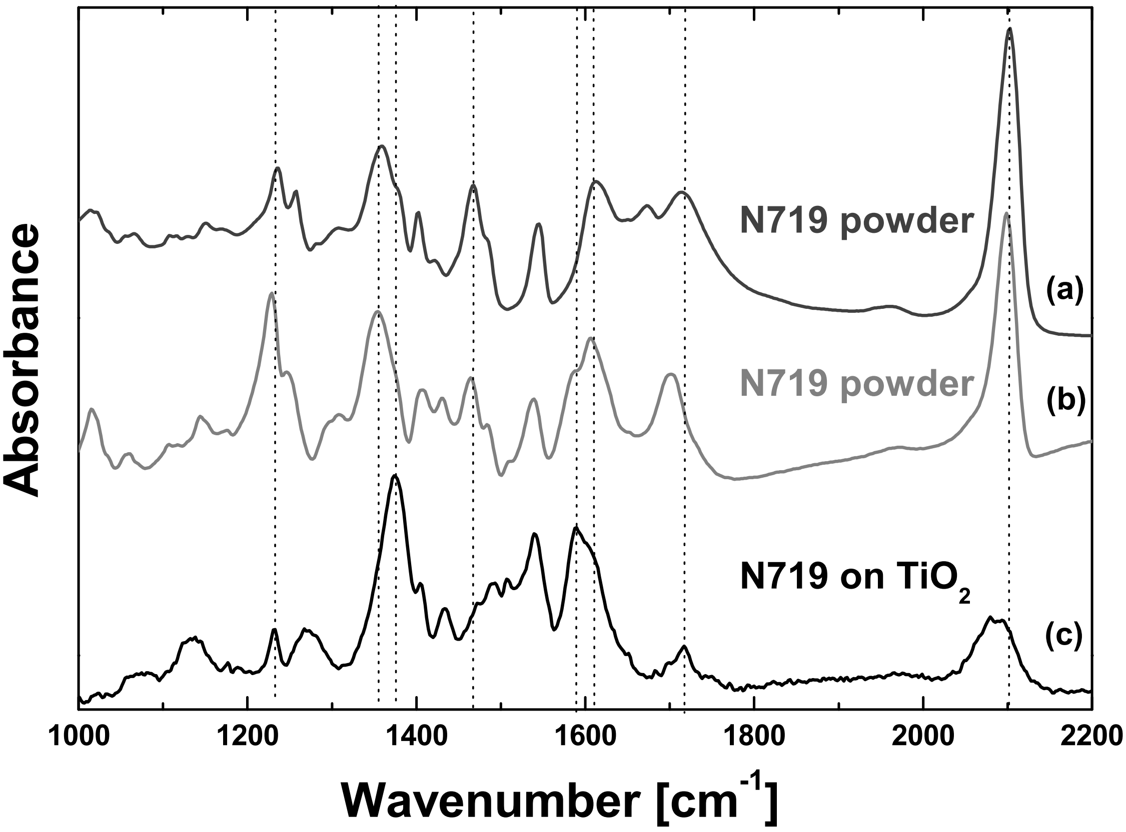

FIG. 5.9. FTIR spectra of N719 adsorbed on TiO_2 paste compared with the signals of the dye powder: **(a)** normal FTIR, **(b)** and **(c)** ATR-FTIR.

corresponding to the carboxy groups. A very weak ν(C=O) line can be observed at 1715 cm^{-1}, the ν(C-O) at 1237 cm^{-1} decreases in intensity, and the ν(COO^{-}) signals strongly increase. Since the modes of the non-equivalent oxygens are strongly attenuated by the adsorption and the carboxylate bands turn out to dominate the spectrum, it can be concluded that the anchoring occurs via bridging or bidentate linkage. These results are in agreement with those obtained from the Raman measurements. The presence of the signals of the protonated form can again be ascribed to contributions of non-adsorbed molecules, or simply to the signal of non-bound carboxy groups, since for steric reasons not all these groups are involved in the anchoring process. It was illustrated in the introduction that several research groups have used the difference between the symmetric and asymmetric bands of the dyes in the free and adsorbed state as criterion. In the N719 salt the carboxylate vibrations appear at 1354 and 1606 cm^{-1}, the difference being 252 cm^{-1}. In the adsorbed state they are located at 1375 and 1602 cm^{-1}, 227 cm^{-1} apart, which is consistent with the bridging or bidentate coordination. Similar conclusions for the same dye and similar compounds have been reported in the literature, as was already mentioned in the introduction [7,59,90,91,93]. In Ref. [93] it is proposed that minor wavenumber shifts in the carboxylate stretching modes upon adsorption indicate bridging coordination. Since in the present study the shifts are more pronounced, the binding type seems to be bidentate chelating.

Another important difference is that the intensity of the band at ~1470 cm^{-1} ascribed to the TBA counterion decreases strongly when the complex is attached to the TiO_2. When the dye is in solution, the counterions are separated from the carboxylates. Since adsorption takes place through the COO^- and COOH moieties, part of these groups attach to the surface. When the substrates are rinsed after preparation, the counterions are expected to remain in the solvent and be washed away.

The band of the thiocyanate appears much weaker and slightly blue-shifted. The shift to lower wavenumbers was already observed with Raman and RRS spectroscopy and was ascribed to changes in the dye upon adsorption. The low intensity can either result from degradation of the dye (see appendix A) or from a change in the dipole moment owing to a different deprotonation state of the complex when it is adsorbed on the semiconductor [7].

The ATR-FTIR spectra of N719 on TiO_2 paste films prepared in different solvents were compared with the absorption bands of the powder complex. (The spectra are not shown). Big differences do not appear, and in the three cases the dye seems to attach to the surface via bridging or bidentate coordination.

5.2.4 Raman Spectroscopy of Ru-TPA_2

Excitation wavelength, 632.8 nm

The spectrum of Ru-TPA_2 adsorbed on TiO_2 recorded with the red laser is shown in Fig. 5.10. The quality of the signal is very poor due to the presence of strong fluorescence. Under continued irradiation, the lines of the dye are affected very fast, first undergoing structural transformations, then disappearing from the spectrum. It is evident that no lines corresponding to carboxy groups can be observed, neither in their protonated form, nor as deprotonated carboxylates. The Raman line at ~1630 cm^{-1} associated with the ν(C=C) of the C-H chain in trans configuration which binds the TPA to the bipyridine appears as a shoulder of the band at 1606 cm^{-1} and it is less well defined than in the powder signal. The rest of the bands are deformed by the fluorescence background, which makes a further discussion almost impossible.

It is worthwhile mentioning that strong Raman lines of the titania are present in the spectrum. Similar as was described in the case of the dye N719 adsorbed on the TiO_2 film, the titania lines are also affected by high and/or long irradiation, and when the signal of the anchored complex disappears, they recover their original structure.

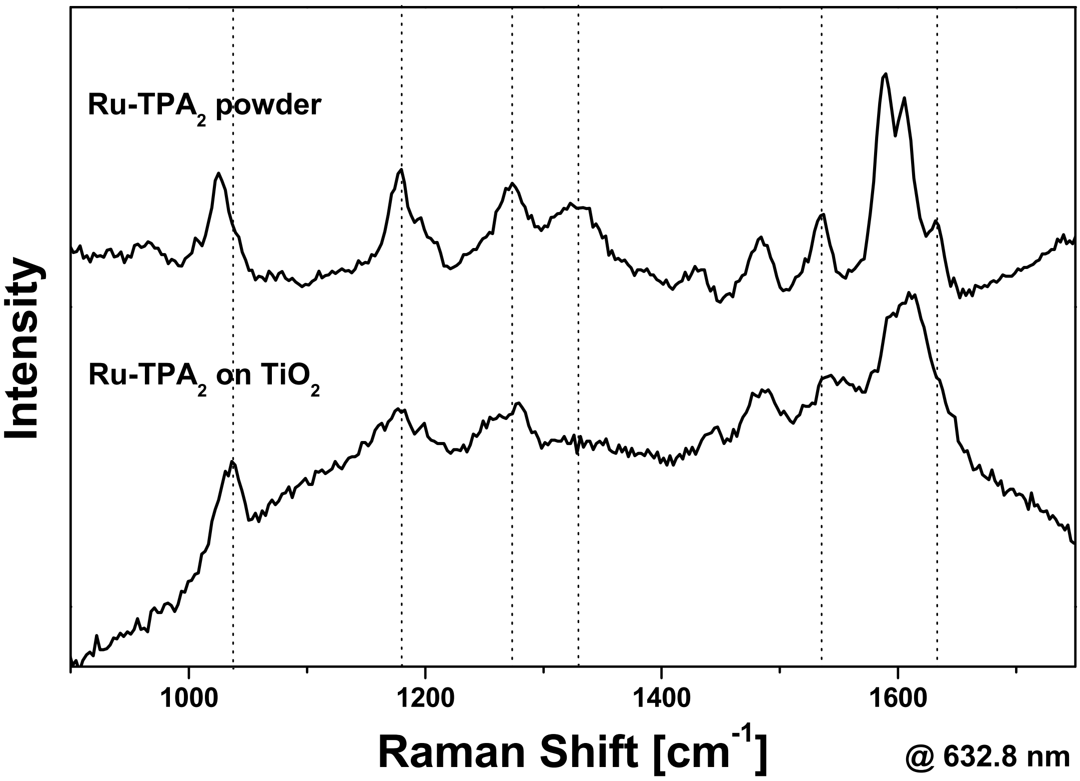

FIG. 5.10. Raman spectra of Ru-TPA_2 excited at 632.8 nm.

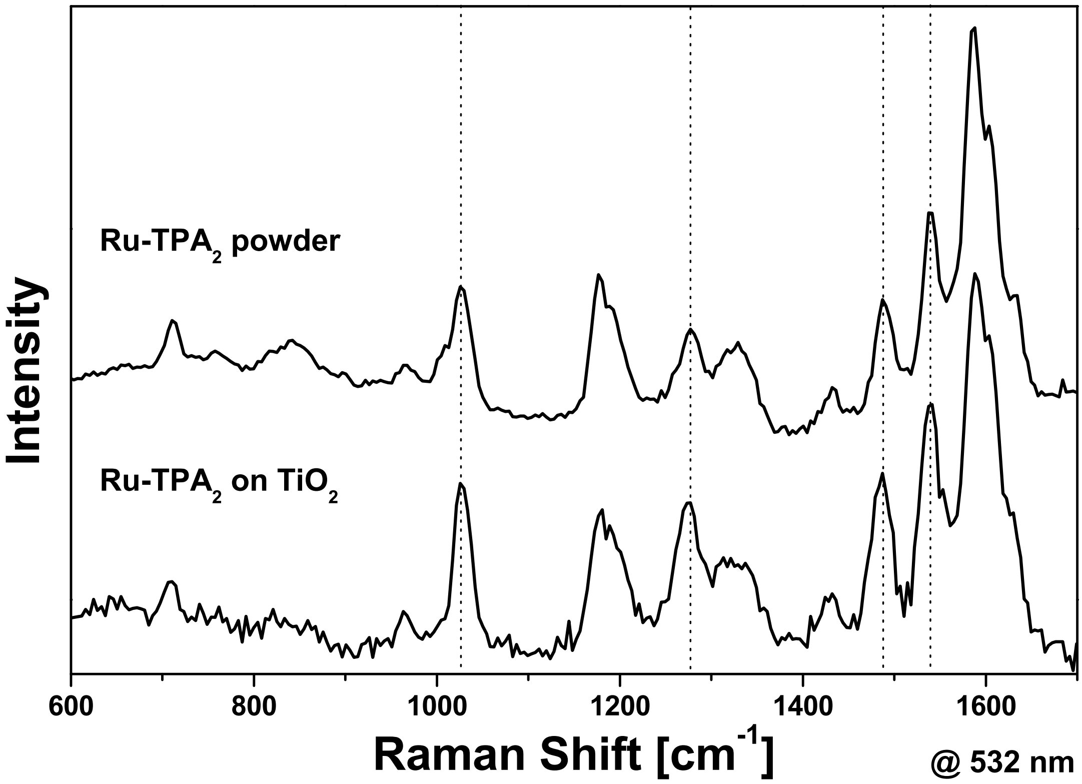

FIG. 5.11. Raman spectra of Ru-TPA_2 excited at 532 nm.

Excitation wavelength, 532 nm

With the green excitation, a spectrum of good quality can be recorded, since the fluorescence is partly quenched. This improvement can also be due to preresonance effects at this wavelength, as was previously discussed in chapters 3 and 4. To avoid overheating and other light-induced processes, the signal of different spots on the sample was accumulated to yield the final spectrum.

Comparing the Raman lines of Ru-TPA_2 adsorbed on the TiO_2 substrate with the powder signal, small differences can be found (see Fig. 5.11). The lines corresponding to the bipyridine, such as the ν(C=C) and ν(C=N) at 1537 and 1490 cm^{-1}, respectively, and the ring breathing band at 1024 cm^{-1} appear to be stronger in the adsorbed state. The band at 1273 cm^{-1}, ascribed to the C-N stretching mode and C-H deformation, also increases in intensity. These changes can be explained by a change in the configuration and in the electronic structure of the dye upon adsorption; they are enhanced by stronger preresonance effects. No signal of the linking part of the molecule appears, so no conclusion can be drawn in this respect. As it was mentioned above for the red laser, the C=C stretching band of the alkene group at $\sim$1630 cm^{-1} is not so well defined as in the powder signal, but appears as a shoulder.

The lines of the substrate were very weak in the SERRS spectrum of N719 adsorbed on TiO_2 as discussed in the previous section, but in the present case, no lines can be observed at all. This behavior can be interpreted as the result of two main contributions: First, the titania lines overlap with the fluorescence background accompanying the dye signal, and second, the semiconducting nature of the TiO_2 is largely lost, due to the high photoinduced charge on its surface. This second argument implies a strong binding of the complex to the semiconductor, since efficient electronic injection seems to occur from the former to the latter.

5.2.5 ATR-FTIR Spectroscopy of Ru-TPA_2

The FTIR and the ATR-FTIR spectra of the complex Ru-TPA_2, in powder form and adsorbed on the TiO_2 film, have been also recorded (see Fig. 5.12). The experimental procedure was the same as described in section 5.2.3. From the spectra it is clear that the conformation of the dye Ru-TPA_2 changes upon adsorption.

Comparing the FTIR and the ATR-FTIR signals of the powder, only minor differences can be noticed. The band of the ν(C=O) at 1726 cm^{-1} appears slightly stronger, the peak at 1426 cm^{-1}, ascribed to a ν(C=N) of the bipyridine becomes broader and stronger, and the relative intensities of some other lines vary also.

In the spectrum of the adsorbed dye, strong symmetric and asymmetric $\nu(COO^-)$ lines show up. The $\nu_{sym}(COO^-)$ appears at 1379 cm^{-1}, whereas the line of the asymmetric vibration is overlapped by the strong C=C stretching band of the aromatic rings. From

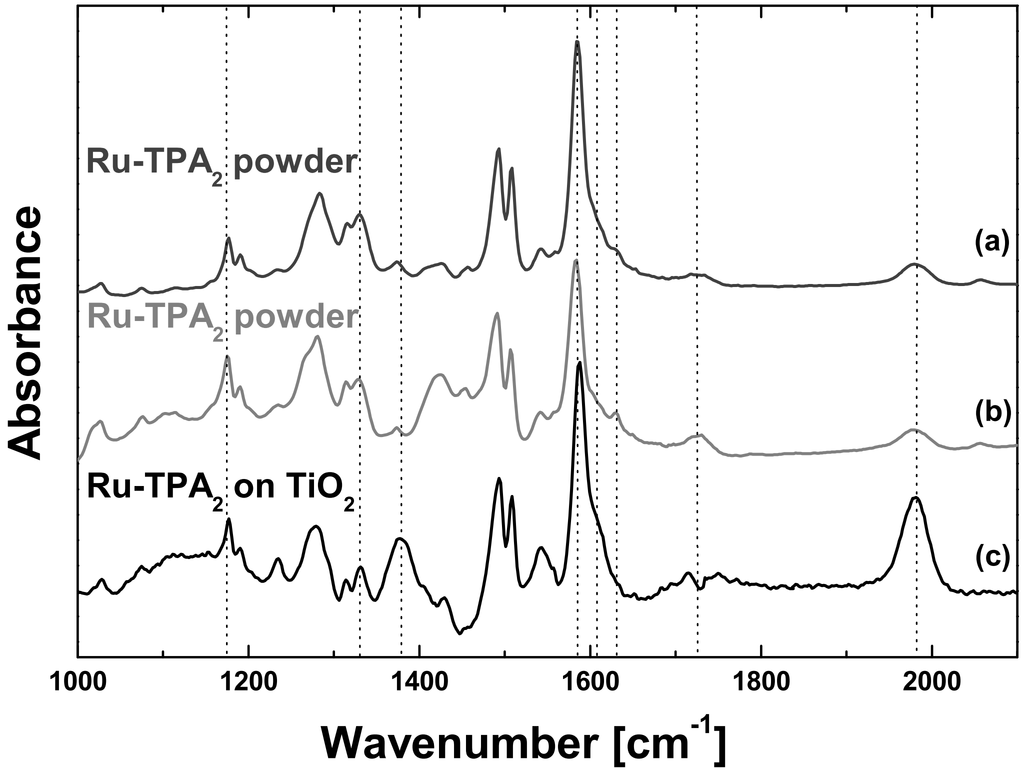

FIG. 5.12. FTIR spectra of Ru-TPA$_2$ adsorbed on TiO$_2$ paste as compared with the signals of the dye powder: **(a)** normal FTIR, **(b)** and **(c)** ATR-FTIR.

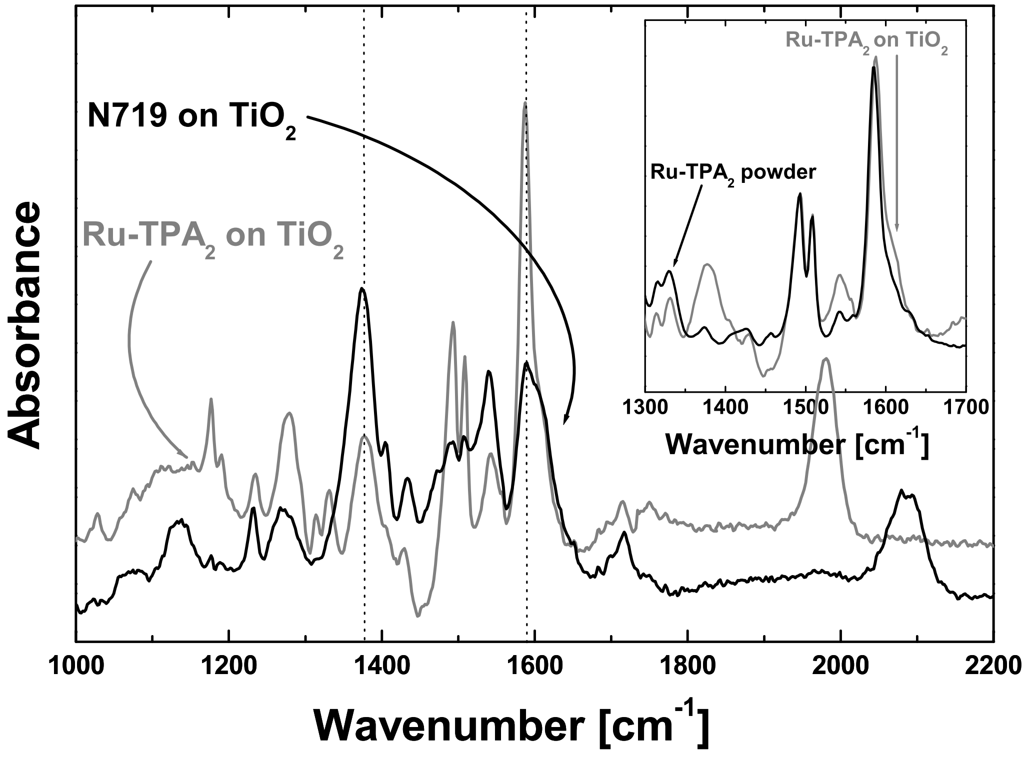

FIG. 5.13. ATR-FTIR spectra of Ru-TPA$_2$ and N719 adsorbed on TiO$_2$ paste. In the inset, the signal of Ru-TPA$_2$ adsorbed on TiO$_2$ paste is compared with the FTIR powder spectrum of the dye.

the superposition of the spectra of the two adsorbed dyes, in Fig. 5.13, the position of this band can be estimated. Unfortunately, the frequency of the stretching modes of the deprotonated carboxy groups of the Ru-TPA_2 in ionic state is not known, and the criterion used previously which involves the energy difference between the symmetric and asymmetric bands of the dyes in the free and the adsorbed state cannot be used. However, the presence of a very weak C=O stretching mode and the appearance of the strong carboxylate stretching bands strongly support the idea that the adsorption must occur via bridging or bidentate linkage, as in the case of N719.

Further changes occur in the signals of the adsorbed complex. The band at 1540 cm^{-1}, ascribed to the C=C stretching of the bipyridine, increases in intensity as compared to the powder spectra. Moreover, the ν(C=C) band of the alkene group at $\sim$1630 cm^{-1} becomes weaker and more as a shoulder than an independent band. This effect was also observed in the Raman spectra and can be ascribed to a conformational change of the molecule upon adsorption.

5.3 Measurements of the Dyes Adsorbed on TiO_2 Powder

The efficiency of the spectral sensitization of TiO_2 films depends not only on the type of the dye adsorption, but also on the morphology of the semiconductor surface [90]. Hence, for comparison with the previous results in TiO_2 paste films, in this section the adsorption of the complexes N719 and Ru-TPA_2 on anatase nanopowder is investigated with FTIR spectroscopy in KBr pellets. The dyes and the anatase powder were already characterized with Raman and FTIR spectroscopies in chapter 3. The sensitization

FIG. 5.14. Colloidal ethanolic solutions of the dyes and TiO_2 under stirring. The left picture corresponds to N719, the right one to Ru-TPA_2.

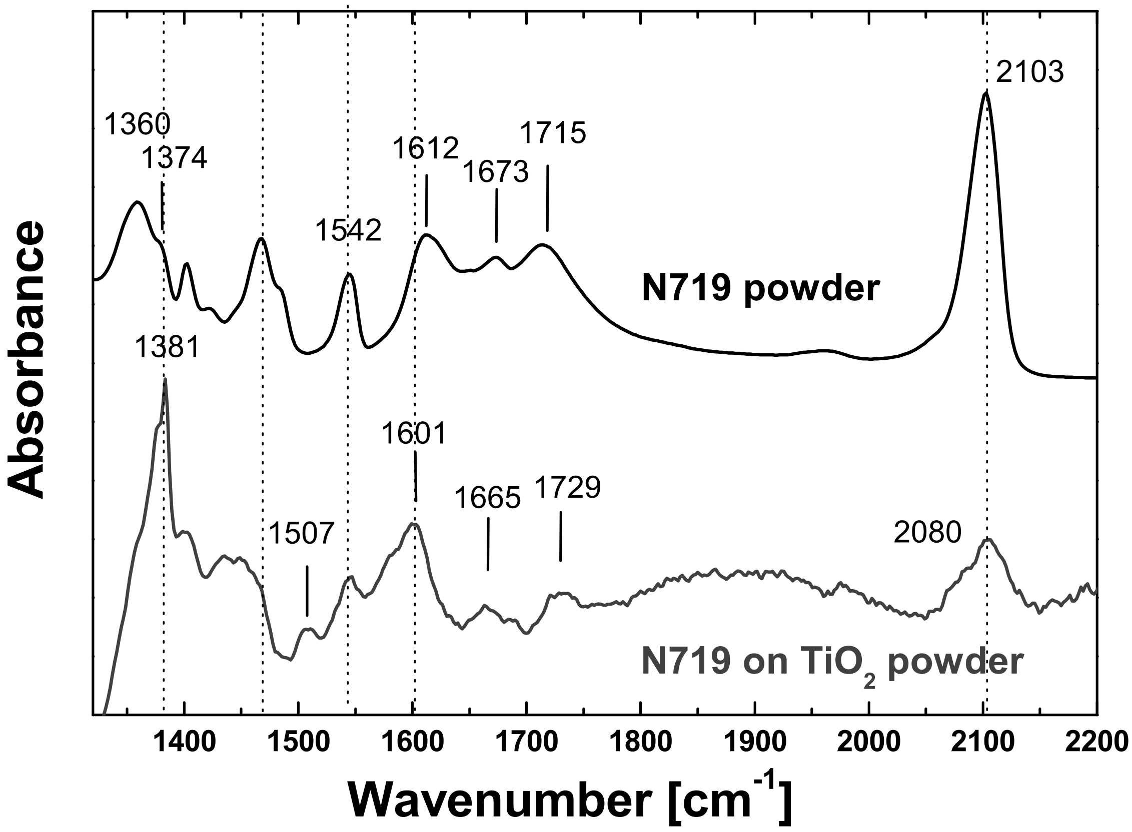

FIG. 5.15. FTIR spectrum of N719 adsorbed on TiO_2 powder compared with the signal of the dye powder.

process of the titania was performed according to the description of Falaras [92].

Before the adsorption, the TiO_2 particles were dried in vacuum overnight. Approximately 52 mg of titania were added to 10 mL of 10^{-4} M ethanolic solutions of the dyes. The resulting colloidal solutions were stirred overnight. Figure 5.14 shows the solutions at this stage. Then, the modified semiconductor was filtered through a glass frit with porosity 5 (pore size $\sim 1\mu$m) and thoroughly washed with ethanol, until all non-adsorbed molecules were removed. Finally the material was dried in air. Before pressing it with KBr to pellets, the sensitized anatase particles were further dried in vacuum. The final spectra were obtained after subtracting the signal of a KBr pellet with TiO_2 powder. In some of the measurements, the broad background signals were partly removed by fitting procedures.

5.3.1 FTIR Spectroscopy of N719

The quality of the spectrum recorded on N719 adsorbed on TiO_2 powder is very poor due to the presence of a broad background signal (see Fig. 5.15), but a qualitative comparison between the signal of the N719 adsorbed on TiO_2 powder and the signal of the dye powder can be performed. A weak thiocyanato band appears at the same position as in the powder of the pure complex, accompanied by a shoulder at 2080 cm^{-1}. These changes can be induced by a variation in the structure of the molecule upon adsorption, and by a change in the dipole moment of the molecule owing to differences in the location of the protons [7], as it was already mentioned in previous sections.

The two ν(C=O) bands are shifted and decrease in intensity in the adsorbed state. On the other hand, strong $\nu(COO^-)$ bands dominate the spectrum. Both carboxylate lines shift as compared with their position in the non-adsorbed dye. The asymmetric mode moves from 1612 to 1601 cm^{-1}, and the symmetrical one from 1374 to 1381 cm^{-1}. Other vibrational lines such as the ν(C=C) mode of the bipyridine at 1544 cm^{-1} seem to be unaffected. Taking into account that the ν(C=O) bands are strongly attenuated and that the carboxylate stretching lines appear with high intensity, it can be concluded that the adsorption occurs via the carboxy groups in a bridging or bidentate chelating linkage. If the criterion of the spectral separation of the carboxylate bands is used, which is 252 cm^{-1} in the salt and 220 cm^{-1} in the adsorbed dye, the conclusion is also that the linkage occurs in bridging or bidentate chelating form. These observations are in accordance with the results of the previous section on TiO_2 paste films and with other studies reported in the literature [7,59].

The presence of ν(C=O) lines shows that there are still protonated carboxylic acid groups present. The positions of these lines are slightly shifted with respect to the ionic dye and a broad peak shows up around 3150 cm^{-1}. This indicates that part of the protonated carboxy groups are forming H-bonds with the powder surface [59].

5.3.2 FTIR Spectroscopy of Ru-TPA_2

Few changes occur in the spectrum of the Ru-TPA_2 adsorbed on TiO_2 with respect to that of the unadsorbed dye, see Fig. 5.16. After the sensitization of the powder, the ν(C=O) line appears slightly shifted to lower wavenumbers (1723 cm^{-1}) with noticeably higher intensity. However, no carboxylate bands seem to be present in the spectrum. The band at 1283 cm^{-1} assigned to ν(C-N) and ν(C-H) bending modes also seems to be enhanced in the anchored state, whereas the ν(C=C) of disubstituted benzene at 1508 cm^{-1} decreases in intensity.

Since there are no lines of the $\nu(COO^-)$ modes and the C=O stretching mode increases in intensity, it can be concluded that the binding to the nanoparticles occurs via unidentate or ester-like linkage or hydrogen bonding. From the fact that some bands ascribed to the donor ligand (bpy-TPA_2) appear to be affected by the adsorption, it can be expected that chemical bonds, not only physisorption, are formed between the dye and the TiO_2 powder.

It has been shown that the adsorption on the titania nanoparticles occurs through unidentate or ester-like linkage, while also hydrogen bonding can be present. However,

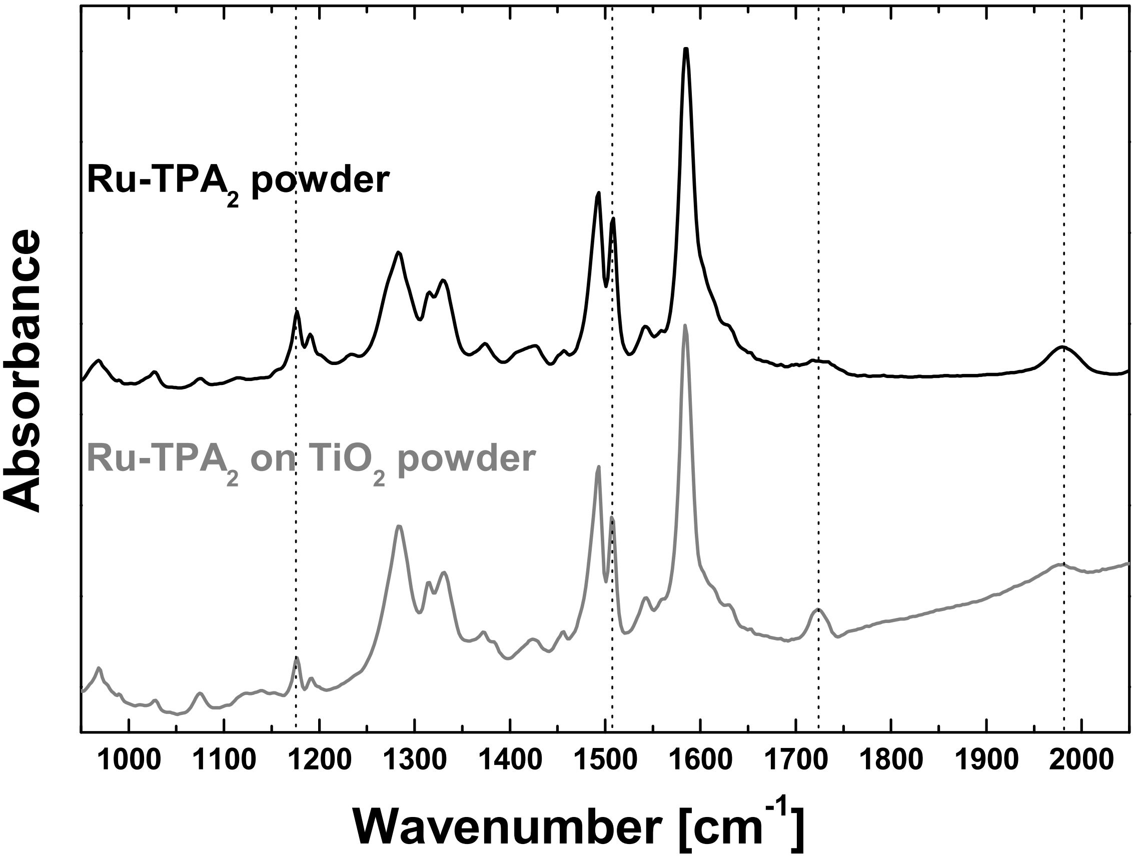

FIG. 5.16. FTIR spectrum of Ru-TPA_2 adsorbed on TiO_2 powder compared with the signal of the dye powder.

in the previous chapter the anchoring type of Ru-TPA_2 on TiO_2 paste films was investigated, showing that the adsorption was formed via bridging or bidentate chelate bonds. Obviously the differences in the systems can lead to completely different adsorption configurations.

5.4 Summary and Conclusions

In this chapter, the characterization of the adsorption of N719 and Ru-TPA_2 on two different nanocrystalline TiO_2 substrates has been performed. The first part is devoted to the investigations of dye-sensitized anatase paste films, whereas in the second part the complexes are anchored to anatase nanopowder. UV-VIS, Raman, and FTIR spectroscopy have been used.

The investigated ruthenium polypyridyl dyes contain carboxy moieties as anchoring groups. These carboxy groups can interact with metal ions in different ways: by physical adsorption via hydrogen bonding, or via chemical bond formation with a unidentate linkage, a bidentate (or chelating) linkage, or a bridging linkage. In the unidentate form, one oxygen atom of the carboxylic-acid group interacts with the metal ion resulting in an ester-like bond. In the bidentate and bringing linkage both oxygen atoms of this group interact equally with one metal ion, or with two metal ions, respectively.

In the first part, the UV-VIS absorption measurements of the titania film substrates show that the electronic transitions are slightly influenced by the adsorption, shifting to lower energies. Raman experiments at different excitation wavelengths demonstrate that photoinduced charge-transfer processes take place efficiently between the adsorbate and the substrate. Moreover, this is the first time that the Raman spectrum of Ru-bpy dyes (in this case, the dye N719) adsorbed on TiO_2 has been obtained without the resonance condition, only by means of SERS enhancement. Preresonant effects in the case of Ru-TPA_2 permit one to measure Raman spectra of high quality. The presence of a fluorescence background has been assigned to residual amounts of non-chemisorbed molecules. From the Raman measurements, the coordination of both complexes on the TiO_2 paste films has been proposed to occur via bidentate or bridging linkage. This result has been confirmed by the ATR-FTIR spectra, which provide a direct fingerprint of the deprotonation state of the carboxy moieties and their interaction with the TiO_2 surface.

It has also been shown that the thiocyanate group of the complex N719 is affected by adsorption, whereas the donor ligand of Ru-TPA_2, the bpy-TPA_2, seems to be only slightly influenced.

Neither Raman nor ATR-FTIR spectroscopies show differences in the binding configuration of the dye N719 on the titania paste when the samples are prepared from different solvents. Only minor differences in the SERRS spectra have been observed.

In the second part, FTIR measurements in KBr pellets of the dyes adsorbed on anatase nanopowder reveal that the dye N719 binds via bridging or bidentate chelate linkage to the TiO_2, similar as in the case of the anatase paste, whereas the Ru-TPA_2 complex appears to bind via unidentate or ester-like linkage or by direct physisorption via H-bonding. The latter results are contrary to those obtained on the anatase paste, indicating a strong dependence of the anchoring configuration on the morphology of the semiconductor.

The experiments have shown that Raman and FTIR spectroscopies are complementary techniques which can provide structural information of the dye/semiconductor system, as well as of the relevant changes caused by the adsorption process.

Chapter 6

Conclusions and Outlook

6.1 Summary and Conclusions

Ruthenium(II) complexes containing polypyridyl ligands are intensely investigated as potential photosensitizers in organic solar cells [1–4]. Of particular interest is their use in dye-sensitized solar cells based on nanocrystalline films of TiO_2. Functional groups of the dye allow for efficient anchoring on the semiconductor surface and promote the electronic communication between the donor orbital of the dye and the conduction band of the semiconductor.

In this thesis, ruthenium bipyridiyl complexes with ligands of different nature have been investigated in order to obtain a better understanding of the influence of the interactions between solvent, complex, and substrate. The dyes were the well-known $(Bu_4N)_2[Ru(dcbpyH)_2(NCS)_2]$ or N719 photosensitizer with cyano ligands and a new dye, $[Ru(dcbpyH_2)_2(bpy\text{-}TPA_2)](PF_6)_2$ or Ru-TPA_2, with triphenylamine (TPA) moieties.

UV-VIS, normal Raman, preresonance and resonance Raman, SERS, absorption-FTIR and ATR-FTIR spectrocopies have been used. The Raman spectra were recorded with a HeNe (λ = 632.8 nm) and a frequency-doubled Nd:YAG laser (λ = 532 nm) as excitation sources. The results can be summarized as follows:

In chapter 3, the pure dyes have been spectroscopically characterized. UV-VIS absorption experiments show solvatochromic shifts of the electronic transitions of the two dyes due to H-bonding and donor-acceptor interactions between the ligands and the solvent molecules. The N719 transitions exhibit a blue shift with increasing Gutmann acceptor number, as was already observed for other cyano and thiocyano complexes. In contrast, the Ru-TPA_2 transitions show a red shift with increasing Gutmann donor number of the solvent, except for water, which causes a larger shift than ethanol. An extra contribution of the different deprotonated states of the dyes has also to be taken into account.

The resonance Raman spectrum of N719 suggests that the lowest MLCT transition corresponds to the injection of an electron into the bipyridine ligands. The lines of the TPA ligand dominate the recorded Raman spectra of Ru-TPA$_2$ both with the red and with the green laser. With the green excitation, the bipyridine lines seem to be stronger indicating the influence of preresonance effects. A detailed vibrational line assignment has been performed for both Raman and FTIR spectra.

Different types of TiO$_2$ substrates and powders were used. The Raman and FTIR spectra have been shown and the lines have been assigned to vibrations. The crystallinity of the different samples has also been briefly discussed.

In chapter 4, the influence of the solvent on the adsorption of the two dyes on colloidal particles has been studied with surface-enhanced Raman spectroscopy (SERS). Water, ethanol, and acetonitrile were used as solvents, and the SERS substrates were colloidal silver and gold solutions.

The analysis of the recorded spectra reveals that the dyes are adsorbed on the colloidal systems in different ways depending on the solvent. At acidic pH values, when dissolved in acetonitrile (hydrogen bond acceptor solvent), the dyes do not deprotonate completely and bind via their electron-donor ligands, whereas in water (both hydrogen bond donor and hydrogen bond acceptor) they also bind via their electron-acceptor ligands. In ethanol (hydrogen bond donor), N719 has the same behavior as in water, whereas Ru-TPA$_2$ only binds through its electron-acceptor ligands.

At basic pH, there is still an influence of the nature of the solvent on the way how the molecules attach to the metallic particles. In acetonitrile, acceptor for hydrogen bonds, the binding via their electron-donor ligands is favored, whereas in water and ethanol, hydrogen bond donors, they also bind through their acceptor ligands, the dicarboxybipyridines.

The SERRS signals of the N719 dye are very close to the SERS spectra recorded with the red laser, but with the characteristics of the resonance effect. The comparison with the RRS of N719 powder indicates that only the vibrations related with the anchoring to the colloidal system are likely to be affected by the adsorption. For Ru-TPA$_2$, the spectra are also very similar for both excitation wavelengths with a slight enhancement of the lines corresponding to the bipyridines due to preresonance effects.

Furthermore, it turned out that in aqueous gold solutions of the dyes no SERS signal is produced and in ethanolic gold solutions the SERS effect is very weak. This can be ascribed to the smaller affinity of the complexes to gold as compared to silver, which apparently has the consequence that the interaction between dye and gold nanoparticle is not strong enough to break the hydrogen bonds between the dye and the solvent molecules.

Strong SERS signals were recorded for both complexes in the gold solution when dissolved in acetonitrile, and, moreover resonance effects are present, mainly for the Ru-TPA$_2$ dye. The UV-VIS absorption maximum shifts because of a charge transfer effect between the complex and the metallic nanoparticle. The similarities of the SERS and the SERRS signals of Ru-TPA$_2$ indicate the important role of the chemical enhancement mechanism. Charge transfer, H-bonding, and donor-acceptor interactions are crucial for the interpretation of the observed spectra. The variation of the pH to basic values has the same influence as for the silver solution: N719 shows small variations in its adsorption configuration, whereas the spectra of Ru-TPA$_2$ do not change at all, confirming the strong affinity of the TPA ligands to the gold.

Moreover, it was found that the presence of the electrolyte NaCl seems to favor the binding via the donor ligands.

In chapter 5, the adsorption of the N719 and Ru-TPA$_2$ on two different nanocrystalline TiO$_2$ substrates has been characterized. The first part is devoted to the investigations of dye-sensitized anatase paste films, whereas in the second part the complexes are anchored to anatase nanopowder. UV-VIS, Raman, and FTIR spectroscopy have been used.

The investigated ruthenium polypyridyl dyes contain carboxy moieties as anchoring groups. These carboxy groups can interact with metal ions in different ways: by physical adsorption via hydrogen bonding, or via chemical bond formation with a unidentate linkage, a bidentate (or chelating) linkage, or a bridging linkage. In the unidentate form, one oxygen atom of the carboxylic-acid group interacts with the metal ion resulting in an ester-like bond. In the bidentate and bridging linkage both oxygen atoms of this group interact equally with one metal ion, or with two metal ions, respectively.

In the first part, the UV-VIS absorption measurements of the titania film substrates show that the electronic transitions are slightly influenced by the adsorption, shifting to lower energies. Raman experiments at the two excitation wavelengths demonstrate that photoinduced charge-transfer processes take place efficiently between the adsorbate and the substrate. Moreover, this is the first time that the Raman spectrum of Ru-bpy dyes (in this case, the dye N719) adsorbed on TiO$_2$ has been obtained without the resonance condition, only by means of SERS enhancement. Preresonant effects in the case of Ru-TPA$_2$ permit one to measure Raman spectra of high quality. The presence of a fluorescence background has been assigned to residual amounts of non-chemisorbed molecules. From the Raman measurements, the coordination of both complexes on the TiO$_2$ paste films has been proposed to occur via bidentate or bridging linkage. This result has been confirmed by the ATR-FTIR spectra, which provide a direct fingerprint of the deprotonation state of the carboxy moieties and their interaction with the TiO$_2$ surface.

It has also been shown that the thiocyanate group of the complex N719 is affected by adsorption, whereas the donor ligand of the Ru-TPA$_2$, the bpy-TPA$_2$, seems to be only slightly influenced.

Neither Raman nor ATR-FTIR spectroscopy show differences in the binding configuration of the dye N719 on the titania paste when the samples are prepared from different solvents. Only minor differences in the SERRS spectra have been observed.

In the second part of chapter 5, FTIR measurements in KBr pellets of the dyes adsorbed on anatase nanopowder reveal that the dye N719 binds to the TiO_2 via bridging or bidentate chelate linkage, similar as in the case of the anatase paste, whereas the Ru-TPA_2 complex appears to bind via unidentate or ester-like linkage or by direct physisorption via H-bonding. The latter results are contrary to those obtained on the anatase paste, indicating a strong dependence of the anchoring configuration on the morphology of the semiconductor.

6.2 Further Work

From the conclusions of this work it is clear that a big step towards the understanding of photosensitizers dyes has been done, but still open questions remain. On the other hand, only part of a solar cell has been the subject under study. Investigations of a complete solar cells can provide further information about the interaction of all the components, and hence, the performance of such photovoltaic cells can be optimized. A sketch of the composition of such a photovoltaic system is shown in Fig. 6.1, together with the image of a section of a real solid-state dye-sensitized solar cell.

Lowest MLCT transition of Ru-TPA_2

In chapter 3, the MLCT and ILCT of the dyes N719 and Ru-TPA_2 have been investigated. In particular, the lowest MLCT band of the N719 complex has been studied with

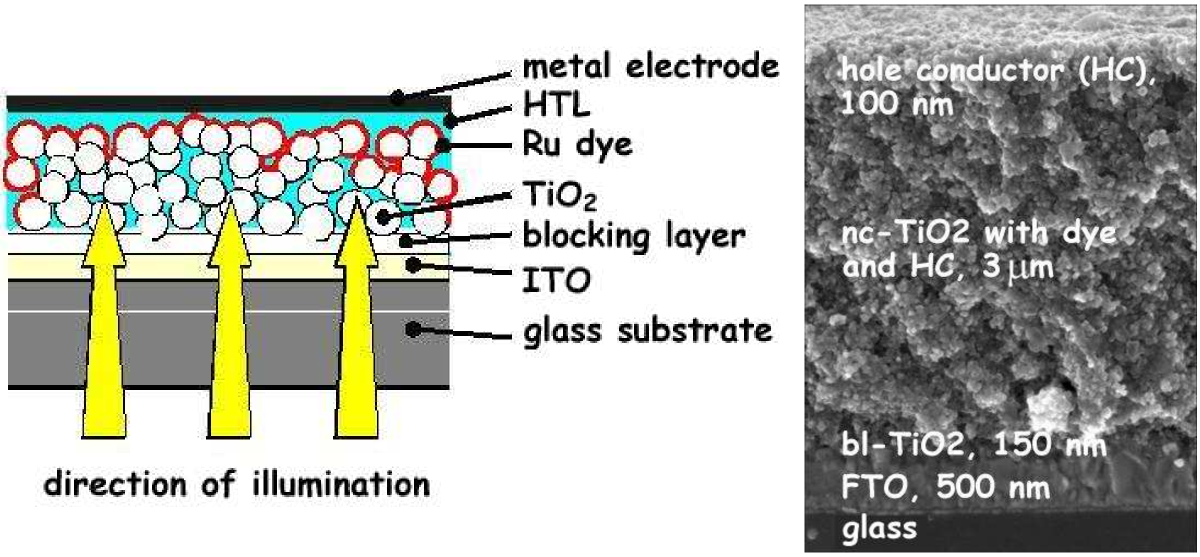

FIG. 6.1. Solar cell working principle. Electron microscope image of a section of a real solid-state dye-sensitized solar cell.

resonance Raman spectroscopy, whose results show that this transition corresponds to a charge transfer from the ruthenium atom to the bipyridine ligands (acceptor ligands). The preresonance results of the Ru-TPA_2 suggest that the lowest MLCT transition of this complex also corresponds to the injection of an electron to a bipyridine moiety, but in this case both, the donor and acceptor ligands, contain bipyridine groups, so no conclusion can be drawn in this respect. An excitation wavelength close to the lowest MLCT absorption band (see Table. 3.1), will permit one to identify the nature of the lowest charge-transfer transition. In addition, measurements on Ru-TPA_2 adsorbed on TiO_2 with RRS will provide further information about the influence of the adsorption and of the nature of anchoring to the titania nanostructure.

Hole transport layer

In this work the interaction of two Ru-dyes with silver, gold, and titanium dioxide nanoparticles and substrates has been analyzed. In complete solar cells, the charge-transfer cycle which takes place in the system semiconductor/dye is closed with a redox mediator, usually iodine-based electrolytes. However, in a step towards real solid-state devices, an amorphous solid layer is used instead of the electrolyte [97]. This layer is called *hole transport layer*; it is usually based on a low-molecular-weight compound. One possible material of this type is the spiro-OMeTAD (abbreviated name for the molecule plotted in Fig. 6.2) [43, 45].

A good understanding of the processes which occur at the interface of the hole transport layer with the dye/TiO_2 (see Fig. 6.1) is crucial for the improvement of this type of cell. This can be done using surface Raman spectroscopy and ATR-FTIR, as was demonstrated in the present work. The Raman lines of the spiro-OMeTad are very strong, so it will be convenient to perform the Raman measurements are performed with resonant laser sources.

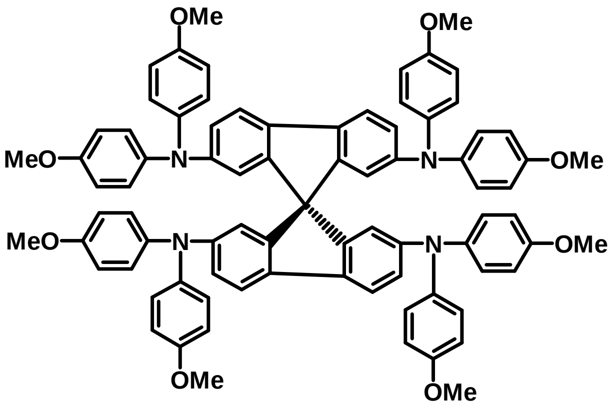

FIG. 6.2. Chemical structure of spiro-OMeTAD.

Potential-dependent experiments

Resonance micro-Raman spectrophotoelectrochemistry combines spatial resolution, offering the ability to detect the vibrational properties of separate components in the nanocrystalline cell, with a dynamic control of the electrochemical interface via the applied potential [98]. This technique has been successfully applied in electrolyte solar cells [98, 99] for investigating the photoelectrode/electrolyte interface, and it can probably also be extended to solid-state photovoltaic devices. Within this thesis, only few potential dependent experiments were performed and these measurements did not exploit resonance effects. The lines of the hole transport layer appeared very strong and no lines of the dye were visible. Therefore no variation with the applied potential was found. Perhaps, better results may be obtained using resonance Raman spectroscopy.

Appendix A

Laser and Light-Induced Effects on the Dyes

During the recording of the Raman spectra of several samples, spectral modifications of the signals due to laser and light-induced effects seem to take place. These changes can be ascribed to changes of the morphology of the complex under irradiation, as well as to degradation processes occurring in the system after UV-VIS illumination under certain conditions. The most important effects are briefly described in this appendix. All Raman measurements described in the following sections were performed with the excitation line of the HeNe laser at 632.8 nm.

A.1 Laser-Induced Modification of Ru-TPA_2

When the Raman spectrum of the dye Ru-TPA_2 dissolved in water was recorded, some spectral changes were induced during the irradiation. The temporal evolution of the Raman signal has been investigated. These changes are not occurring when the sample is measured in powder state (see Fig. 3.6). In the latter case, under very high laser powers the dye is degradated and the signal slowly disappears, but no noticeable modification of the lines is observed. Hence, this laser-induced effect must be related with the nature of the interaction of the complex with the solvent.

Also, when the SERS spectrum of this complex dissolved in water was recorded under high-intensity irradiation, spectral modifications of the Raman lines occurred. The spectrum undergoes an even stronger modification than in normal Raman measurements due to the influence of the surface-enhancement effects. A temporal sequence of the SERS spectra of the Ru-TPA_2 complex in aqueous silver solution is shown in Fig. A.1. In the literature, structural changes of the Ag-bpy system upon illumination with the 514.5 nm Ar^+ laser line have already been reported [100].

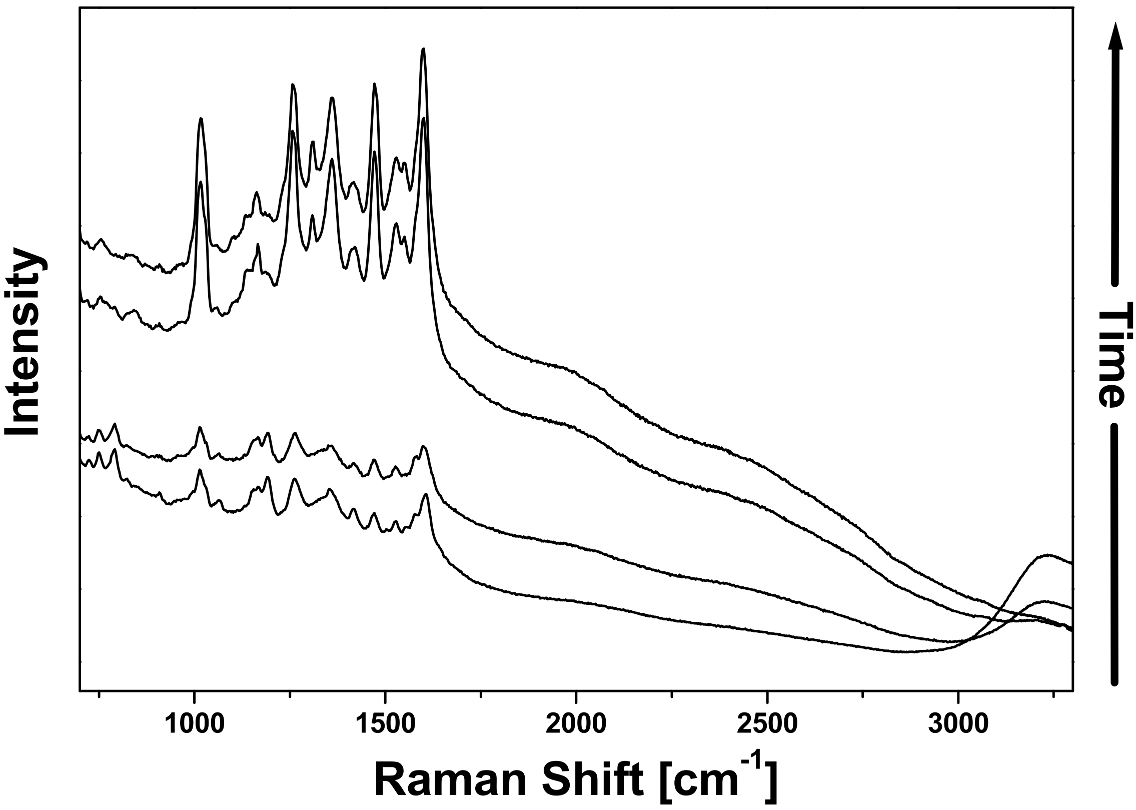

FIG. A.1. Temporal sequence of SERS spectra of Ru-TPA$_2$ in aqueous silver solution under high-power laser irradiation. Between the first and the last spectrum, 23 hours passed.

The modifications observed in both cases can be ascribed to a deprotonation process of the complex in the presence of water caused by the irradiation. In the Ru-TPA$_2$ aqueous solution, the carboxylic-acid groups seem to lose their protons with the absorption of light, and a strong band of the symmetric stretching vibration of the carboxylate unit appears at 1370 cm $^{-1}$. Other changes take place in the spectrum, and the bands of the bipyridine ligands appear to increase slightly. In the case of the SERS solution with silver nanoparticles, larger variations of the spectrum occur (see Fig. A.1).

The results of chapter 4 show that the SERS spectrum of the Ru-TPA$_2$ dye in acidic aqueous silver solution is composed of a mixture of the signals of the donor and acceptor ligands (see Fig. 4.3), since the dye binds to the nanoparticles via both moieties. Under high-power irradiation, the dye seems to deprotonate, and the resulting carboxylate groups bind to the metallic nanoparticles. Since in SERS, the part of the molecule which is in contact with the metallic nanostructure appears to be subject to stronger enhancement, the lines corresponding to the bipyridine ligands increase in intensity. After long irradiation, the bpy lines dominate the spectrum and are overlapping with the signals of the rest of the dye. In Fig. A.1, the spectral range is plotted up to 3300 cm^{-1}, so that the O-H stretching domain is also included. It was mentioned in chapter 4 that neither the ν(OH) lines of the carboxylic-acids groups, nor the ν(OH) bands of the water were usually observed in the recorded spectra. But in this temporal sequence, some broad bands seem to be present in the beginning at $\sim 3250^{-1}$ which can be assigned to the OH groups of the dicarboxybipyridine moieties or to the water. It is well resolved that these lines disappear from the spectrum, and simultaneously the bands of the bipyridine moieties dramatically increase in intensity. If the band is due to the OH groups of the dye, then this finding may confirm the hypothesis of the deprotonation of the dye under strong irradiation. However, if the bands stems from the water, its origin remains an open question.

Another factor which can contribute to the increase of the SERS signals is that the laser can reduce silver ions which are still present in the solution in addition to the nanoparticles. The ability of intense laser-light to reduce silver ions has also been observed by other groups [101].

Also other types of laser-induced reactions have been reported in the literature, e.g. nitro-to-amine conversion [102] or the formation of hematite from iron ions (Fe^{3+}) (α-Fe_2O_3) [41]. Hence, high light intensities in the laser focus can have various effects.

A.2 Thiocyanato Loss

The degradation mechanisms in dye-sensitized solar cells have been studied by Greijer Agrell et al. with UV-VIS and IR spectroscopy [103]. This group used the N719 complex in the cells. They found that the thiocyanato ligand was the most sensitive part of the dye, it is degradated in air at high temperatures, and in water it seems to be exchanged with H_2O/OH^-. Both processes, in air and in water, are accelerated under visual illumination.

The samples investigated in this thesis were usually kept in the dark, but during the different measurements, the dye solutions or substrates are exposed to UV-VIS light. As a consequence, the intensity of the vibrational line corresponding to the thiocyanato group at ~ 2100 cm^{-1} as measured in Raman and IR experiments decreased in the course of a few weeks. The loss of the thiocyanato groups, or its exchange with water in solution, is the most noticeable degradation effect. This prevents a quantitative discussion of the intensity of the band in the spectra of different samples, when the solutions are not freshly prepared.

A.3 Aggregation

This last section corresponds to a laser effect which does not modify the characteristics of the Raman spectrum of the measured sample, but increases only its intensity. Under continuous irradiation in Ru-TPA_2 acetonitrile and aqueous solution, the dissolved

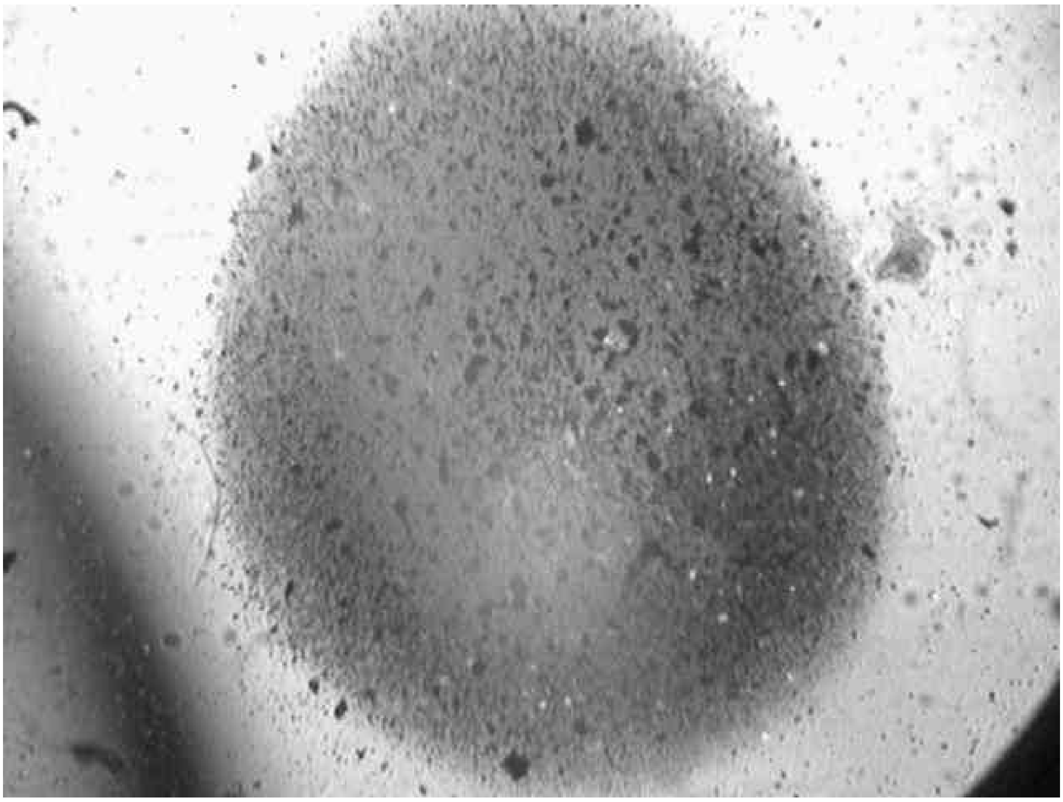

FIG. A.2. Accumulation of Ru-TPA$_2$ particles in acetonitrile gold solution on the bottom of the cuvette after long illumination with the red laser. The darker spot indicates the laser path. The photograph was taken after 4 hours.

dye molecules aggregate to particles and accumulate around the laser beam. The solutions are measured in cuvettes in the inverted microscope, and after some minutes of illumination, dye crystallites start to diffuse from all regions of the solution to the position of the laser beam. They accumulate at the glass surface of the cuvette.

When the particles accumulate, an increase of the Raman signal is observed until the saturation occurs. This effect is found with the red and the green laser. Similar results were also obtained in gold solutions of this dye, and in silver solutions of the complex N719. A photograph of the resulting accumulation in gold solution is shown in Fig. A.2. The photograph was taken with an objective of magnification 4× and NA = 0.18.

Bibliography

[1] B. O'Regan and M. Grätzel, "A low-cost, high-efficiency solar-cell based on dye-sensitized colloidal TiO_2 films," *Nature*, vol. 353, p. 737, 1991.

[2] A. Hugot-Le Goff, S. Joiret, and P. Falaras, "Raman resonance effect in a monolayer of polypyridyl ruthenium(II) complex adsorbed on nanocrystalline TiO_2 via phosphonated terpyridyl ligands," *J. Phys. Chem. B*, vol. 103, p. 9569, 1999.

[3] H. Greijer, J. Lindgren, and A. Hagfeldt, "Resonance Raman scattering of a dye-sensitized solar cell: mechanism of thiocyanato ligand exchange," *J. Phys. Chem. B*, vol. 105, p. 6314, 2001.

[4] M. K. Nazeeruddin, S. M. Zakeeruddin, R. Humphry-Baker, M. Jirousek, P. Liska, N. Vlachopoulos, V. Shklover, C.-H. Fischer, and M. Grätzel, "Acid-base equilibria of (2,2'-bipyridyl-4,4'-dicarboxy acid)ruthenium(II) complexes and the effect of protonation on charge-transfer sensitization of nanocrystalline titania," *Inorg. Chem.*, vol. 38, p. 6298, 1999.

[5] World Nuclear Association, "Energy for the World - Why Uranium?," *www.world-nuclear.org.*

[6] A. Hagfeldt and M. Grätzel, "Molecular photovoltaics," *Acc. Chem. Res.*, vol. 33, p. 269, 2000.

[7] M. K. Nazeeruddin, R. Humphry-Baker, P. Liska, and M. Grätzel, "Investigation of sensitizer adsorption and the influence of protons on current and voltage of a dye-sensitized nanocrystalline TiO_2 solar cell," *J. Phys. Chem. B*, vol. 107, p. 8981, 2003.

[8] G. M. Barrow, *Molecular Spectroscopy.* New York: McGraw-Hill International Book Company, 1962.

[9] D. A. Long, *Raman Spectrometry.* London: McGraw-Hill International Book Company, 1977.

[10] H. W. Siesler and K. Holland-Moritz, *Infrared and Raman spectroscopy of polymers.* New York: Marcel Dekker, 1980.

[11] H. Barańska, A. Łabudzińska, and J. Terpiński, *Laser Raman spectrometry: Analytical applications.* Chichester: Wiley, 1987.

[12] C. N. Banwell and E. M. McCash, *Fundaments of Molecular Spectroscopy.* London: McGraw-Hill International Book Company, 1994.

[13] G. Turrel and J. Corset, *Raman microscopy: developments and applications.* London: Academic Press Limited, 1996.

[14] M. K. Nazeeruddin, M. Grätzel, K. Kalyanasundaram, R. B. Girling, and R. E. Hester, "Raman characterization of charge-transfer transitions in ligand-bridged binuclear polypyridyl complexes of ruthenium(II)," *J. Chem. Soc., Dalton Trans.*, p. 323, 1993.

[15] M. K. Nazeeruddin, E. Muller, R. Humphry-Baker, N. Vlachopoulos, and M. Grätzel, "Redox regulation in ruthenium(II) polypyridyl complexes and their application in solar energy conversion," *J. Chem. Soc., Dalton Trans.*, vol. 23, p. 4571, 1997.

[16] C. V. Raman and K. S. Krishnan, "A new type of secondary radiation," *Nature*, vol. 121, p. 501, 1929.

[17] Z.-Q. Tian, B. Ren, and D.-Y. Wu, "Surface-enhanced Raman scattering: from noble to transition metals and from rough surfaces to ordered nanostructured," *J. Phys. Chem. B*, vol. 106, p. 9463, 2002.

[18] H. Yamada, N. Tani, and Y. Yamamoto, "Infrared specular reflection and SERS spectra of molecules adsorbed on smooth surfaces," *J. Electron Spectrosc.*, vol. 30, p. 13, 1983.

[19] L. G. Quagliano, B. Jusserend, and D. Orani, "SERS spectroscopy to study adsorbates on semiconductor surfaces," *J. Raman Spectrosc.*, vol. 29, p. 721, 1998.

[20] W. B. Caldwell, D. Campbell, K. M. Chen, B. R. Herr, C. A. Mirkin, A. Malik, M. K. Durbin, P. Dutta, and K. G. Huang, "A highly ordered self-assembled monolayer film of an azobenzenealkanethiol on Au(111) - Electrochemical properties and structural characterization by synchrotron in-plane X-ray-diffraction, atomic-force microscopy, and surface-enhanced Raman-spectroscopy," *J. Am. Chem. Soc.*, vol. 117, p. 6071, 1995.

[21] R. G. Freeman, K. G. Grabar, K. J. Allison, R. M. Bright, J. A. Davis, A. P. Guthrie, M. B. Hommer, M. A. Jackson, P. C. Smith, D. G. Walter, and M. J. Natan, "Self-assembled metal colloid monolayers - An approach to SERS substrates," *Science*, vol. 267, p. 1629, 1995.

[22] K. G. Grabar, R. G. Freeman, M. B. Hommer, and M. J. Natan, “Preparation and characterization of Au colloid monolayers,” *Anal. Chem.*, vol. 67, p. 735, 1995.

[23] M. Fleischmann, P. J. Hendra, and A. J. McQuillan, “Raman spectra of pyridine adsorbed at a silver electrode,” *Chem. Phys. Lett.*, vol. 26, p. 163, 1974.

[24] D. L. Jeanmaire and R. P. V. Duyne, “Surface Raman spectroelectrochemistry part I. Heterocyclic, aromatic, and aliphatic amines adsorbed on the anodized silver electrode,” *J. Electroanal. Chem.*, vol. 84, p. 1, 1977.

[25] M. G. Albrecht and J. A. Creighton, “Anomalously intense raman spectra of pyridine at a silver electrode,” *J. Am. Chem. Soc.*, vol. 99, p. 5215, 1977.

[26] S. Nie and R. Emory, “Probing single molecules and single nanoparticles by surface-enhanced Raman scattering,” *Science*, vol. 275, p. 1102, 1997.

[27] K. Kneipp, Y. Kneipp, H. Kneipp, L. T. Perelman, I. Itzkan, R. D. Dasari, and M. Feld, “Single molecule detection using surface-enhanced Raman scattering (SERS),” *Phys. Rev. Lett.*, vol. 78, p. 1667, 1997.

[28] A. Ilie, C. Durkan, W. I. Milne, and M. E. Welland, “Surface-enhanced Raman spectroscopy as a probe for local modification of carbon films,” *Phys. Rev. B*, vol. 66, p. 045412, 2002.

[29] M. Moskovits, “Surface-enhanced spectroscopy,” *Rev. Mod. Phys.*, vol. 57, p. 783, 1985.

[30] R. K. Chang and T. E. Furtak, *Surface enhanced Raman scattering.* New York: Plenum, 1982.

[31] A. Otto, I. Mrozek, H. Grabhorn, and W. Akemann, “Surface-enhanced Raman-scattering,” *J. Phys.- Condens. Mat.*, vol. 4, p. 1143, 1992.

[32] H. Ueba, S. Ichimura, and H. Yamada, “Where are we in the study of SERS - Role of chemisorption and charge-transfer,” *Surf. Sci.*, vol. 119, p. 443, 1982.

[33] J. R. Lombardi, R. L. Birke, T. Lu, and J. Xu, “Charge-transfer theory of surface enhanced Raman spectroscopy: Herzberg-Teller contributions,” *J. Chem. Phys.*, vol. 84, p. 4174, 1986.

[34] A. Campion and P. Kambhampati, “Surface-enhanced Raman scattering,” *Chem. Soc. Rev.*, vol. 27, p. 241, 1998.

[35] J. R. Ferraro and K. Nakamoto, *Introductory Raman spectroscopy.* San Diego: Academic Press Limited, 1994.

[36] E. Hecht and A. Zajac, *Optics.* Reading, Massachusetts: Addison-Wesley Publishing Company, 1979.

[37] M. Diem, *Introduction to modern vibrational spectroscopy.* New York: John Wiley & sons, 1993.

[38] T. Schittkowski, *Aufbau und Test eines konfokalen Raman-Mikroskops.* Diploma Thesis: Universität Bayreuth, 1999.

[39] M. Bauer, *Aufbau und Test eines konfokalen Mikroskopes und Fluoreszenzmikroskopes.* Diploma Thesis: Universität Bayreuth, 1999.

[40] L. Kador, T. Schittkowski, M. Bauer, and Y. Fan, "Three-dimensional materials analysis by confocal Raman microspectroscopy," *Appl. Optics*, vol. 40, p. 4965, 2001.

[41] C. Pérez León, L. Kador, M. Zhang, and A. H. E. Müller, "*In situ* laser-induced formation of α-Fe_2O_3 from Fe^{3+} ions in a cylindrical core-shell polymer brush," *J. Raman Spectrosc.*, vol. 35, p. 165, 2004.

[42] C. Pérez León, L. Kador, B. Peng, and M. Thelakkat, "Influence of the solvent on the surface-enhanced spectra of ruthenium(II) bipyridyl complexes," *J. Phys. Chem. B*, vol. 109, p. 5783, 2005.

[43] U. Bach, D. Lupo, P. Comte, J. Moser, F. Weissörtel, J. Salbeck, H. Spreitzer, and M. Grätzel, "Solid-state dye-sensitized mesoporous TiO_2 solar cells with high photon-to-electron conversion efficiencies," *Nature*, vol. 395, p. 583, 1998.

[44] M. Thelakkat, J. Hagen, D. Haarer, and H.-W. Schmidt, "Poly(triarylamine)s-synthesis and application in electroluminiscent devices and photovoltaics," *Synth. Met.*, vol. 102, p. 1125, 1999.

[45] U. Bach, K. De Cloedt, H. Spreitzer, and M. Grätzel, "Characterization of hole transport in a new class of spiro-linked oligotriphenylamine," *Adv. Mater.*, vol. 12, p. 1060, 200.

[46] C. Jäger, R. Bilke, M. Heim, D. Haarer, H. Karickal, and M. Thelakkat, "Hybrid solar cells with novel hole transporting poly(triarylamine)s," *Synth. Met.*, vol. 1543, 2001.

[47] K. Peter, H. Wietasch, B. Peng, and M. Thelakkat, "Dual-functional materials for interface modifications in solid-state dye-sensitised TiO_2 solar cells," *Appl. Phys. A*, vol. 79, p. 65, 2004.

[48] K. Peter and M. Thelakkat, “Synthesis and characterization of bifunctional polymers carrying tris(bipyridyl)ruthenium(II) and triphenylamine units,” *Macromolecules*, vol. 36, p. 1779, 2003.

[49] J. C. Curtis, B. P. Sullivan, and T. J. Meyer, “Hydrogen-bonding-induced solvatochromism in the charge-transfer transitions of ruthenium(II) and ruthenium(III) ammine complexes,” *Inorg. Chem.*, vol. 22, p. 224, 1983.

[50] E. Y. Fung, A. C. M. Chua, and J. C. Curtis, “Evidence for a specific solvent solute interaction as a major contributor to the excited-state distorsion of the emitting charge-transfer state in the complex $(bpy)_2Ru(II)(CN)_2$,” *Inorg. Chem.*, vol. 27, p. 1294, 1988.

[51] E. M. Kober, B. P. Sullivan, and T. J. Meyer, “Solvent dependence of metal-to-ligand charge-transfer transitions - Evidence for initial electron localization in MLCT excited-states of 2,2’-bipyridine complexes of ruthenium(II) and osmium(II),” *Inorg. Chem.*, vol. 23, p. 2098, 1984.

[52] C. J. Timpson, C. A. Bignozzi, B. P. Sullivan, E. M. Kober, and T. J. Meyer, “Influence of solvent on the spectroscopic properties of cyano complexes of ruthenium(II),” *J. Phys. Chem.*, vol. 100, p. 2915, 1996.

[53] P. Chen and T. J. Meyer, “Medium effects on charge transfer in metal complexes,” *Chem. Rev.*, vol. 98, p. 1439, 1998.

[54] J. Streiff and J. L. McHale, “Resonance Raman study of the solvatochromic electronic transitions of $[Ru(NH_3)_4bipyridine]^{2+}$ in methanol and dimethylsulfoxide,” *J. Chem. Phys.*, vol. 112, p. 841, 2000.

[55] V. Gutmann, *The Donor-Acceptor Approach to Molecular Interactions.* New York: Plenum, 1988.

[56] P. Corio, M. L. A. Temperini, J. C. Rubim, and P. S. Santos, “The effects of the solvent and electrolyte in the surface enhanced Raman spectrum of iron(II)bis(1,10-phentanthroline)dicyano: evidence for the formation of strong ion-pairs,” *Spectrochim. Acta A*, vol. 55, p. 2411, 1999.

[57] G. Wolfbauer, A. M. Bond, G. B. Deacon, D. R. MacFarlane, and L. Spiccia, “Experimental and theoretical investigations of the effect of deprotonation on electronic spectra and reversible potentials of photovoltaic sensitizers: Deprotonation of cis-L_2RuX_2 (L = 2,2’-bipyridine-4,4’-dicarboxylic acid; X = CN^-, CNS^-) by electrochemical reduction at platinum electrodes,” *J. Am. Chem. Soc.*, vol. 122, p. 130, 2000.

[58] L. C. T. Shoute and G. R. Loppnow, “Excited-state metal-to-ligand charge transfers dynamics of a ruthenium(II) dye in solution and adsorbed on TiO_2 nanoparticles from resonance Raman spectroscopy,” *J. Am. Chem. Soc.*, vol. 125, p. 15636, 2003.

[59] K. S. Finnie, J. R. Bartlett, and J. L. Woolfrey, “Vibrational spectroscopic study of the coordination of (2,2’-bipyridyl-4,4’-dicarboxy acid)ruthenium(II) complexes to the surface of nanocrystalline titania,” *Langmuir*, vol. 14, p. 2744, 1998.

[60] S. M. Zakeeruddin, M. K. Nazeeruddin, F. P. Rotzinger, R. Humphry-Baker, K. Kalyanasundaram, M. Grätzel, V. Shklover, and T. Haibach, “Molecular engineering of photosensitizers for nanocrystalline solar cells: Synthesis and characterization of Ru dyes based on phosphonated terpyridines,” *Inorg. Chem.*, vol. 36, p. 5937, 1997.

[61] S. M. Zakeeruddin, M. K. Nazeeruddin, R. Humphry-Baker, M. Grätzel, and V. Shklover, “Stepwise assembly of tris-heteroleptic polypyridyl complexes of ruthenium(II),” *Inorg. Chem.*, vol. 37, p. 5251, 1998.

[62] S. Quillard, G. Louarn, and S. Lefrant, “Vibrational analysis of polyaniline: A comparative study of leucoemeraldine, emeraldine, and pernigraniline bases,” *Phys. Rev. B*, vol. 50, p. 12496, 1994.

[63] C. Kvarnström, A. Petr, P. Damlin, T. L. ans A. Ivaska, and L. Dunsch, “Raman and FTIR spectroscopic characterization of electrochemically synthesized poly(triphenylamine), PTPA,” *J. Solid State Electr.*, vol. 6, p. 505, 2002.

[64] A. M. F. Benial, V. Ramakrishnan, and R. Murugesan, “Infrared and laser Raman studies of $[Ni(II)(dppe)Cl_2]$ and $[Co(III)(dppe)_2Cl_2]PF_6$ (dppe = 1,2-bis(diphenylphosphino)ethane),” *Spectrochim. Acta A*, vol. 58, p. 1703, 2002.

[65] B. Peng, G. Jungmann, C. Jäger, D. Haarer, H.-W. Schmidt, and M. Thelakkat, “Systematic investigation of the role of compact TiO_2 layer in solid state dye-sensitized TiO_2 solar cells,” *Coord. Chem. Rev.*, vol. 248, p. 1479, 2004.

[66] W. Ma, Z. Lu, and M. Zhang, “Investigation of structural transformations in nanophase titanium dioxide by Raman spectroscopy,” *Appl. Phys. A*, vol. 66, p. 621, 1998.

[67] X. Zhu, R. Birringer, U. Herr, and H. Gleiter, “X-ray diffraction studies of the structure of nanometer-sized crystalline materials,” *Phys. Rev. B*, vol. 35, p. 9085, 1987.

[68] M. Gotić, M. Ivanda, A. Sekulić, A. T. S. Musić, S. Popović, and K. Furić, "Microstructure of nanosized TiO_2 obtained by sol-gel synthesis," *Matt. Lett.*, vol. 28, p. 225, 1996.

[69] P. Falaras, A. Hugot-Le Goff, M. Bernard, and A. Xagas, "Characterization by resonance Raman spectroscopy of sol-gel TiO_2 films sensitized by the $Ru(PPh_3)_2(dcbipy)Cl_2$ complex for solar cells application," *Sol. Energ. Mat. Sol. C.*, vol. 64, p. 167, 2000.

[70] Y. Iida, M. Furukawa, T. Aoki, and T. Sakai, "Raman spectrum of ultrafine anatase powders derived from hydrolysis of alkoxide," *Appl. Spectrosc.*, vol. 52, p. 673, 1998.

[71] M. R. Waterland and D. F. Kelley, "Photophysics and relaxation dynamics of Ru(4,4'-dicarboxy-2,2'-bipyridine)$_2$cis(NCS)$_2$ in solution," *J. Phys. Chem. A*, vol. 105, p. 4019, 2001.

[72] M. A. Webb, F. J. Knorr, and J. L. McHale, "Resonance Raman spectrum of [Ru(bipyridine)$_3$]$^{2+}$ in water, acetonitrile and their deuterated derivatives: the possible role of solvent in excited-state charge localization," *J. Raman Spectrosc.*, vol. 32, p. 481, 2001.

[73] P. Corio, G. F. S. Andrade, I. C. N. Diógenes, I. S. Moreira, F. C. Nart, and M. L. A. Temperini, "Characterization of the $[Ru(CN)_5(pyS)]^{4-}$ ion complexes adsorbed on gold, silver and copper substrates by surface-enhanced Raman spectroscopy," *J. Electroanal. Chem.*, vol. 520, p. 40, 2002.

[74] N. Leopold and B. Lendl, "A new method for fast preparation of highly surface-enhanced Raman scattering (SERS) active silver colloids at room temperature by reduction of silver nitrate with hydroxylamine hydrochloride," *J. Phys. Chem. B*, vol. 107, p. 5723, 2003.

[75] K. Faulds, R. E. Littleford, D. Graham, G. Dent, and W. E. Smith, "Comparison of surface-enhanced resonance Raman scattering from unaggregated and aggregated nanoparticles," *Anal. Chem.*, vol. 76, p. 592, 2004.

[76] P. K. Mallick, G. D. Danzer, D. P. Strommen, and J. R. Kincaid, "Vibrational spectra and normal-coordinate analysis of tris(bipyridine)ruthenium(II)," *J. Phys. Chem.*, vol. 92, p. 5628, 1988.

[77] H. R. Virdee and R. E. Hester, "Surface-enhanced Raman spectra of [Ru(II)(bpy)$_3$]$^{2+}$ and electrochemically generated [Ru(II)(bpy)$_3$]$^{+}$ on silver electrode," *J. Phys. Chem.*, vol. 88, p. 451, 1984.

[78] Z.-Y. Zhu, C. Mao, R.-Y. Yang, L.-X. Dai, and C.-S. Nie, "Surface-enhanced Raman spectra of Ru(II) homo- and heterolytic complexes with 2,2'-bipyridine and 1,1'-biisoquinoline in aqueous silver sol," *J. Raman Spectrosc.*, vol. 24, p. 221, 1993.

[79] S. Schneider, G. Brehm, W. Jäger, M. I. Silva, H. D. Durrows, and S. T. Formosinho, "Vibrational spectra, normal coordinate analysis and excited-state lifetimes for a series of polypyridylruthenium(II) complexes," *J. Raman Spectrosc.*, vol. 27, p. 163, 1996.

[80] I. Srnová-Šloufová, B. Vlčková, T. L. Snoeck, D. J. Stufkens, and P. Matějka, "Surface-enhanced Raman scattering and surface-enhanced resonance Raman scattering excitation profiles of Ag-2,2'-bipyridine surface complexes and of $[\mathrm{Ru(bpy)_3}]^{2+}$ on Ag colloidal surfaces: Manifestations of the charge-transfer resonance contributions to the overall surface enhancement of Raman scattering," *Inorg. Chem.*, vol. 39, p. 3551, 2000.

[81] H. A. Azab, I. T. Ahmed, and M. R. Mahmoud, "Potentiometric determination of the apparent dissociation constants of some dicarboxylic acids in various hydroorganic media," *J. Chem. Eng. Data*, vol. 42, p. 593, 1997.

[82] U. K. Sarkar, "A pH-dependent SERS study of thiophene-2-carboxylic acid adsorbed on Ag-sols," *Chem. Phys. Lett.*, vol. 374, p. 341, 2003.

[83] M. Kim and K. Itoh, "pH dependence of surface-enhanced Raman scattering spectra from 2,2'-bipyridine adsorbed on Ag colloids," *J. Phys. Chem.*, vol. 91, p. 126, 1987.

[84] S. Sánchez-Cortés and J. García-Ramos, "Anomalous Raman bands appearing in surfaced-enhanced Raman spectra," *J. Raman Spectrosc.*, vol. 29, p. 365, 1998.

[85] P. Wang and G. Wu, "Ultraviolet laser excited surface enhanced Raman scattering of thiocyanate ion on the Au electrode," *Chem. Phys. Lett.*, vol. 385, p. 96, 2004.

[86] S. Umapathy, A. M. Cartner, A. W. Parker, and R. E. Hester, "Time-resolved resonance Raman spectroscopic studies of the photosensitization of colloidal titanium dioxide," *J. Phys. Chem.*, vol. 94, p. 8880, 1990.

[87] P. Falaras, M. Grätzel, A. Hugot-Le Goff, M. Nazeeruddin, and E. Vrachnou, "Dye sensitization of TiO_2 surfaces studied by Raman spectroscopy," *J. Electrochem. Soc.*, vol. 140, p. L92, 1993.

[88] T. J. Meyer, G. J. Meyer, B. W. Pfennig, J. R. Schoonover, C. J. Timpson, J. F. Wall, C. Kobusch, X. Chen, B. M. Peek, C. G. Wall, W. Ou, B. W. Erickson,

and C. A. Bignozzi, “Molecular-level electron transfer and excited assemblies on surfaces of metal oxides and glass,” *Inorg. Chem.*, vol. 33, p. 3952, 1994.

[89] A. Hugot-Le Goff and P. Falaras, “Origin of new bans in the Raman spectra of dye monolayers adsorbed on nanocrystalline TiO_2,” *J. Electrochem. Soc.*, vol. 142, p. L38, 1995.

[90] K. Murakoshi, G. Kano, Y. Wada, S. Yanagida, H. Miyazaki, M. Matsumoto, and S. Murasawa, “Importance of binding states between photosensitizing molecules and the TiO_2 surface for efficiency in a dye-sensitized solar cell,” *J. Electroanal. Chem.*, vol. 396, p. 27, 1995.

[91] M. Nara, H. Torii, and M. Tasumi, “Correlation between the vibrational frequencies of the carboxylate group and the types of its coordination to a metal ion: An ab initio molecular orbital study,” *J. Phys. Chem.*, vol. 100, p. 19812, 1996.

[92] P. Falaras, “Synergetic effect of carboxylic acid functional groups and fractal surface characteristics for efficient dye sensitization of titanium oxide,” *Sol. Energ. Mat. Sol. C.*, vol. 53, p. 163, 1998.

[93] N. W. Duffy, K. D. Dobson, K. C. Gordon, B. H. Robinson, and A. J. NcQuillan, “In situ infrared spectroscopic analysis of the adsorption of ruthenium(II) bipyridyl dicarboxylic acid photosensitisers to TiO_2 in aqueous solutions,” *Chem. Phys. Lett.*, vol. 266, p. 451, 1997.

[94] L. C. T. Shoute and G. R. Loppnow, “Excited-state dynamics of alizarin-sensitized TiO_2 nanoparticles from resonance Raman spectroscopy,” *J. Chem. Phys.*, vol. 117, p. 842, 2002.

[95] Y.-X. Weng, L. Li, Y. Liu, L. Wang, and G.-Z. Yang, “Surface-binding forms of carboxylic groups on nanoparticulate TiO_2 surface studied by the interface-sensitive transient triplet-state molecular probe,” *J. Phys. Chem. B*, vol. 107, p. 4356, 2003.

[96] G. B. Deacon and R. J. Phillips, “Relationships between the carbon-oxygen stretching frequencies of carboxylato complexes and the type of carboxylate coordination,” *Coord. Chem. Rev.*, vol. 33, p. 227, 1980.

[97] J. Hagen, W. Schaffrath, P. Otschik, R. Fink, A. Bacher, H.-W. Schmidt, and D. Haarer, “Novel hybrid solar cells consisting of inorgnic nanoparticles and an organic hole transport material,” *Synth. Met.*, vol. 89, p. 215, 1997.

[98] T. Stergiopoulos, M. Bernard, A. Hugot-Le Goff, and P. Falaras, “Resonance micro-Raman spectrophotoelectrochemistry on nanocrystalline TiO_2 thin film electrodes sensitized by Ru(II complexes.,” *Coord. Chem. Rev.*, vol. 248, p. 1407, 2004.

[99] M. Bernard, H. Cachet, P. Falaras, A. Hugot-Le Goff, M. Kalbac, I. Lukes, N. T. Oanh, T. Stergiopoulos, and I. Arabatzis, “Sensitization of TiO_2 by polypyridine dyes,” *J. Electrochem. Soc.*, vol. 150, p. E155, 2003.

[100] I. Srnová, B. Vlčková, I. Němec, M. Šlouf, and J. Štěpánek, “Infrared microscopy and surface-enhanced Raman scattering of Ag colloid-2,2’-bipyridine film,” *J. Mol. Struct.*, vol. 483, p. 213, 1999.

[101] Y. Xiao, Y.-S. Li, and G. H. Swihart, “A close look at silver oxide colloid for surface-enhanced Raman scattering,” *Talanta*, vol. 58, p. 755, 2002.

[102] K. Kim, S. J. Lee, and K. L. Kim, “Surface-enhanced Raman scattering of 4-nitrothioanisole in Ag sol,” *J. Phys. Chem. B*, vol. 108, p. 16208, 2004.

[103] H. Greijer Agrell, J. Lindgren, and A. Hagfeldt, “Degradation mechanisms in a dye-sensitized solar cell studied by UV-VIS and IR spectroscopy,” *Solar Energy*, vol. 75, p. 169, 2003.

Acknowledgments

> *– Adieu, dit le renard. Voici mon secret. Il est très simple: on ne voit bien qu'avec le coeur. L'essentiel est invisible pour les yeux.*
> *– L'essentiel est invisible pour les yeux, répéta le petit prince, afin de se souvenir.*
> *– C'est le temps que tu as perdu pour ta rose qui fait ta rose si importante.*
> *– C'est le temps que j'ai perdu pour ma rose..., fit le petit prince, afin de se souvenir.*
> *– Les hommes ont oublié cette vérité, dit le renard. Mais tu ne dois pas l'oublier. Tu deviens responsable pour toujours de ce que tu as apprivoisé. Tu es responsable de ta rose...*
> *– Je suis responsable de ma rose..., répéta le petit prince, afin de se souvenir.*
>
> Antoine de Saint-Exupéry

It has taken me a lot of time to start to write the last words of this book. Finally I have decided to help myself by stealing some ideas that other friends and colleagues used in their manuscripts.

As André Leopold mentioned in his "Danksagung", some months has passed since this thesis was handed in, even the "Kolloquium" is far in the past. When I am writing these lines, I find myself in the next step of my career, which is not but another intermediate phase of my life. The time gives me an interesting perspective of my time in Bayreuth, of all what I learned there, of all people I met there. And I wonder how one can summarize in few lines all these feelings and all gratitude to so much help and support... Well, I guess I have no other option, I have to do it anyway, so I will start.

First of all, I would like to thank my "Doktorvater" Lothar Kador. First, because he offered me the possibility to work in his group. Second, because with his large patience, his huge knowledge and his not less modesty, he made possible this work and showed me how a scientist should be. Nor should I forget his constant help and support in my scientific and also personal life, and his lectures on "Deutsche-Oberfränkische" language and culture.

I am very thankful to Mukundan Thelakkat and Bin Peng for providing me the dyes and substrates investigated along this thesis. I also want to thank other members of the MCI who helped me!! In special, I would like to express my gratitude and friendship to Laura Torre Lorente, who discovered to me, amongst other things, the wonderful world of the chemistry: thanks for always being there! It was nice to have accessories in the chemistry department.

Even if the results of my collaboration with Mingfu Zhang and Axel H. E. Müller are not explicitely included in this thesis, I would like to mention that it was nice to work with them. I have also to mention another collaborator, Kerim R. Allakhverdiev with whom I really enjoy the Raman measurements and the coffee breaks!!

The EPVI chaired by Dietrich Haarer, Werner Köhler and Jürgen Köhler, together with the BIMF and their members provided me a nice working atmosphere and a motivating ambience. The technical staff: Michael Heimler, Waltraud Joy (thanks for preparing my samples!), Evelyn Hülsmann, Karin Baier, Clarissa Abetz, Monika Birkelbach, Werner Reichstein and Wolfgang Richter, did a helpful work and offered a friendly company. My colleagues Ralf Bausinger, Gerhard Wittko, Ulrich Theissen, Erwin Lang and Klaus Jäger were the first who took care of me when I arrived to the department. Slowly, also other people were involved like Marianne Hartung, Martin Richter, André Leopold, Renate Müller, Richard Hildner, Markus Bauer and Manuela Dezi who finally became my friends. Not to forget Tobias Schittkowski, Michael Häckel, Silke Oellerich, Jürgen Baier, Hanna Engelke, Christiane Scharf, Tobias Pflock, Florian Spreitler, Bettina Theissen, Clemens Hofmann, Dagmar Klostermeier, Wolfgang Enge, Albert Voit, Stefan Jungblut, Jürgen Müller, Dominik Stadelmaier, Robert Kellner, and Philipp Schleiffer. Thank you all for your assistance and for creating this nice environment!

There are also other people in the Faculty of Physics of Bayreuth I would like to thank like Christine Linser who solved many of my bureaucratic problems and the workers of the mechanic workshop and of the “Rechenzentrum”.

And what to say about Alberto de Lózar and Alejandro Luque... I am really happy that Alberto convinced us to come with him to Bayreuth. I would never forget the time we were together, the team we formed, the family we created, the friendship we developed and the selfless support that I have always found from their side.

Our Bayreuther family and group of friends were formed by a variable number of people of different nationalities, with whom, as well as with some of the already mentioned people, I shared dinners, cinemas, parties, travels, endless debates, visits to the hospital, laughs and tears, “WGs”, dreams and many other things. Amongst others, their members were Mar García Mira, Susanne Jensen, Hania Wypukol, Martin Riedel, Nicola Daro, Luis Miguel Fernández, Òscar Gratacós Torrà, Alberto Rivera, Lucía Veruca, Patricia Chimeno Marcos, Juan Gala Serra, Ana Escartín, Eva Estrada, Almudena García, Matthias Meinel, Paola Uribe, Óscar Lafuente, Nicole Teichmann, Jérémy

Chabé, Marilyn, Jordi Soriano Fradera, Wolfgang Michel, Pramod & wife Pullarkat, Pablo Fernández, Adela Subjakova, David Mercader, Damián Morán Dauchez, Sobiroh Kariyo, Esther Jodar, Rafa Gargallo, Reinhard Richter, Silke Struck, Saskia Knispel, Blanca Serrano and Ayaka Shimizu. My time in Bayreuth was much nicer because of you.

Pavel Akimov has been a very important person for me during my PhD years, I cannot imagine my life in Bayreuth without his company, his advice and his help and support. Thank you for all Pavel!

I do not want to forget my friends of Seville: Víctor Morales Flórez, Daniel Martín Reina, Cristina Llanos Rodríguez, Cisela de Nova Pozuelo, Jaime Hernando Sánchez, Fco. Javier González González, Joanne Parker, Mario Herrero Romero, Yumi Yakuwa, Saulo Morales, Esther Mesas García, Rafael Linares Doblado, Vicente Maestro, Juan Manuel Becerril, Diana Morales Flórez, Marta Soler Montiel, María Yusti, Carmen Millán Chacartegui, Fernando Paredes, Carlos Ojeda, Rocío Marín Cantero, and the European fraction: Gonzalo Angulo, Lola Rodríguez, Alejandro Cuetos Menéndez and Francisco Gallego Gómez. I am grateful for their standing encouragement. I was very happy to see that they were constantly waiting for me and that they always received me with open arms!!

And to finish I would like to thank my hole family, especially my mother, my father, my brothers Rafael, Fernando, Alberto and Nacho, my sister Soledad, my great-aunt “la Tita” and my cousin Virginia for their continuous support, for believing in me and for being always there for anything I needed!! Gracias familia Pérez León por estar siempre ahí.

Thank you all for making me feel everywhere at home.